Use of geophysical techniques for the detection and monitoring of water flow and internal erosion in porous media : Application to earth dams

Yara Maalouf

Université Grenoble Alpes

THÈSE

Pour obtenir le grade de

DOCTEUR DE L'UNIVERSITÉ GRENOBLE ALPES

Spécialité : **Sciences de la Terre, de l'Univers et de l'Environnement**

Arrêté ministériel : 25 mai 2016

Présentée par

Yara MAALOUF

Thèse dirigée par **Christophe Voisin** et
codirigée par **Grégory Bièvre et Naji Khoury**

préparée au sein de **l'Institut des Sciences de la Terre** et
de **l'École Doctorale Sciences de la Terre, de l'Environnement et des Planètes**

Méthodes géophysiques pour la détection et le suivi temporel d'écoulements et d'érosion interne dans les milieux poreux: application aux digues en terre

Geophysical techniques for the detection and monitoring of water seepage and internal erosion in porous media : Application to earth dams

Thèse soutenue publiquement le **3 Décembre 2021**,
devant le jury composé de :

Philippe GUEGUEN
Directeur de recherche, ISTerre, Grenoble, Président
Frédéric NGUYEN
Professeur, Université de Liège, Belgique, Rapporteur
Jonathan CHAMBERS
Senior Researcher, BGS, Royaume-Uni, Rapporteur
Yannick FARGIER
Chargé de Recherche, Université Gustave Eiffel, France, Invité
Christophe VOISIN
Chargé de Recherche, ISTerre, Grenoble, Directeur de Thèse
Grégory BIÈVRE
Maître de Conférence, ISTerre, Grenoble, Invité
Naji KHOURY
Maître de Conférence, NDU-Louaizé, Liban, Invité

ABSTRACT

Water storage structures have always been built to provide water for agricultural and household needs. But before these structures become a threat to human lives, monitoring techniques have to be implemented to prevent any malfunctioning during their operation lives. Earthen dams, one of the oldest reservoir types undergo different types of failures throughout their aging. One of the major causes of breach is internal erosion. This type of failure happens when soil particles of the structure itself or its foundation migrate downstream by seepage flow.

Being the primary cause of failure, internal erosion also known as piping, is a complex phenomenon. It requires extensive monitoring to be detected at early stages. Otherwise, by the time visual signs appear it would be too late to prevent any human or agricultural losses.

Conventional geotechnical methods usually used require a lot of instrumentation and sometimes fail to detect the first stages of internal erosion. Recent researches have focused on the use of geophysical techniques (non-destructive) to detect anomalies within the body of the dam and monitor its evolution. In this study, we will focus on the use of electrical resistivity and seismic techniques in the detection and monitoring of water seepage and internal erosion in earthen dams. For this purpose, experiments were conducted under controlled environment in the laboratory and in the field to better assess what happens during seepage and followed by the 4 stages of internal erosion: i/ initiation, ii/ continuation, iii/ progression and iv/ breach.

We have identified seismic signals occurring in swarms and bursts. They respond to the changes in the water head applied thus the change in the flow rate. Therefore, they are the signature of the coupling between the water seepage and the rearrangement of soil particles. Furthermore, the frequency is found to be the same regardless of the dimensions of the earth dams. However, we hypothesize that it is directly related to the diameter (dimensions) of the pipe.

The electrical resistivity technique failed to detect and monitor the water seepage and, more importantly, the evolution towards failure. The passive seismic monitoring revealed a complex, highly non-linear evolution process with several episodes. The detection of the internal erosion process is a key parameter – we show here a rate of 2 cm/min for soil parameters that are similar to field conditions.

RÉSUMÉ

Les structures de stockage d'eau ont toujours été construites pour fournir de l'eau pour les besoins agricoles et domestiques. Mais avant que ces structures ne deviennent une menace pour les vies humaines, des techniques de surveillance doivent être mises en œuvre pour prévenir tout dysfonctionnement pendant leur durée d'exploitation. Les barrages en terre, l'un des plus anciens types de réservoirs, subissent différents types de défaillances au cours de leur vieillissement. L'une des principales causes de rupture est l'érosion interne. Ce type de défaillance se produit lorsque des particules de sol de la structure elle-même ou de sa fondation migrent vers l'aval par le biais d'un flux d'infiltration.

Étant la principale cause de défaillance, l'érosion interne, également appelée renard hydraulique, est un phénomène complexe. Il nécessite une surveillance approfondie pour être détecté à un stade précoce. Sinon, lorsque des signes visuels apparaissent, il est trop tard pour prévenir toute perte humaine.

Les méthodes géotechniques conventionnelles habituellement utilisées nécessitent beaucoup d'instrumentation et échouent parfois à détecter les premiers stades de l'érosion interne. Les recherches récentes se sont concentrées sur l'utilisation de techniques géophysiques (non destructives) pour détecter les anomalies dans le corps du barrage et suivre son évolution. Dans cette étude, nous allons nous concentrer sur l'utilisation de la résistivité électrique et des techniques sismiques dans la détection et le suivi des infiltrations d'eau et de l'érosion interne dans les barrages en terre. A cette fin, des expériences ont été menées dans un environnement contrôlé en laboratoire et sur le terrain pour mieux évaluer ce qui se passe pendant l'infiltration et suivi par les 4 étapes de l'érosion interne : i/ initiation, ii/ continuation, iii/ progression et iv/ brèche.

Nous avons identifié des signaux sismiques se produisant en essaims et en salves. Ils répondent aux changements de la hauteur d'eau appliquée donc au changement du débit. Par conséquent, ils sont la signature du couplage entre l'infiltration d'eau et le réarrangement des particules du sol. De plus, on constate que la fréquence est la même quelles que soient les dimensions des barrages en terre. Cependant, nous faisons l'hypothèse qu'elle est directement liée au diamètre (dimensions) du tuyau.

La technique de résistivité électrique n'a pas permis de détecter et de surveiller les infiltrations d'eau et, surtout, l'évolution vers la rupture. La surveillance sismique passive a révélé un processus d'évolution complexe, hautement non linéaire, avec plusieurs épisodes. La détection du processus d'érosion interne est un paramètre clé - nous montrons ici un taux de 2 cm/min pour des paramètres de sol qui sont similaires aux conditions de terrain.

ACKNOWLEDGEMENTS

Oprah Winfrey once said: "Surround yourself only with people who are going to take you higher".

I express sincere gratitude to my advisors Christophe Voisin, Grégory Bievre and Naji Khoury. This bumpy road would not have been possible without their guidance, mentoring and full support to accomplish what one day seemed impossible. Naji Khoury, a colleague, a mentor and a friend; you pushed me forward when I laid back and almost gave up. You have secured whatever is needed to get me where I am today. I will always be grateful to you.

I thank the entire team at ISTerre for welcoming me in the laboratory and making sure that my stays in France are productive and comfortable. A lot of appreciation to all the staff members, researchers and colleagues. Moreover, I would like to thank the staff and faculty members at Notre Dame University – Louaize for supporting my Ph.D. work in the laboratory.

I am grateful for USAID, EDF, IRD, Campus France and last but not least Talaya (Société des Eaux de Tarshishe) for the continuous funding of my stays in France and the experimental work that was conducted in Lebanon.

I thank my family – husband and kids – for enduring the hard times when I was away and supported me in every step of the journey. You have always shown me love and compassion. Alain, I would have never reached this far without you. You took the role of a mum and a dad when I was not around. Karl and Léa, I may not have been around you when you needed me but you never showed me that and you always succeeded to draw a smile on my face when my heart was breaking for not being able to hold you and kiss you every night. I love you!

Mum and Dad, you are my pillars since I was born, you are my role models. You have supported every choice I have made and guaranteed that I worry about nothing when you are around. Thank you for surrounding my kids with love and tenderness.

Nancy and Elie – we are not related by blood but it surely feels like it. You were always by my side when I needed you. You have always motivated me and helped me in everything I wanted. Our coffee breaks were enough to boost my morale. Thank you for being there when I needed someone to listen. Elie – I cannot thank you enough for the hard work you have put to make sure that every experiment is successful.

CONTENTS

ABSTRACT ..... **iii**

RÉSUMÉ ..... **v**

ACKNOWLEDGEMENTS ..... **vii**

CONTENTS ..... **ix**

LIST OF FIGURES ..... **xii**

LIST OF TABLES ..... **xix**

INTRODUCTION **1**

CHAPTER 1 STATE OF THE ART **7**

1.1 Earth dams 8
1.2 Internal Erosion Mechanisms 9
1.2.1 Concentrated Leak Erosion 12
1.2.2 Backward Erosion 12
1.2.3 Suffusion 13
1.2.4 Contact Erosion 13
1.3 Monitoring and Detection of Internal Erosion 14
1.3.1 Visual Inspection of Internal Erosion 14
1.3.2 Geotechnical and Hydraulic Monitoring 16
1.3.2.1 Seepage Monitoring *16*
1.3.2.2 Water Pressure Monitoring *16*
1.3.2.3 Deformation Monitoring *16*
1.3.2.4 Temperature Monitoring *16*
1.3.3 Geophysical Monitoring Techniques 17
1.3.3.1 Electro-Magnetic Induction Profiling Technique *17*
1.3.3.2 Ground Penetrating Radar *20*
1.3.3.3 Self-Potential Technique *21*
1.3.3.4 Induced Polarization Technique *23*

1.3.3.5 Electrical Resistivity Technique *25*
1.3.3.6 Seismic Monitoring of Earth dams *34*
1.4 Summary 45

CHAPTER 2 WATER SEEPAGE IN POROUS MEDIA: EXPERIMENTAL FIELD TESTING 47
Experimental setup 48
Electrical Resistivity Tomography 50
Seismic Measurements 50
Results 51
Electrical Resistivity Monitoring 52
Geometric factor analysis *52*
Timelapse ER analysis *53*
Timelapse ER ratios *55*
Active Seismic 57
Seismic Monitoring 57
Vertical geophone: Broadband Analysis *57*
Vertical geophone: 160 – 190 Hz frequency band analysis *59*
Horizontal geophone – Broadband Analysis *60*
Horizontal geophone: 160 – 190 Hz frequency band analysis *61*
Horizontal geophone (Geophone 19): 180 – 220 Hz frequency band analysis *62*
Interpretation and Discussion 63
Limitations 64
Conclusions and Perspectives 64

CHAPTER 3 WATER SEEPAGE IN POROUS MEDIA: LABORATORY EXPERIMENT 67
3.1 Experimental Setup 68
3.1.1 Geotechnical Characteristics of the Seepage Zone 68
3.1.2 Electrical Resistivity Tomography 69
3.1.3 Seismic Monitoring 70
3.2 Results 70
3.2.1 Experimental Protocol and Visual Interpretation 70
3.2.2 Electrical Resistivity Monitoring Results 72
3.2.2.1 Synthetic model of the complete and optimized sequence *72*
3.2.2.2 ER monitoring of the seepage zone *73*

3.2.2.3 ER monitoring of the upper and lower part of the seepage zone 75
3.2.3 Seismic Monitoring 77
3.2.3.4 Broadband analysis 77
3.2.3.5 160 – 190 Hz frequency band analysis 78
3.2.3.6 Events analysis in the 160 – 190 Hz frequency band 80
3.2.3.7 Reference geophone analysis at 160 – 190 Hz frequency band 82
3.3 Interpretation and Discussion 83
3.4 Limitations 84
3.5 Conclusions and Perspectives 85

CHAPTER 4 INTERNAL EROSION IN POROUS MEDIA: GEOPHYSICAL MONITORING OF A LABORATORY SCALE EXPERIMENT 87
4.1 Introduction 89
4.2 Materials and methods 92
4.2.1 Experimental setup 92
4.2.2 Geotechnical characteristics of the seepage zone 93
4.2.3 Electrical resistivity tomography 95
4.2.4 Seismic monitoring 96
4.3 Results 98
4.3.1 Video monitoring 98
4.3.2 Electrical resistivity imaging and monitoring 100
4.3.3 Seismic monitoring 105
4.4 Interpretation and discussion 112
4.5 Conclusions 116

CHAPTER 5 CONCLUSIONS AND PERSPECTIVES 117

REFERENCES 121

APPENDIX 133
Appendix A 134
Appendix B 137
Appendix C 138
Appendix D 139
Appendix E 140
Appendix F 141

List of Figures

Figure 1: Photographs of Dam failure – a. represents the failure of the Hell Hole Dam in California USA in 1964 due to overtopping (Failure of Hell Hole Dam – Geotechnical Photo Album) and b. represents a sinkhole that was developped due to piping failure and internal erosion of the embankment into the foundation (FEMA, 2015). 2

Figure 2: Aqoura reservoir breach in 2015 caused by the collapse of the earth embankment due to internal erosion (*The Daily Star - Lebanon*, 2015). 4

Figure 1-1: Different types of earth dams; (a) Homogeneous dam made out of impermeable material showing the seepage path and its length (L) with the differential head (H), (b) Zoned dam consisting of a core of lower permeability than the body of the dam and (c) Dam structure consisting of pervious materials and an impervious diaphragm at the center. 9

Figure 1-2: The four-stage of internal erosion mechanism depending on their location; a. Internal erosion in the embankment initiated by concentrated leak, b. Internal erosion in the foundation initiated by backward erosion and c. Internal erosion from the embankment to the foundation initiated by backward erosion (Foster and Fell, 1999). 12

Figure 1-3: Internal erosion initiated by concentrated leak. The close-up shows the pipe that has formed and the detachment of soils particles that are migrating towards the downstream (Fell et al., 2015). 13

Figure 1-4: Internal erosion initiated by backward erosion piping formed in the foundation of the earth dam – the line represents the seepage path and the pipe is represented by the rectangle (Sellmeijer et al., 2011) 14

Figure 1-5: Visual observation of the mud water at the downstream of an embankment dam (FEMA, 2015). 16

Figure 1-6: Geophysical profiles conducted on the crest of the Vitineves reservoir (Sentenac et al., 2018). 20

Figure 1-7: EMI results of the survey conducted on the crest of the Vitineves reservoir. The area in the red rectangle shows a low apparent resistivity identifying the seepage zone (Sentenac et al., 2018). 21

Figure 1-8: GPR survey a) results highlighting the presence of an anomaly represented by a white circle indicating the presence of an air-filled cavity, b) representing the size of the cavity, c) the location, d) lateral extension and e) the traces of claws identifying the animal scratches (Chlaib et al., 2014). 22

Figure 1-9: A diagram representing the laboratory setup used for the monitoring of SP of a sand specimen located at the bottom of the column. Three silver electrodes were used in the experiment to monitor SP changes throughout the brine injection (Boleve et al., 2011) .24

Figure 1-10: SP results reflecting the changes with time; (a) changes of SP with water head – cycles 1 to 4 are the changes of heads: 0.5, 1, 1.8 and 1.7 respectively and (b) represents the SP data with respect to changes in head highlighting a linear relationship. Data represented in black and red correspond to the inflow electrode and outflow electrodes respectively (Boleve et al., 2011). 25

Figure 1-11: Schematics of the experimental basin; a) represents the top view and b) a side view with the locations of the profiles P1 to P7 (Abdulsamad et al., 2019). 26

Figure 1-12: 3D inversions of the IP data acquired; a) Tomogram before the leakage started and b) Tomogram during the leakage in the basin. B represents the area with an increase in the chargeability due to the presence of the leakage in the experimental basin (Abdulsamad et al., 2019). 27

Figure 1-13: Different array types with different a-spacing corresponding to the distance between the potential electrodes and the n×a corresponds to the closest distance between the current and potential electrodes. m×a represents the midpoint distance and s determines the maximum number of potential dipoles available within the distance a (Sjödahl, 2006).. 29

Figure 1-14: Pseudo-section of Wenner apparent resistivity data. The x-axis represents the location of the electrodes and the y-axis shows the pseudo-depth of each reading..... 30

Figure 1-15: ERT conducted downstream identifying LRZ1 and LRZ2 and delineating the soil/rock interface by a dashed line (Camarero et al., 2019). 31

Figure 1-16: ER monitoring: A- showing the cross section of the crest with the 3 anomalous zones noted zones A, B and C; B- empty reservoir and the filling (3m depth) and C- empty reservoir at the beginning of the experiment and empty reservoir at the end of the experiment after being filled (Sjödahl et al., 2010). 32

Figure 1-17: Electrical Resistivity results of the Hallby dam monitoring; A: electrical resistivity data at 61.25 m on the crest versus time at different depths and B: electrical resistivity data at 43.75 m on the crest versus time at different depths. Red box indicates the depth of the seepage (Figure 1-17B) (Sjödahl et al., 2008). 34

Figure 1-18: Experimental setup of the laboratory scale earthen dam and the anomalous one introduced to induce internal erosion (Shin et al., 2019). 35

Figure 1-19: Results of the ER data retrieved at different time intervals; Column 1 shows the pseudo sections 1 to 8 from the start of the experiment to the failure respectively; column 2 shows the individual inversions; column 3 is the timelapse analysis using the 1st inversion as starting model and column 4 shows the timelapse analysis with the preceding model as starting model for inversion (Shin et al., 2019). 36

Figure 1-20: Seismic data analysis; (a) Seismograms of the shot at the first geophone of the profile for the analysis of S: S-waves and L: Love waves, (b) Travel-time curves corresponding to 2 shots performed at the end of the profile and one at the center for S-waves analysis, (c) phase velocity versus frequency of the Love waves corresponding to shot at 18 m along the profile and (d) Vs profile following the inversion of the dispersion curve in c) (Bièvre et al., 2017). 38

Figure 1-21: (a) The front view drawing of the laboratory scale earth dam of approximately 600 cm width and roughly 70 cm height. The metal rod is located in the center below geophone 6; (b) cross section view of the earth dam and (c) photograph of the piping following 5 h of water seepage (Planès et al., 2016). 40

Figure 1-22: Velocity changes obtained following the cross correlation conducted on a 1.2 m spaced pairs of sensors (Planès et al., 2016). 41

Figure 1-23: (a) representing the downstream and the leaked water, (b) the different upstream reservoir water head with time and the corresponding stages of the experiment, (c) and (d) the top and cross section view respectively of the dam (Planès et al., 2016). 42

Figure 1-24: (a) Representation of the sensor pairs selected for the analysis of dV/V with the visual leakage locations highlighted by grey rectangles: B and A at the abutment, whereas B-C represents the softening areas; (b) shows the water elevation in the reservoir and the average surface wave velocity, (c) to (f) show dV/V analysis with the sensor pairs selected and shown in part (a) (Planès et al., 2016)..... 43

Figure 1-25: Locating the seismic noise source; a) shows the Probability Density Function (PDF) of the seismic source location before any work has been implemented on the site and c) PDF after finishing the remediation works (Bièvre et al., 2017). 45

Figure 1-26: Results of the passive seismic monitoring: a) shows the early stage of internal erosion when the pipe diameter was still small, b) the spectrogram from the data collected from the geophone located at a distance of 1m from the erosion pipe at the early stage, c) the spectrogram obtained from the analysis of the data collected from the geophone located at a distance of 3.7m from the pipe, d) view of the enlarged pipe leading to further erosion – late stage, e) the spectrogram showing high activity from the data collected from the geophone located at 1m from the erosion pipe at the late stage and e) the spectrogram of the data collected from the geophone located at a distance of 3.7m from the erosion pipe following at the late stage (Hickey et al., 2009). 46

Figure 1-27: IJkdijk dam; a. Upstream view of the embankment dam following construction and b. the dimensions of the embankment dam (Parekh, 2016). 47

Figure 1-28: Acoustic Emission counts of peaks that exceed a threshold set to 10 detected on three channels at the downstream. Red dots represent the measurements during night time (Parekh, 2016). 48

Figure 2-1: Laboratory setup showing the extension of pipes placed downstream for the saturation phase, the geophones and electrodes placed on top of the concrete beam and the tank of water for the control of head. 52

Figure 2-2: Changes in head applied at the upstream as a function of time. The indices represent the stages in the experiment detailed in Table 2-1. 56

Figure 2-3: Synthetic results with the complete (74 measurements) and the optimized (37 measurements) sequences. a) The mesh used for inversion along with the location of the slice c) Coverage slices from the 3D models along with the difference, expressed in percent, between the complete and optimized sequences. All slices pass through the vertical plane defined by the line of electrodes. 58

Figure 2-4: A- Changes in heads of water with time and B-F 2D slices performed on the 3D inversions at different times of the experiment and G- Weighted average of the electrical resistivity data in the soil sample with time; the grey rectangle represents the corrupted data that were not successfully retrieved. The dashed grey lines represent the different stages of water filling detailed in Figure 2-2. 60

Figure 2-5: Average weighted ER monitoring of the upper part and lower part of the seepage zone presented in black and red respectively. The indices represent the stages of the experiment detailed in Table 2-1. 61

Figure 2-6: Seismic monitoring of the experiment: A- Corresponding ΔH with respect to the time of the experiment; B- Broadband time series; C- Corresponding spectrogram of the experiment. The grey dashed lines correspond to the indices defined in Figure 2-2 and Table 2-1 Summary of the experiment stages and the grey rectangles show phases of low activity (night time) next to the experimental setup. 63

Figure 2-7: Seismic monitoring as a function of the head of water; A- Changes of the heads of water applied, B- Seismogam filtered between 160 and 190 Hz and C- the Energy Spectrum Density (PSD) as a function of time centered at a frequency of 170 Hz. 64

Figure 2-8 Identification of the events detected. A- Changes in the water head with time, B- Filtered seismogram in the 160-190 Hz frequency band showing red rectangles of a 6 min duration, C, D, E and F represent the close-up on the 6 min events identified during the water seepage including a 45 s close up window to represent the events observed; they are all represented in the same time and amplitude scales. 66

Figure 2-9 A- Changes in head with time and B- the filtered seismogram in the 160-190 band frequency of the vertical geophone placed as a reference next to the experimental setup 68

Figure 2-10 Schematic representation of the water flow inside the soil sample; A- represents the initial stage of the soil sample at OMC, B- is the saturation phase with the air bubbles moving upwards and the soil particles rearrangement and interparticle interaction and C- shows the entrapped air bubbles at the top of the soil sample. 70

Figure 3-1: Location of the experimental dam in Cerema near Rouen, France. 74

Figure 3-2: Dimensions of the Experimental Dam. A- Front view showing the height of the 3 seepage channels, B- Top view indicating the location of the vertical (pink) and horizontal (green) geophones on the crest and C- Section A-A showing the reservoir and its details. 75

Figure 3-3: Details of F2 seepage channel from A the downstream side showing the geotextile and the geomembrane and B the upstream side showing the PVC pipe, bentonite, filter and the corresponding ΔH. 76

Figure 3-4: Timeline of the geophysical measurements. 78

Figure 3-5: A-Representation of the theoretical geometric factor "K_a" for the Wenner configuration and the corrected geometric factor "K_{corr}" as a function of the electrode spacing "a" and B- represents the ratio between "K_a" and "K_{corr}" as a function of the spacing "a". 79

Figure 3-6: Electrical resistivity monitoring; A- represents the coverage with the overlayed pre-defined 2D mesh and B through I- represent the timelapse analysis for measurements 1 to 8 respectively as highlighted in Figure 3-4. The seepage channels F1, F2 and F3 are also indicated on the figure. 80

Figure 3-7: Timelapse ER ratios with respect to the baseline ERT_0; A-H represent the ratios of the conducted ERTs (from 1 to 8 respectively) to ERT_0. 82

Figure 3-8: Seismic recordings of the vertical geophone located on top of the seepage zone (geophone 6) with varying ΔH; A- Changes in ΔH with time – dashed grey lines delineating the increase in ΔH, B- Time series depicting the seismic activity during the changes in ΔH shown as grey dashed lines and C- Time versus frequency (spectrogram) analysis of the time series shown in B – the dashed grey lines delineate the changes in ΔH. The grey rectangles correspond to the night periods..... 84

Figure 3-9: A- the flow rate recorded during the experiment, B- the Filtered seismogram of the vertical geophone (6) at a frequency band of 160 – 190 Hz and C- the PSD centered at 170 Hz with the grey and the red data showing the unsmoothed and the smoothed data respectively. The dashed lines represent the times and heads as shown in Figure 3-4..... 86

Figure 3-10: Seismic recordings of the horizontal geophone located on top of the seepage zone (geophone 19) with varying ΔH; A- Changes in ΔH with time – dashed black lines delineating the increase in ΔH, B- Time series depicting the seismic activity during the changes in ΔH shown as black dashed lines and C- Time versus frequency (spectrogram) analysis of the time series shown in B – the dashed black lines delineate the changes in ΔH – the magenta rectangle shows the frequency band of 90-120 Hz, the red rectangle shows the frequency band of 160-190 Hz and the cyan rectangle shows the frequency band of 180-220 Hz..... 87

Figure 3-11: Analysis of the horizontal geophone (geophone 19); A- Flowmeter measurements with time of the experiment, B- Filtered seismogram in the 160 - 190 Hz band frequency and C- the PSD of geophone 19 at 170 Hz; the grey data represent the unsmoothed PSD whereas the red data represent the smoothed PSD. 88

Figure 3-12: A- the flow rate recorded during the experiment, B- the Filtered seismogram of the horizontal geophone (19) at a frequency band of 180-220 Hz and C- the PSD centred at 200 Hz with the grey and the red data showing the unsmoothed and the smoothed data respectively. The dashed black lines represent the different increases in heads. 89

Figure 4-1: The different stages of internal erosion in the backward erosion type (modified from Fell et al. (2015). (1) Initiation, when the first soil particle is driven downstream. (2) Continuation, when additional soil particles are washed away. (3) Progression is the formation of the pipe in the embankment and (4) breach represented by the complete failure of the dam. 96

Figure 4-2: Laboratory setup of the seepage experiment. Δh represents the difference in water height between the water level in the tank and the bottom of the soil sample zone. The granulometric distribution of the soil sample is shown. 99

Figure 4-3: Chronological framework of the geophysical measurements along with the observed events. MM: mass movement. 104

Figure 4-4: Captions taken from the video of the camera mounted downstream during the seepage of water in the soil sample. a) The water reaches the downstream. b), c), d) and e) Mass movements MM1 to MM4, respectively. f) Failure of the soil sample allowing water to flow freely. See Figure 3 for the location of the events on the timeframe. 105

Figure 4-5: Synthetic results with the complete (74 measurements) and the optimized (37 measurements) sequences. a) The mesh used for inversion along with the location of the slice shown in Figs. 5b and 5c. b) Resistivity slices from the 3D models. c) Coverage slices from the 3D models along with the difference, expressed in percent, between the complete and optimized sequences. All slices pass through the vertical plane defined by the line of electrodes. 106

Figure 4-6: Experimental electrical resistivity tomography results. a) Tomographic images for measurements ep01 to ep03 from top to bottom, respectively. b) Resistivity difference of tomograms ep02 and ep03 with respect to ep01. c) Evolution of the average resistivity of the upper (in black) and lower (in red) sub-zone. Error bars correspond to the standard deviation. These sub-zones are indicated in Fig. 6a. 108

Figure 4-7: Seismic recordings of geophone 3 located above the soil sample zone. a) Time series showing the main seismic events. Arrows and orange lines delimit the different phases of the experiment (valve opening, full upstream hose, water downstream, mass movements MM1 to MM4 and failure with references to the video snapshots of Figure 4-4. b) Time versus frequency analysis of the seismic recordings presented in Figure 4-7a. The purple rectangles show the three frequency ranges that are further analysed. 110

Figure 4-8: a), c) and e) seismic record of geophone 3 filtered in the 140-160, 80-120 and 5-20 Hz frequency range, respectively. Vertical orange lines indicate the different phases of the experiment (details at the bottom of the figure). The grey stripe corresponds to water movements in the tank following valve opening. b), d) and f) Cumulative number of events per class of amplitude normalized to the strongest event. Grey: normalized amplitudes

between 0.1 and 0.4; blue: normalized amplitudes between 0.4 and 0.6; green: normalized amplitudes between 0.6 and 0.8; red: normalized amplitudes between 0.8 and 1. 111

Figure 4-9: Impulsive, short-duration (around 0.1 s) seismic events generated each ~0.5 s (Δt) by a water leakage at the upstream part of the experiment and which was used as a seismic source to investigate the soil sample. The total duration shown in the figure is around 2.56 s. 114

Figure 4-10: Autocorrelation of seismic time-series recorded by geophone 3 located immediately above the soil sample zone and filtered between 80 and 120 Hz. a) Causal part of the autocorrelation (the acausal part is symmetric). b) Maximum *cc* values of each autocorrelation. *cc* values below 0.18 were discarded and are represented by small white-filled circles. Monitored and observed events are indicated by red dashed lines. 116

Figure 4-11: The different stages of internal erosion interpreted from seismic monitoring. The time lag from autocorrelation is represented as a slowness (the inverse of velocity) to present a trend similar to the cumulative number of seismic events. 119

Figure B-1 A to F: Visualization of the seepage of water in the soil medium showing the air bubbles exiting the soil through pores 143

Figure C-1 Analysis of the horizontal geophone (geophone 19); A- Flowmeter measurements with time, B- Filtered seismogram in the 90 - 120 Hz band frequency and C- the PSD of geophone 19 at 100 Hz; the grey data represent the unsmoothed PSD whereas the red data represent the smoothened data 144

List of Tables

Table 2-1 Geotechnical properties of the sand 49

Table 2-2 The corresponding shear wave velocity (V_s) profile. 57

Table 3-1: Summary of the experiment stages 72

Table 4-1: Statistical results of synthetic and experimental inversions of electrical resistivity data. RRMSE: relative root mean square error. 103

Table 4-2: Inversion results of the synthetic dataset. Resistivity of the concrete and of the soil sample in the numerical model were initially set to 500 and 300 Ω.m, respectively. 103

Table A-1 Rate of development and detectability of internal erosion through the embankment (Fell et al., 2015) 134

Table A-2 Rate of development and detectability of internal erosion through the foundation, and from the embankment to the foundation (Fell et al., 2015) 135

Table A-3 Rate of development and detectability of internal erosion into and along conduits or adjacent walls (Fell et al., 2015) 136

INTRODUCTION

A dam is a structure used for flood prevention, water storage for household and irrigation purposes, hydropower and recreation. The types of dams differ according to the material of construction, their design, their construction, the way they resist forces and their cross-section: earth dams, rockfill dams, gravity dams among others. Dams exist in different sizes but due to the higher risk caused by larger dams, the International Commission On Large Dams (ICOLD) database consists uniquely of large dams that are 15 m high or greater from lowest foundation to crest or a between 5 m and 15 m high impounding more than 3 million m^3 of water (*ICOLD*, 2020). The ICOLD database comprises 58,713 registered large dams worldwide, 65% of which are earthen dams (37,984 dams). In France, 30% of the constructed dams are earth dams (*CFBR, 2012*).

15% of the population around the globe will be living in areas at risk of flooding by 2050; in Europe alone, over 45 flooding events took place between 1950 and 2005 (Tourment et al., 2018). Flooding could be the result of water level rise in seas, rivers or lakes due to heavy rainfall or extreme snow melt but the most catastrophic floods are the ones involving the breach of water retaining structures (Van Beek et al., 2015). Despite their common use because of their ease in construction, earth dams are at risk of failure. A study conducted by Foster et al. (2000b) on large embankment dams up to 1986 excluding large dams constructed in Japan before the year 1930 indicates that 48.4% of the dams failed due to overtopping (Figure 1a) and 46.1% was due to piping (Figure 1b) (i.e. of which 30.5% through the embankment). Available statistics show that piping is the most frequent type of failure in embankment dams (Deangeli et al., 2009; Foster et al., 2000b). Foster et al. (2000b) showed that piping (induced by internal erosion) is almost accountable for one-half on embankment failures. They also specify that about 1 in 200 dams fail due to piping and 1 in 60 dams have had a piping incident. Piping is the result of the continuous

erosion of soil particles in the body of the dam (i.e. internal erosion) that will be carried downstream by seepage flow until a pipe is formed. This phenomenon may lead to breach and failure (Parekh, 2016).

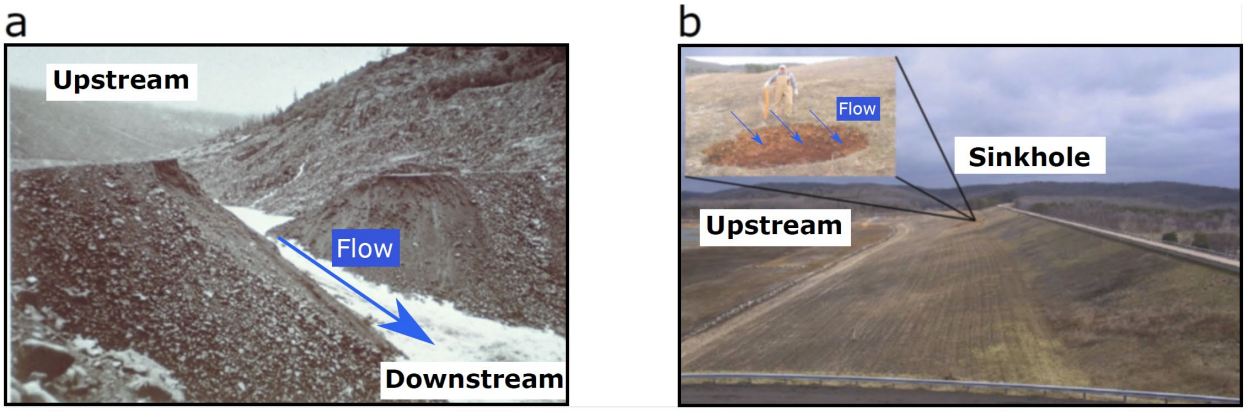

Figure 1: Photographs of Dam failure – a. represents the failure of the Hell Hole Dam in California USA in 1964 due to overtopping (Failure of Hell Hole Dam – Geotechnical Photo Album) and b. represents a sinkhole that was developped due to piping failure and internal erosion of the embankment into the foundation (FEMA, 2015).

Up until mid-1980's, the use of anti-seep collars (i.e. impermeable diaphragms of mostly metal and concrete) was the approach used during the construction of earthen dams to prevent internal erosion (FEMA, 2011). This approach was not fully successful and new proper designs against internal erosion have been established through the use of properly designed filters to stop the erosion (FEMA, 2005, 2011, 2015); however, old structures that are still operating are still susceptible to internal erosion mechanisms (Robbins and Griffiths, 2018). The degradation of the dam materials (i.e. concrete, masonry or soil) makes the structures more prone to failure (Adamo et al., 2020a). For example, in the U.S., 85% of the existing dams have already exceeded their 50-year design in 2020 which raises the question about their performance (Parekh, 2016);

Throughout the years, multiple earth dams have failed leading to catastrophic fatalities and major economic losses such as the Baldwin Hills dam. It failed and resulted in the release of a huge amount of water (250 million gallons) which ended up killing 5 people and resulted in damage losses approximated at $ 11 million. Engineers inspecting the site revealed that the problem was with the land where the dam was built in addition to cracks found in the asphaltic liner which allowed the water to enter and erode the materials (Barnes, 1992; Sharma and Kumar, 2013). The visual inspection of the caretaker led to the detection of the anomalous water seeping from the dam.

Also, in 1976, the Teton dam located in Idaho, USA collapsed several hours after detecting the muddy seepage due to internal erosion. The breach led to the death of 11 people in total and around $ 400 million in losses. Following the inspections, the main cause of the failure was the cracks that developed in the impermeable core of the structure (Barnes, 1992; Graham, 2008; Sharma and Kumar, 2013).

Then in 1997, the Anita embankment dam in Montana, USA failed. It is designed of a homogeneous fill of Lean Clay and a riprap at the upstream. In 1997, a leak was detected beside the outlet conduit. Leakage and water from the outlet conduit were approximated at 400 cfs which was larger than the designed capacity. 36 hours after the initiation process, the dam was empty. It did not completely fail. Investigations showed that the type of materials used in the embankment dam (mainly lean clay) were dispersive; in addition to the poor compaction around the conduits which caused internal erosion and leakage in the dam (Calamak and Yilmaz, 2018).

Even the failure of small earth dams could lead to catastrophic consequences. In a mountainous village in Lebanon, Aqoura, there exists over 15 reservoirs that are constructed using natural soil and an empirical trial and error engineering approach without the application of engineering designs. In 2015, two reservoirs collapsed due to overtopping (heavy rainfall and poor design of the capacity) and piping (Figure 2) resulting in major losses of agricultural lands and heavy machineries (*The Daily Star - Lebanon*, 2015). Luckily, no deaths were reported but questions were raised about the stability of the remaining reservoirs that could be prone to failure at any time.

Figure 2: Aqoura reservoir breach in 2015 caused by the collapse of the earth embankment due to internal erosion (*The Daily Star - Lebanon*, 2015).

Finally, the failure of the upstream tailing dam which was constructed in 1976 in Brazil. On January 25, 2019, the dam collapsed causing the death of more than 259 people. It was monitored using satellite-driven soil moisture index, multispectral high-resolution imagery and Interferometric Synthetic Aperture Radar (Lumbroso et al., 2021; Silva Rotta et al., 2020) According to the studies done on the Brumadinho dam, the increase in moisture content on the surface of the dam with time have led to its collapse.

In addition, some earth dams have experienced internal erosion mechanisms that have been stopped prior to reaching failure such as the Rhone delta dams located in France. They were subjected to internal erosion without them leading to failure from 1840 up until 2016 (Mallet et al., 2019). Also, the Oroville dam that is located in California, USA. It is considered to be the tallest dam in the USA with a height of 770 ft. In 1997, the service spillway flow was around 52,500 cfs when it suddenly failed and led to the removal of a concrete section of the chute. This incident led to internal erosion in the foundation of the dam and progressive failure of the chute slab in the upstream and downstream directions. The Oroville dam incident is considered to be one of the gravest dam safety incidents in United States history (France et al., 2018).

The consequence of a dam failure is mainly the potential loss of lives that is very dependent on the available time to evacuate areas at risk (i.e. downstream) (Fell et al., 2003; Graham, 1999); therefore, it is very crucial to detect internal erosion at its first stages (FEMA, 2015; Graham, 1999; Parekh, 2016). Several researches have focused on finding the probability of dam failure (Foster et al., 2000a; Foster and Fell, 1999) by dividing the internal erosion mechanism into four categories and determining the time of each phase (Bonelli, 2013; FEMA, 2015; ICOLD, 2017; Robbins and Griffiths, 2018; Wan and Fell, 2004). In addition, the FEMA issued in their 2015 bulletin techniques that are used to monitor and detect internal erosion. Initially, visual inspection was conducted to detect anomalous seepage zones in low hazard potential dams. It relied on the detection of surface discharges, surface deformations among others (FEMA, 2015). In the case of higher hazard dams, greater instrumentation was required to quantify the seepage. The use of non-destructive techniques was not widely used previously because dam engineers were doubtful concerning their effectiveness.

In the past decades, geophysical techniques (i.e. electrical resistivity, self potential, electromagnetic profiling, seismic, remote sensing among others) have been extensively introduced in the monitoring and detection of anomalies in the body of the dam (Adamo et al., 2020b; de Wit and Olivier, 2018; FEMA, 2015; Fisher et al., 2017; Guireli et al., 2020; Ikard et al., 2015). Although designs of earth dams have evolved to take into account internal erosion and new monitoring techniques have been implemented in order to detect internal erosion yet earth dams are still failing leaving behind a large number of fatalities, huge economical losses and waste of water resources and infrastructures. Hence the problem still exists and raises the following questions: Is it possible to detect internal erosion at its early stages to prevent massive damages using electrical resistivity and seismic techniques? How does monitoring of seismic noise and electrical resistivity bring us one step closer into understanding the mechanism of internal erosion?

Up until today, there is not a full understanding about how internal erosion could be detected in earth dams and what is the best technique to monitor these structures that would be able to confirm the initiation of internal erosion and its evolution in order to alert well ahead of time areas situated at a high risk zone. In order to better assimilate the effectiveness of electrical resistivity and seismic

techniques in monitoring water seepage in porous media and internal erosion, this thesis focuses on the application of both methods on controlled laboratory setups and field sites.

For this purpose, two types of experiments were conducted: first, controlled laboratory experiments to better understand the mechanism of internal erosion and water seepage under controlled environment. Second, a field testing which was conducted on an experimental dam in Rouen, France.

Chapter 1 of this thesis is a state of the art explanation about the mechanism of internal erosion. It highlights the different types and different stages of internal erosion. It indicates where it is initiated and how it progresses towards failure. Furthermore, this chapter summarizes the techniques used to monitor earth dams in the objective of detecting internal erosion. The overall literature review presented in Chapter 1 determines the extent of knowledge about internal erosion and what is still missing in order to reach a full monitoring system that would detect internal erosion at its initial stages.

Chapter 2 explains the experiment conducted on an experimental dam in Rouen, France. This experiment targets a forced water flow inside a high permeability channel of gravels embedded inside a low permeability dam. This test was conducted to understand the effect of water seepage solely on electrical resistivity and seismic techniques.

Chapter 3 tackles the laboratory experiment conducted at Notre Dame University – Louaize, Lebanon. It was designed to allow water seepage inside a soil sample uniquely under varying water heads. Continuous monitoring using electrical resistivity and seismic techniques were implemented on this laboratory setup to detect changes that occur due to the water seepage and the quantification of the flow rate in the porous medium.

Chapter 4 is a dedicated to the entire evolution of a soil sample starting from water seepage all the way to the initiation of internal erosion until the failure. It was conducted using the same laboratory setup for the monitoring of water seepage. Both electrical and seismic techniques were implemented to monitor the evolution of the soil sample in addition to video monitoring that allowed to better understand the changes seen in the data.

Finally, chapter 5 is a conclusion about the experiments that were conducted in this thesis and it also presents the perspectives for future work.

CHAPTER 1
State of the Art

Internal erosion is one of the major causes of failure of earth dams. This chapter will present the mechanism of internal erosion and its different stages before reaching the breach of the earth dam. Moreover, conventional monitoring and detection techniques of internal erosion will be presented. It will also be dedicated to the geophysical techniques (electrical resistivity and seismic methods) used in the scope of this thesis as well as previous studies conducted using these techniques in the laboratory and in the field.

1.1 Earth dams

The main purpose of building dams historically was for water storage due to water scarcity for irrigation purposes (Engemoen, 2014). Sadd–El–Kafara is the first known dam to be built and used in Egypt around 2,900 B.C. (Wiltshire, 2002). With the increase in population, the need for additional water supply that would overcome the dry seasons has become essential (Stephens, 2010). According to the United Nations, 700 million people could be displaced because of lack of water (United Nations, 2019). With time, dams became not only a structure to store water but also for flood prevention, hydropower electric production and recreation areas. The past failures of embankment dams (that were previously built by experience and precedence) took a turn in the way they are designed in the 1930's with the rapid advancement in geotechnical testing and soil mechanics (FEMA, 2015; Engemoen, 2014).

Earth dams are the oldest types of embankment dams built with natural resources and primitive equipment (Garg, 2002). The Association of State Dam Safety Officials (ASDSO) defines earthen dams to have 50% of the total volume as compacted earth layers that are generally smaller than 3-inch size (ASDSO, 2021). According to ICOLD, earth dams constitute 65% of 58,713 dams worldwide (*ICOLD*, 2020). They are divided into 3 subcategories. First, the homogeneous embankment dams that are the oldest type of embankment dams (Deangeli et al., 2009; Sjödahl et al., 2008; Stephens, 2010). They are usually designed for low to moderately high dams (Garg, 2002). They consist of one type of low permeability material throughout the body of the dam (Garg, 2002; Sjödahl, 2006). Figure 1-1A represents a typical homogeneous dam. A drainage towards the downstream is in place because homogeneous dams are prone to problems of seepage. The drainage channel makes sure the seepage is well inside the body of the dam to prevent piping and instability (Garg, 2002; USACE, 2004). Second, the zoned embankment dams that are specifically for the design of larger dams (Figure 1-1B) (Stephens, 2010). Compared to the homogeneous dams, they are more costly but ensure lower seepage hazards due to the central impervious core surrounding the outer zones providing the structure's stability (Deangeli et al., 2009; Garg, 2002; Stephens, 2010). The integration of the core inside the embankment dam helps in decreasing seepage due to its low permeability compared to the fill materials (Nayebzadeh and Mohammadi, 2011). In case of abrupt change in the materials properties between the central core and the outer zone, a filter is required as a transition zone to prevent piping through cracks that might develop in the core (Garg, 2002). And third, the diaphragm earth dams that are built with pervious materials (i.e. sand, gravel or rock and in this case it is called a rockfill diaphragm dam). A thin diaphragm is incorporated either at the center of the structure or at the upstream side as a blanket to control the seepage (USACE, 2004). The impervious materials used for the diaphragm dam are impermeable soils, cement concrete or bituminous concrete among others. Figure 1-1C shows a schematic of a diaphragm earthen dam.

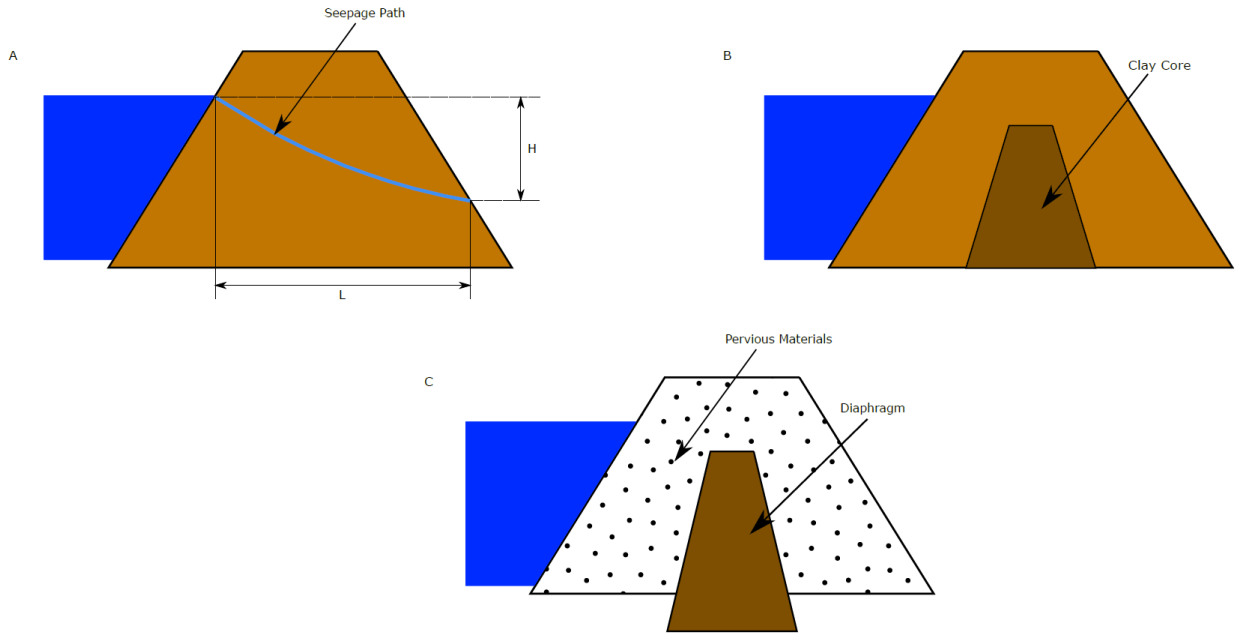

Figure 1-1: Different types of earth dams; (a) Homogeneous dam made out of impermeable material showing the seepage path and its length (L) with the differential head (H), (b) Zoned dam consisting of a core of lower permeability than the body of the dam and (c) Dam structure consisting of pervious materials and an impervious diaphragm at the center.

1.2 Internal Erosion Mechanisms

Internal erosion (also known as piping) is defined as the process of soil particles detachment and erosion below the surface caused by the seepage of water in the earth dam or through cracks[1]. The water seepage through the cracks must be of sufficient high velocity to pull out the soil particles from the soil matrix. Fell and Fry (2007) distinguished three classes of soils vulnerable to internal erosion. The first category consists of the non-plastic soils referring to cohesionless soils such as silt, sand, silty sand and gravel soils. These types of soils tend to collapse when they are saturated thus not withstanding a crack. They are easily eroded. The second category are plastic soils as in clays, clayey sands and clayey sandy gravels that resist erosion more than non-plastic soils. Considering their cohesive properties, these soils can retain a crack even if they are saturated; thus, higher energy is needed for particles to get removed and carried through the cracks. Finally, the third category is the dispersive plastic soils which differ from the plastic soils by their clay mineralogy and the water chemistry.

In addition to the effect of soil properties on the likelihood of internal erosion, the hydraulic conditions also affect the beginning of piping. Bligh (1910) introduced the percolation factor, *c*,

[1] Crack is intended in the geotechnical meaning: a fissure

which is defined as the minimum critical ratio between the seepage length L (m), and the differential head, H (m), for the initiation of internal erosion:

$$\frac{L}{H} = c \quad (1)$$

Multiple researchers have studied the effect of the hydraulic gradient on the initiation of internal erosion until Terzaghi and Peck (1948) defined the critical hydraulic gradient as follows:

$$i_c = \frac{G_s - 1}{1 + e} \quad (2)$$

Where i_c is the critical hydraulic gradient, G_s is the specific gravity and e the porosity. The value of i_c in this equation is approximated to 1 for the initiation of the internal erosion and not for the calculations of hydraulic gradients following internal erosion mechanisms. Although further laboratory studies have shown that the critical hydraulic gradient is lower than 1, nevertheless, equation (2) is still used as an approximation (Rice and Swainston-Fleshman, 2013).

Terzaghi et al. (1996) introduced the failure of dams by the formation of a pipe between the soil and the foundation They differentiated two types of failures due to piping. The first type of failure is by subsurface erosion (also referred to as scour) which begins at the downstream toe and reaches the upstream; and the second type of failure is by heave which is caused by the high-water seepage pressure that infiltrates beneath the downstream toe that is larger than the effective weight of the soil. This concept was elaborated and the mechanism of internal erosion in embankment dams is now divided into three general failure modes depending on the location where internal erosion starts (Fell et al., 2015). It could be initiated in the embankment (Figure 1-2a) including those also happening in through-penetrating structures, known as conduits. They are related to the outlet, spillway walls or other structures supporting the embankment dam. It could also take place in the foundation of the embankment (Figure 1-2b), or in the embankment into the foundation (Figure 1-2c). This type of internal erosion includes the seepage that washes away particles into the foundation or at the contact between the foundation and the embankment itself.

Foster and Fell (1999) integrated a four-stage process for the mechanism of internal erosion in embankment dams illustrated in Figure 1-2 (Foster and Fell, 1999). Stage 1 is the initiation of erosion: this stage starts by one of the following types of internal erosion: concentrated leak, suffusion, contact erosion or backward erosion (Bonelli, 2013). Stage 2 represents the continuation of erosion: in this stage, four scenarios are possible to happen and that is dependent on the gradation of the soils, the existence of filters and their design (Fell et al., 2015). Internal erosion will either stop, or it will continue and then stop leading to minor erosion, or it will stop following excessive erosion or finally it will continue and move to the next stage. Stage 3 is the progression of erosion. This stage depends on the types of soils whether it can retain a pipe or soils from the upstream will be washed away into the eroded zone and stop the erosion or the soils at the upstream will limit the seepage of water to reach an equilibrium. Finally stage 4 which is the breach of the earth dam: four different types of breach may take place (Fell et al., 2015). First is the gross

enlargement of the pipe, second is the unravelling of the toe, third is the crest settlement, or sinkhole on the rest leading to overtopping and four the instability of the downstream slope.

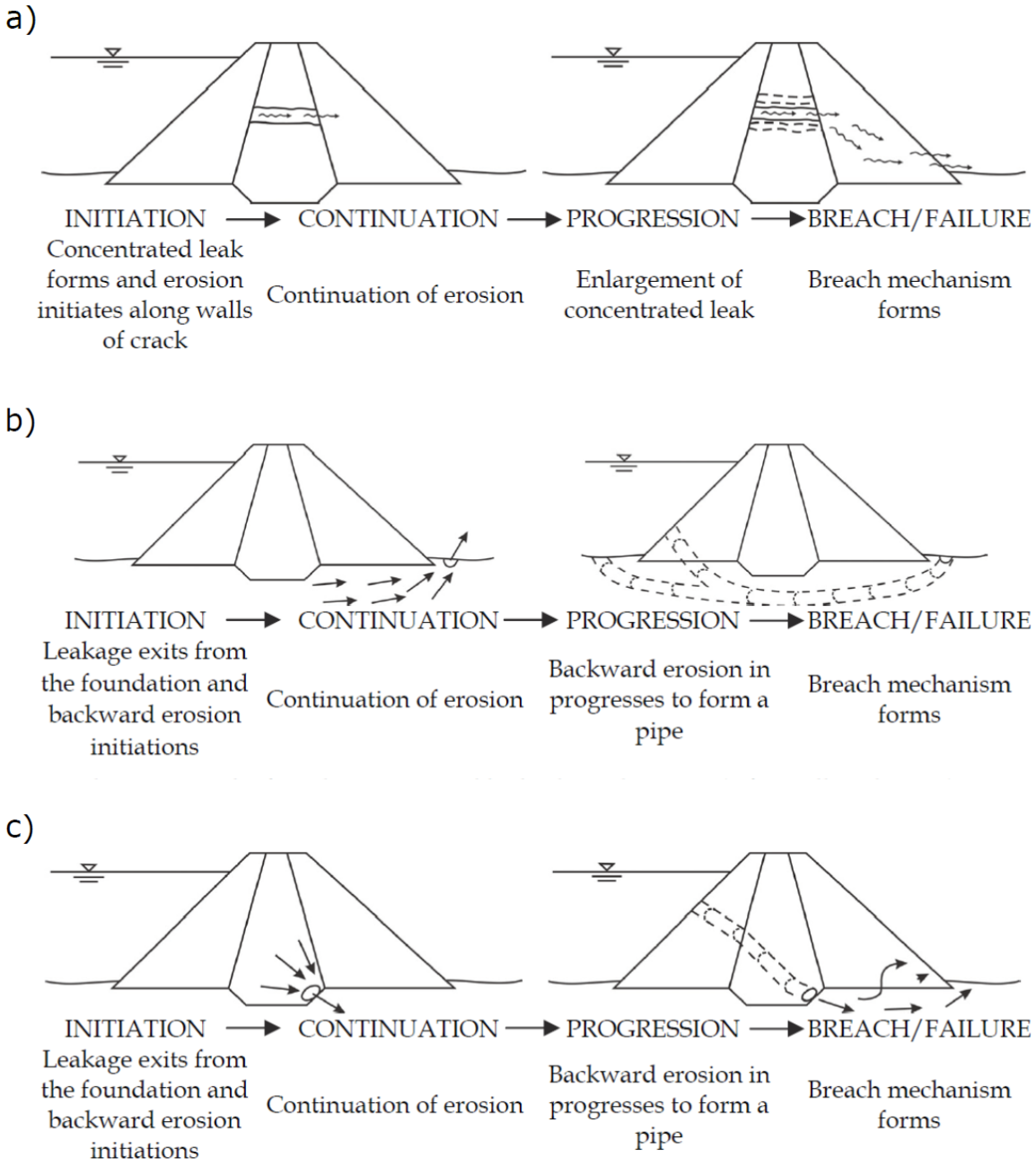

Figure 1-2: The four-stage of internal erosion mechanism depending on their location; a. Internal erosion in the embankment initiated by concentrated leak, b. Internal erosion in the foundation initiated by backward erosion and c. Internal erosion from the embankment to the foundation initiated by backward erosion (Foster and Fell, 1999)**.**

1.2.1 **Concentrated Leak Erosion**

This type of erosion happens in plastic or dispersive plastic soils through cracks or hydraulic fractures which are due to the differential settlement of the dam during construction or when it is in operation (Figure 1-3). The poorly compacted fill in the embankment, around conduits and adjacent walls lead to the collapse of settlement which creates cracks that act as open paths for water. Four factors determine whether internal erosion will take place or not (Bonelli, 2013; Fell et al., 2015). The first factor is whether the soil can hold a pipe. The second one is the existence of zones upstream and sometimes downstream that might limit the hydraulic gradient therefore the internal erosion process is limited. The third factor is the existence of filters that might stop the internal erosion process. Finally, the fourth is the swelling type of soil that might close the cracks and therefore the water seeping will be insufficient for internal erosion to progress.

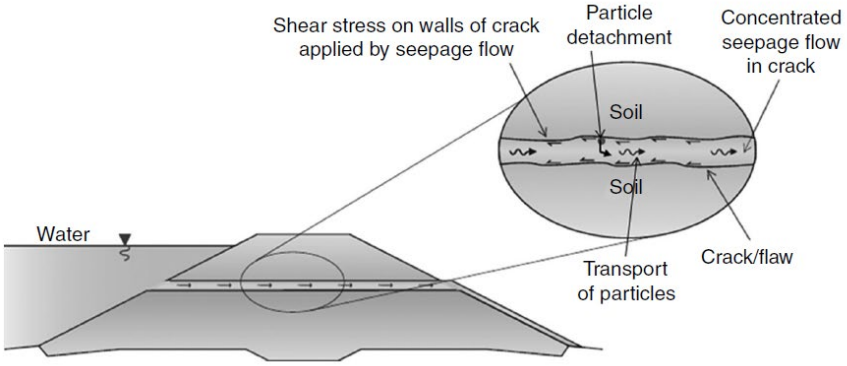

Figure 1-3: Internal erosion initiated by concentrated leak. The close-up shows the pipe that has formed and the detachment of soils particles that are migrating towards the downstream (Fell et al., 2015).

1.2.2 **Backward Erosion**

Backward erosion is experienced in non-plastic soils or plastic soils at higher hydraulic gradients (Bonelli, 2013). It is divided into two types. The first type is the global backward erosion which is the development of a vertical pipe in the core of the embankment and the second type is backward erosion piping which starts at the downstream side of the embankment dam. It is initiated at the downstream toe where the hydraulic gradients are critically high to a point that particles start eroding upwards or horizontally in the case of non-plastic soils. The process continues beneath the embankment dam forming small channels where water transports the eroded soil particles. For this to happen, the soils of the structure should retain the roof of the pipe without any collapse thus the name piping. The detection of backward erosion is usually revealed by the appearance of sand boils downstream (Fell et al., 2015). Sellmeijer et al. (2011) illustrated the process of internal erosion by backward erosion as shown in Figure 1-4 which starts by the observation of a heave downstream that will lead to seepage and the formation of the pipes until reaching the failure.

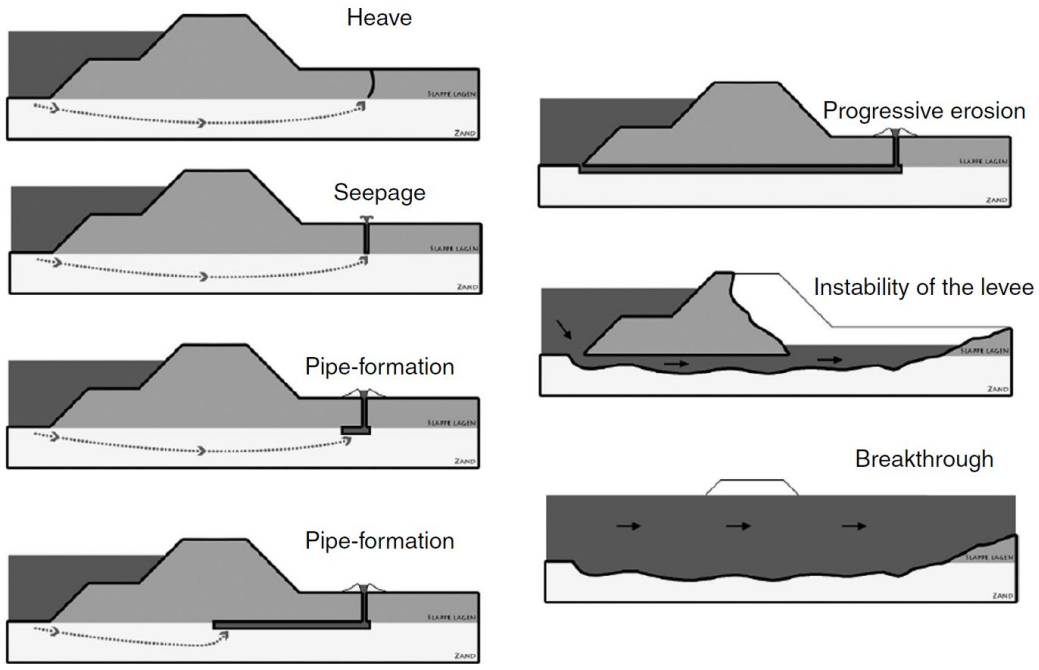

Figure 1-4: Internal erosion initiated by backward erosion piping formed in the foundation of the earth dam – the line represents the seepage path and the pipe is represented by the rectangle (Sellmeijer et al., 2011)

1.2.3 **Suffusion**

Suffusion is the type of internal erosion initiated in the presence of gap-graded cohesionless soils in the embankment cores. The seepage of water causes the small particles to be transported in the pores of the coarser particles which will not be detached. Three criteria should be satisfied for suffusion to occur. First, the size of the fine particles should be less than the size of the constrictions between the larger particles. Second, the amount of fine materials should be less than what is required to fill the voids in the coarser particles leading to the transfer of the effective stresses to the coarser materials. Consequently, fine particles are free to move with the seepage flow. Third, the velocity of the seepage flow should be higher than the weight of the soil particles in order for the particles to overcome the constrictions of the coarser particles and move.

1.2.4 **Contact Erosion**

This type of internal erosion takes place at the interface between a coarse soil such as gravel and a finer soil. The flow seeping parallel to the contact between the coarse particles and the fine particles will erode the fine materials.

1.3 Monitoring and Detection of Internal Erosion

The detection of internal erosion is difficult due to the variety in the piping mechanism. It could be very quick (less than an hour) for a homogeneous embankment dam to collapse due to the presence of cracks in its structure or due to holes dug by animals (ICOLD, 2017). In 1999, the US Bureau of Reclamation suggested a minimum of one hour as a warning time of failure in order to have a significant effect to reduce the number of casualties (Fell et al., 2003). A study was conducted by Fell et al. (2003) on the development time of internal erosion in which they studied previous failure cases. The two phases were not divided because of the complexity of differentiating them when relying on observation. Therefore, continuous monitoring of embankment dams is very crucial in order to detect internal erosion in early phases. Consequently, Fell et al. (2008) came up with a method to identify the likelihoods in detection of internal erosion and the successful intervention. The results of their study are shown in Appendix Table 1-1 for internal erosion in the embankment fill, Appendix Table 1-2 for internal erosion in the foundation and from the embankment to the foundation and Appendix Table 1-3 for internal erosion into and along conduits or adjacent to walls. The authors use the terms Slow (S) for a timeframe of weeks, months and even years, Medium (M) that stands for days or weeks, Rapid (R) when the time is larger than 12 hours to days and Very Rapid (VR) when it is less than 3 hours. The methods of detection and the instrumentations adopted differ in the location of the initiation of internal erosion as well as in the mechanism type. The detection techniques rely more on the identification of an increase in the water flow rather than on particular signs indicating the presence of internal erosion.

1.3.1 Visual Inspection of Internal Erosion

Visual inspection of the embankment dam is the first step towards monitoring (Johansson and Sjödahl, 2004). Regular observations of the structure even by untrained personnel can be reliable in detecting anomalies in the structure. Usually, trained engineers with previous knowledge of the dam history, look for seepage or any deformations in the embankment dam to detect early warning signs of possible internal erosion. Figure 1-5 shows the suspended sand detected visually on the downstream of an embankment dam indicating the presence of internal erosion. Sometimes, video cameras are installed along the conduits for monitoring (FEMA, 2015).

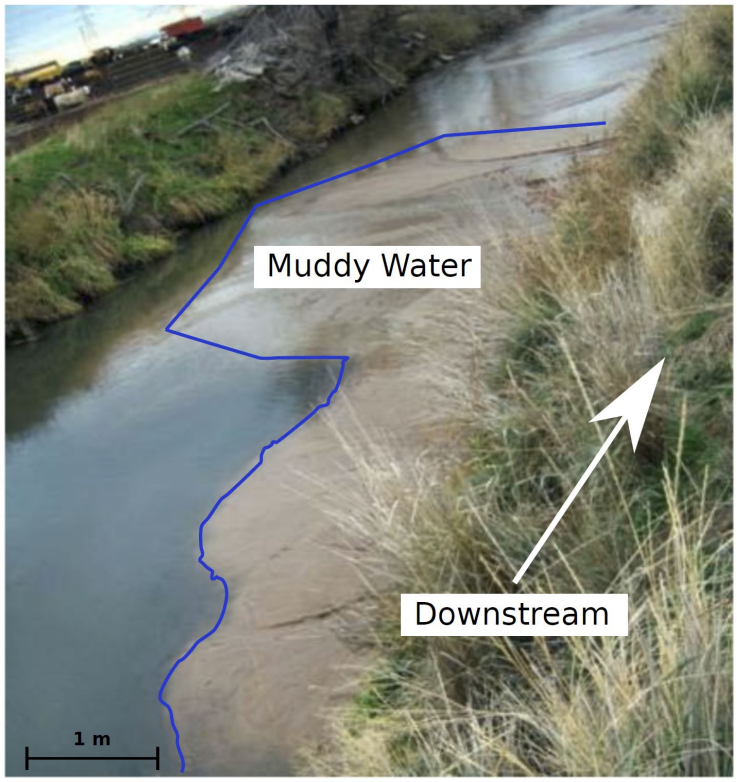

Figure 1-5: Visual observation of the mud water at the downstream of an embankment dam (FEMA, 2015)**.**

Following the observation of seepage and identifying its location, it is crucial to monitor the seepage by measuring the flow and determining its quality (eroded materials). Surface discharges are generally classified into seeps or boils. The discharge is considered to be a seep discharge when the total head is equal to the elevation (i.e. the velocity head is negligible and the pressure head is the atmospheric pressure) when the seepage is more active, the discharge is considered to be a boil and the velocity head is not neglected. In this case, there is enough energy in the flow that would lead to the detachment and transport of soil particles (FEMA, 2015).

A seep is identified by the presence of vegetation. It should be monitored by indicating its boundary, type of vegetation present, its turbidity, the quantity and the size of the wet area. The seepage gradient, which is the difference in total head divided by the seepage flow path, should also be calculated. In case the seepage gradient increases due to an increase in the total head and there is evidence of particles in the discharge, the seep might initiate internal erosion.

Boils are indicative of on-going internal erosion. The high velocity of the seepage leads to the transport of coarse particles, thus the nomenclature sand boils. They take place when the reservoir is at high levels. The existence of boils is indicative of flow paths that have already been formed inside the body of the dam. Sand boils should be monitored and checked regularly for location, quantity and content of the seepage, the area of seepage and the reservoir level.

In addition, the deformations experienced in the embankment dam can indicate the presence of internal erosion but is not always the case. Surface deformations can be manifested as sinkholes, slumps, cracks, depressions and cavities (FEMA, 2015). When deformations are present above conduits or penetrations usually indicate that internal erosion is taking place and require prompt action.

1.3.2 **Geotechnical and Hydraulic Monitoring**

1.3.2.1 Seepage Monitoring

Seepage measurement is very important in assessing the performance of embankment dams. Therefore, close monitoring of flow rates and transport of materials is a direct indication of internal erosion. Increase in flow rates indicate an enlargement of the flow path in the dam or the development of new paths. The use of a bucket and a stop watch is a primitive way of determining the flow rate. More complex systems include the use of weirs (i.e., rectangular or V-notch), flumes and velocity meters. Sediment traps are also used to monitor the quality of the water for potential particles transport. The use of turbidity meters, pH probes and thermal network inside the body of the dam could aid to identify changes that might correlate to seepage paths (Beck et al., 2010; Johansson and Sjödahl, 2004).

1.3.2.2 Water Pressure Monitoring

Water pressure monitoring is intended to give more information about the changes in the hydraulic parameters of the dam (Pagano et al., 2010). It identifies the presence of cracks and erosion problems. The use of piezometers in embankment dams is not very helpful in identifying internal erosion because the piezometers are installed at a specific location and acquire data for a specific point which in most cases is not along the seepage path (Engemoen, 2014).

1.3.2.3 Deformation Monitoring

Deformation monitoring (i.e. settlement sensors, inclinometers or tiltmeters and geodetic) is used to identify slope instability, settlements or depressions caused by internal erosion (Yavaşoğlu et al., 2018). It could also identify differential settlement that would cause cracks in the dam leading to a flow path. In addition, the detection of relative movement in the spillway or outlet structure that would create a flow path for seepage (Engemoen, 2014). Global navigation satellite system (GNSS) instrumentation has also been used for mapping surface deformations and monitoring dams (Gökalp and Taşçi, 2009; Taşçi, 2008; Yuwono and Prasetyo, 2019). Synthetic Aperture Radar (SAR), Unmanned Aerial Vehicle (UAV), remote sensing and Light Detection And Ranging (LiDAR) are new techniques that have also served as surface monitoring on different embankment dams (Evers et al., 2020; Scaioni et al., 2018; Silva Rotta et al., 2020).

1.3.2.4 Temperature Monitoring

Recently, temperature monitoring has been used for early detection of water seepage in earth dams. Even though it is biased by multiple factors such as seasonal variations, effect of temperature of

the upper layers, it is also sensitive to water leakages (Khan et al., 2014). Two types of monitoring techniques have been previously adopted. First, passive measurements that consist on acquiring the natural temperature of the saturated soil layer (Johansson and Sjödahl, 2004) and second, active measurements in order to quantify the flow in a pre-determined anomaly area. The technique relies in increasing the temperature of the surrounding soil and estimating the heat transported by the flow (Artières et al., 2007). A study conducted on the IJKDijk experimental dam, Netherlands, showed an increase in the dissimilarity values (detection parameter) two days before the rupture of the dam (Beck et al., 2010). Although the thermal monitoring did identify leakage, the process of internal erosion was not shown during monitoring. It only detected seepage of water.

1.3.3 **Geophysical Monitoring Techniques**

Multiple geophysical techniques are explained briefly in this section because they are not in the scope of this dissertation. Electrical resistivity and seismic techniques will be elaborated in sections 1.3 and 1.4 respectively because they are the methods that are used in this research.

1.3.3.1 Electro-Magnetic Induction Profiling Technique

The Electro-Magnetic Induction (EMI) technique relies on conductivity of the ground, to transmit electromagnetic energy either generated by a source or naturally existent. The outcome of the EMI technique is the apparent conductivity of the area covered by the test (Mc Dowell et al., 2002). The advantage of using EMI is the large area that can be covered during the testing (FEMA, 2015). EMI is used on embankment dams to locate anomalies in the structure such as piping and cavities through the increase in conductivity values following the increase in water content (Sentenac et al., 2018).

A study conducted by Sentenac et al. (2018) incorporated the use of 3 geophysical techniques: EMI, SP and Electrical Resistivity (ER) in order to characterize the subsurface heterogeneity and determine in an easy way zones that are prone to seepage. The surveys were conducted on the Vitineves reservoir in Czech Republic for the purpose of identifying seepage zones in order to design remediations (see Figure 1-6 for details concerning the location of all profiles). The earth dam is 150 m long and 3 m high. The surveys were conducted when the reservoir was full (09/2012) and empty (11/2012).

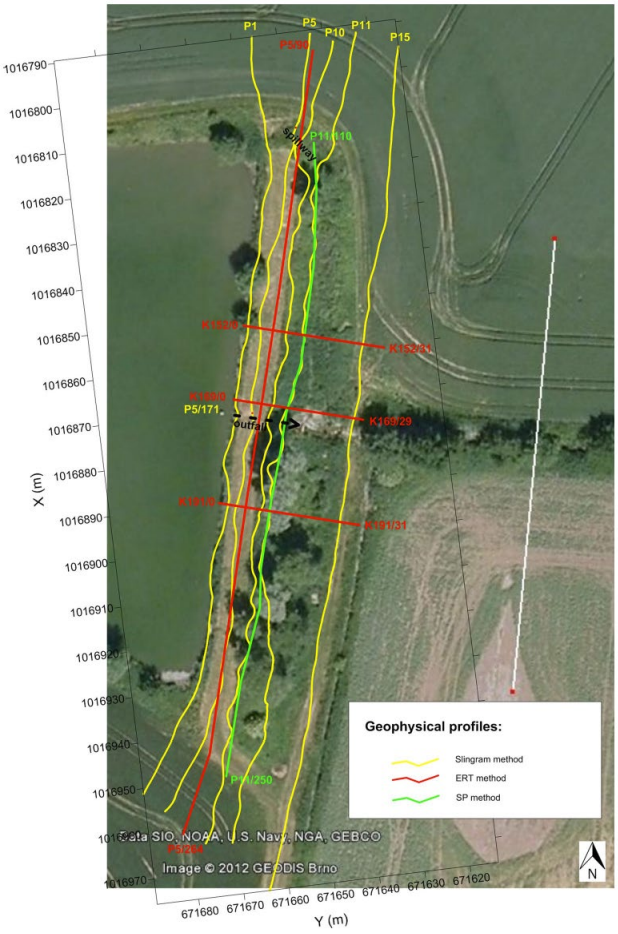

Figure 1-6: Geophysical profiles conducted on the crest of the Vitineves reservoir (Sentenac et al., 2018)**.**

The combination of the three techniques conducted on the crest allowed the determination of seepage zones while comparing the results at empty and full stages and the heterogeneities in the materials used in the body. The profile shown in Figure 1-7 shows a low apparent resistivity area in the middle of the survey highlighted by a red rectangle. According to Sentenac et al., this zone is identified as a probable area of seepage since it seems to exhibit a lower apparent resistivity value (20 Ω.m) compared to the apparent resistivity of the medium (40 Ω.m).

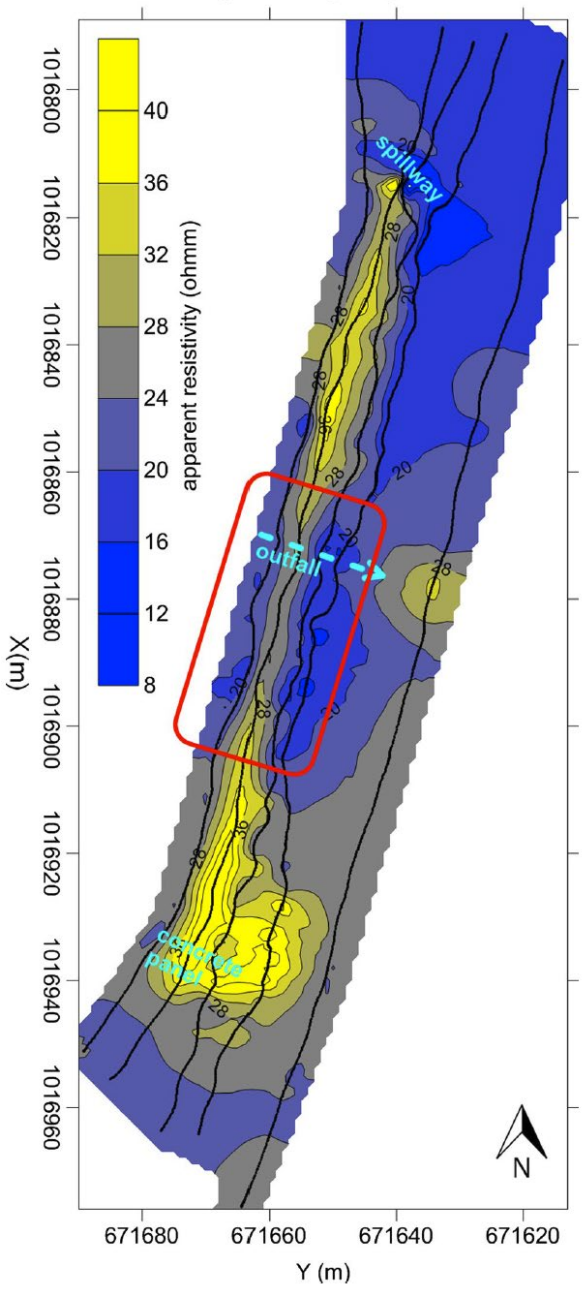

Figure 1-7: EMI results of the survey conducted on the crest of the Vitineves reservoir. The area in the red rectangle shows a low apparent resistivity identifying the seepage zone (Sentenac et al., 2018)**.**

Even though the EMI technique allowed the identification of seepage zones within conductive materials (unlike GPR), the feasibility of continuous monitoring to identify internal erosion is not yet explored and requires human intervention. Furthermore, the identification of lower electrical resistivity values does not directly mean internal erosion is taking place. It might just indicate locations of higher water content or higher clay content.

1.3.3.2 Ground Penetrating Radar

Ground Penetrating Radar (GPR) is a geophysical technique that rely on the propagation of electromagnetic waves of different frequencies (from tens of MHz to 2.5 GHz) in the ground. The waves emitted by an antenna pass through the soil until they intersect with a different layer (dielectric contrast) and partially reflect back to the receiver. GPR technique is characterized by its simplicity and the fast data acquisition but is not efficient in the presence of low resistivity materials such as clayey soils because of the high attenuation (Zimmerman and Chen, 1992). Nevertheless, it was used in a couple of studies for the detections of anomalies that are not very deep (Di Prinzio et al., 2010; Mydlikowski et al., 2007). In a study conducted by Chlaib et al. (2014), GPR was used for the identification of animal burrows, water-filled cavities and metallic objects. The survey was performed on the Lollie levee in Arkansas, USA. Figure 1-8 summarizes the results obtained from one of the surveys carried out on the crest of the levee. The anomalous zone highlighted in Figure 1-8a shows the location of the channel in the profile. Excavations at the site indicated that this anomaly in fact originated from a channel cylindrical air-filled cavity (0.1 m in diameter - Figure 1-8b) at a depth of 0.15 m from the surface (Figure 1-8c).

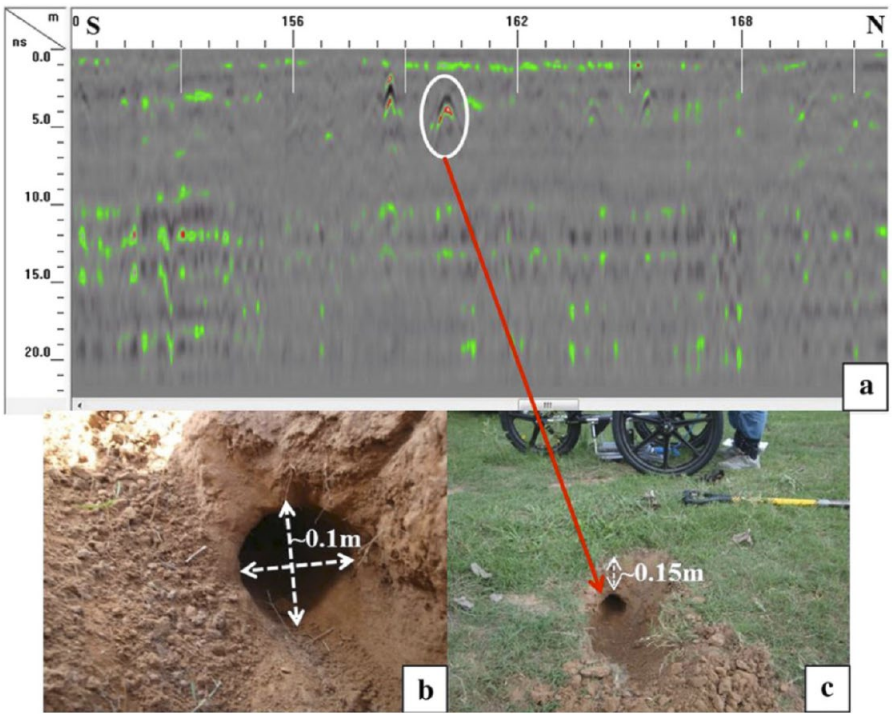

Figure 1-8: GPR survey a) results highlighting the presence of an anomaly represented by a white circle indicating the presence of an air-filled cavity, b) representing the size of the cavity, c) the location, d) lateral extension and e) the traces of claws identifying the animal scratches (Chlaib et al., 2014).

The use of GPR for shallow-depths investigations could indeed identify cavities in the structure of the earth dam. However, this technique was not used for monitoring of internal erosion.

1.3.3.3 Self-Potential Technique

Self-potential (SP) technique also referred as spontaneous potential is a passive technique that is sensitive to the groundwater flow (Boleve et al., 2011; Ikard et al., 2012; Soueid Ahmed et al., 2020). SP data acquisition relies on the use of non-polarizing electrodes. The first one being fixed at a base point and the other moving along the chosen profile that will record the electric potential generated by the fluid flow (FEMA, 2015). SP is extensively used in embankment dams for the detection of seepage (Gevaert, 2019; Heinze et al., 2019; Moore et al., 2011). The experimental setup used by Boleve et al. (2011) is shown in Figure 1-9. It represents a sand sample that was placed at the bottom with the measurement and reference electrodes located at the top and the bottom respectively. The experiment consisted on applying different heads of water to detect the sensitivity of the technique to changes in heads. The experiment was monitored using 3 electrodes: a reference electrode placed in the middle of the sand sample whereas the 2 others were located at the 2 sides (inlet and outlet sides) for timelapse SP measurements.

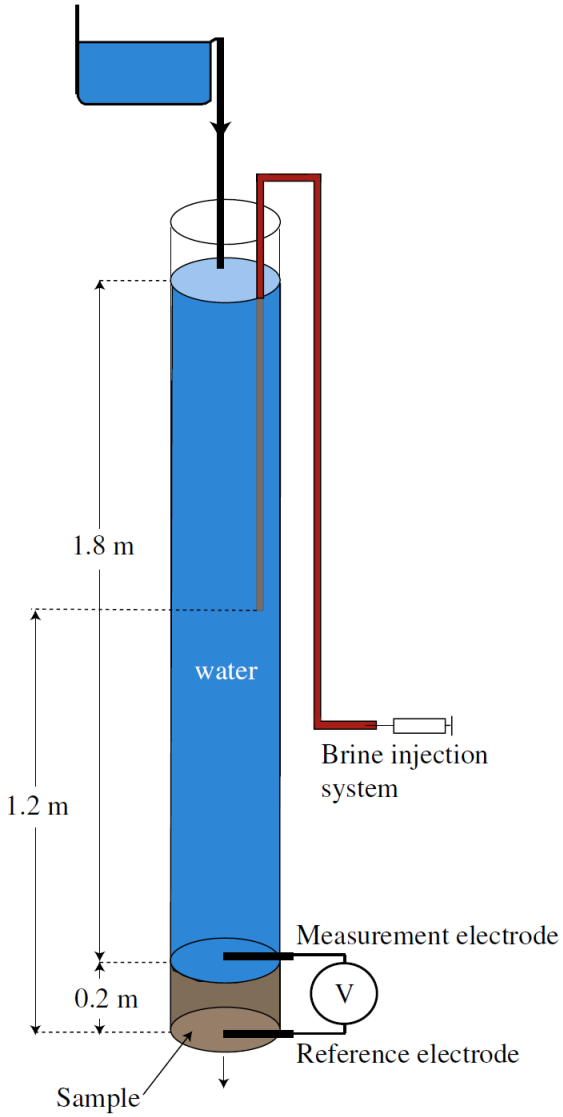

Figure 1-9: A diagram representing the laboratory setup used for the monitoring of SP of a sand specimen located at the bottom of the column. Three silver electrodes were used in the experiment to monitor SP changes throughout the brine injection (Boleve et al., 2011) **.**

Results of the SP with the increasing head of water are detailed in Figure 1-10. The plexiglass column was filled with water up to a certain head and then was left to drain. The cycle of filling/emptying was repeated for 4 different heads: 0.5, 1, 1.8 and 1.7 m denoted by the numbers 1 to 4 respectively in Figure 1-10A. As it can be seen in Figure 1-10a, with every cycle the two electrodes located at the inflow and outflow side showed significant SP variations to the changes in heads applied. The inflow/reference pair decrease with the increase in head up to the desired value and then increases again when the water in the tank is emptied (black data). The minimum SP values were dependent of the head applied. Further decreases were observed for higher heads (from -5 mV for a head of 0.5 m down to approximately -13 mV for a head of 1.8 m). On the other

hand, on the outflow/reference pair, an increase was observed when the water head was increased and then the SP value decreased gradually at the emptying phase of the experiment (Red data). The same trend for both inflow and outflow electrodes was observed at every cycle. Figure 1-10b represents the linear relationship between the maximum/minimum values of SP attained for every cycle for the outflow/inflow electrodes respectively.

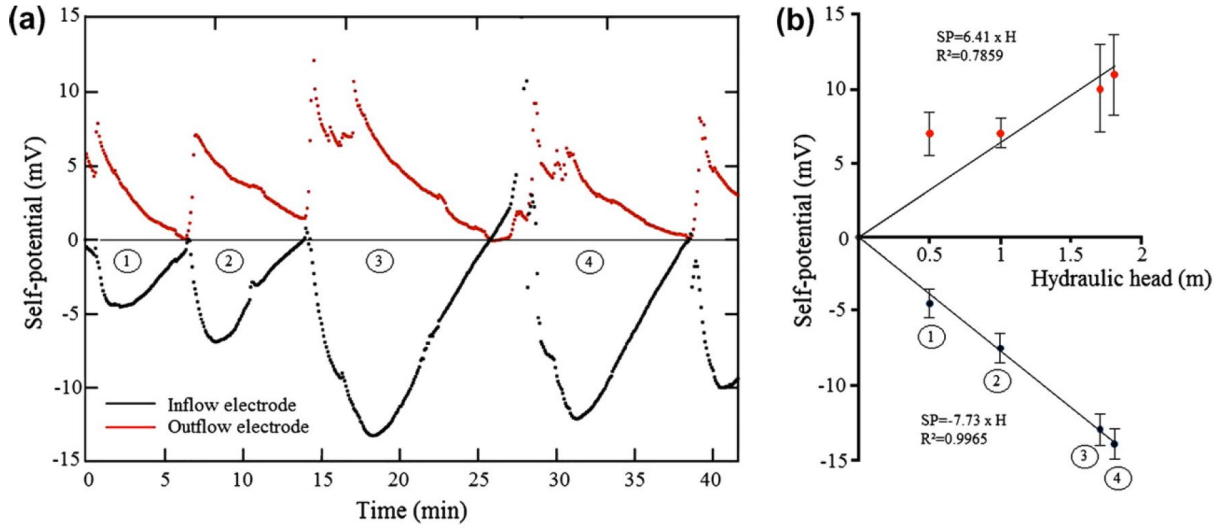

Figure 1-10: SP results reflecting the changes with time; (a) changes of SP with water head – cycles 1 to 4 are the changes of heads: 0.5, 1, 1.8 and 1.7 respectively and (b) represents the SP data with respect to changes in head highlighting a linear relationship. Data represented in black and red correspond to the inflow electrode and outflow electrodes respectively (Boleve et al., 2011)**.**

This study shows that the SP method is sensitive to the seepage of water and to the flowrate leading to different maxima or minima depending on the direction of the flow. However, the effect of internal erosion on SP values was not studied. The use of this technique focuses more on the water seepage primarily and the quantification of the flow rate.

1.3.3.4 Induced Polarization Technique

The Induced Polarization (IP) is an active time-domain or frequency domain geoelectrical method that relies on the ability of a material to reversibly store electrical energy. It acts like a capacitor. The analysis relies on the chargeability of the material which is represented by the voltage decay observed when the injected current is shut-off (Revil et al., 2012). A study conducted by Abdulsamad et al. (2019) confirmed the use of IP to detect leakages in the body of an experimental earth dam. Seven profiles at a 1.5 m spacing were used for the measurements (P1 - crest to P7 - downstream). Each profile consisted of 2 lines (one used to inject the current and the other to measure the potential) spaced at 0.20 m. Each line consisted of 32 electrodes placed at a spacing of 1.0 m as detailed in Figure 1-11.

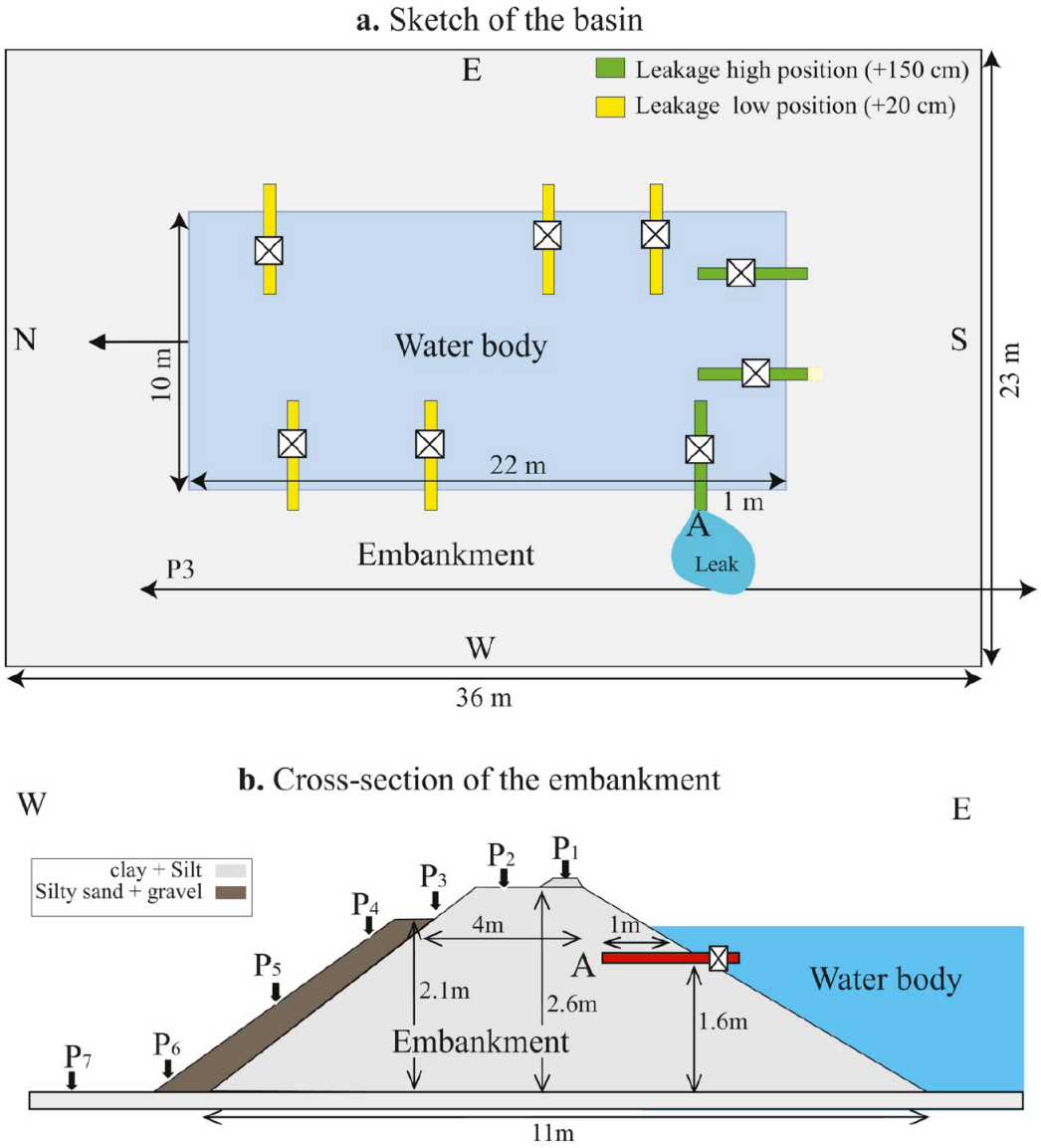

Figure 1-11: Schematics of the experimental basin; a) represents the top view and b) a side view with the locations of the profiles P1 to P7 (Abdulsamad et al., 2019)**.**

The experiment was monitored throughout the leakage. The 3D tomograms obtained following the combination of the inverted 2D data of profiles P1 to P7 are shown in Figure 1-12a and b represent the results obtained before and during leakage respectively. The elevation of 0 m represents the bottom of the embankment. The increase in the chargeability highlighted in zone B shows an increase in water content and the presence of the leakage coming from zone A in Figure 1-11a. This is due to the porosity and the cation exchange of the clay particles in the presence of water.

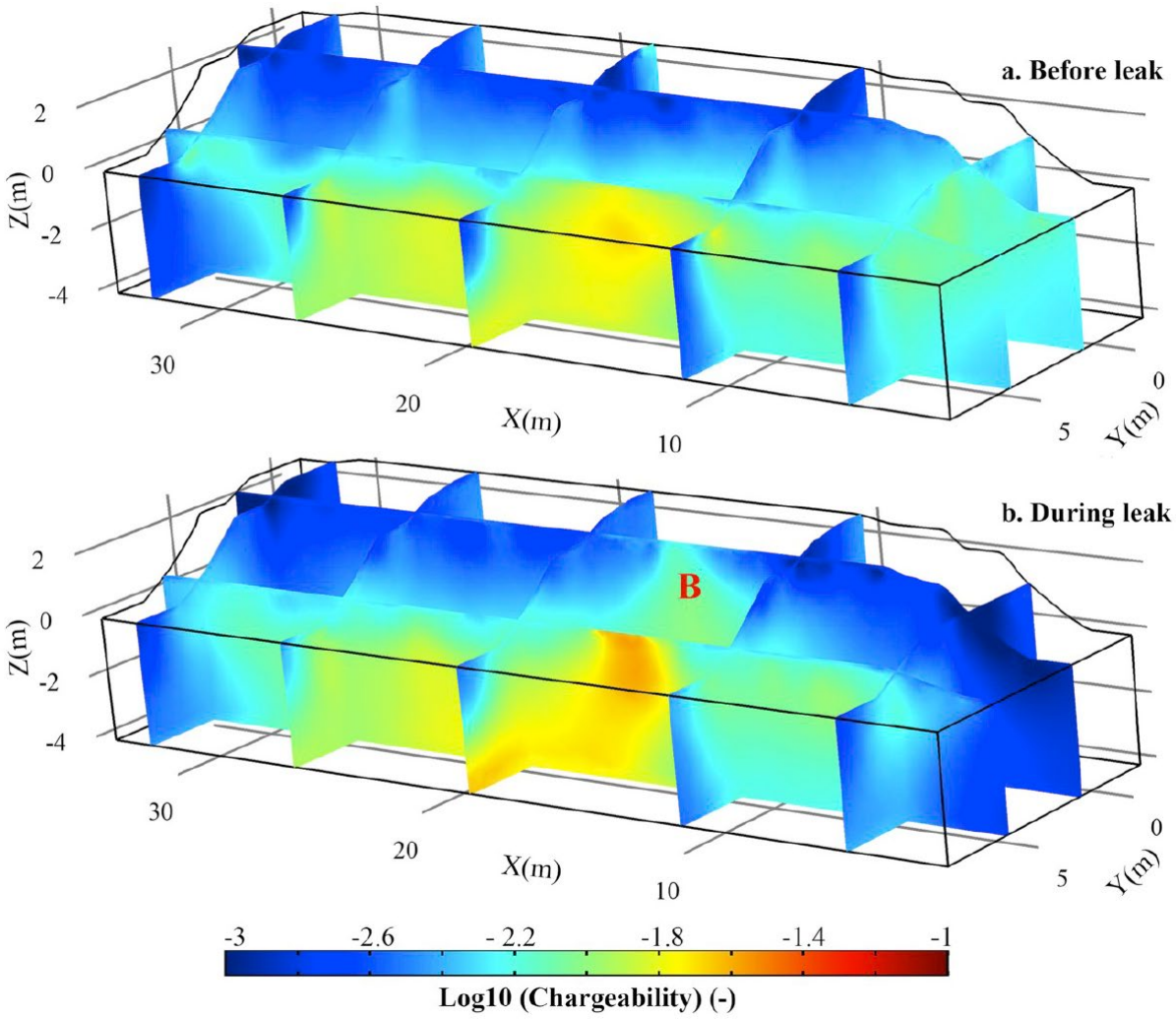

Figure 1-12: 3D inversions of the IP data acquired; a) Tomogram before the leakage started and b) Tomogram during the leakage in the basin. B represents the area with an increase in the chargeability due to the presence of the leakage in the experimental basin (Abdulsamad et al., 2019)**.**

In this experiment, IP monitoring was used for the detection and monitoring of a leakage zone in the body of the embankment. However, monitoring of the initiation of internal erosion and its effect on the chargeability was not addressed in this study.

1.3.3.5 Electrical Resistivity Technique

The concept of ER relies in injecting a current (I, A) in the ground through two electrodes and measuring the potential difference (Voltage, ΔV) using two different electrodes. The ratio between the voltage and the current would be the resistance that will be multiplied by a geometric factor *"k"* that is dependent on the geometry used for the measurements (i.e. spacing between the

electrodes) and the geometry of the body to obtain the apparent resistivity (ρ, Ω.m) (eq. 3 and 4 respectively).

$$\rho = k\frac{\Delta V}{I} \tag{3}$$

Where ρ (Ω.m) is the apparent resistivity, k (m) is the geometric factor, ΔV (V) is the potential difference and I (A) stands for the injected current.

$$k = \frac{2 \times \pi}{\left(\frac{1}{C_1P_1} - \frac{1}{C_2P_1} - \frac{1}{C_1P_2} + \frac{1}{C_2P_2}\right)} \tag{4}$$

Where k (m) is the geometric factor, C_iP_i (m) is the distance between the current and potential electrodes in Figure 1-13.

By changing the locations of the four-electrodes and their spacing, different volumes of the subsurface will be investigated. For the same acquisition configuration and number of electrodes, if the spacing between the current electrodes increase, the depth of investigation increases. If the spacing between the potential electrodes increases the resolution decreases. The apparent resistivity (ρ_a, Ω.m) obtained would be the true resistivity if the medium is homogeneous. Whereas in the case of non-homogeneous media, the apparent resistivity would be the weighted average of the resistivities of the media. Therefore, it is impossible to determine the true resistivity of a certain layer hence the use of inversions for the pseudo-section in order to estimate the true resistivities.

Electrical resistivity is widely used in many applications such as hydrogeology and groundwater exploration and the delineation of water resources to prevent their pollution from salt intrusion and other pollutants (Chambers et al., 2014; Foley et al., 2019; González et al., 2021; Hermans and Paepen, 2020; Park et al., 2016), landslides (Bellanova et al., 2018; Bièvre et al., 2021; Crawford and Bryson, 2018; Gance et al., 2016) among others. More importantly, electrical resistivity technique has been used extensively in earth dams to determine the integrity of the structure. The purpose of applying ER is to identify probable weaknesses within the body of the dam, determine the probable anomalous zones prone to seepage and internal erosion by identifying areas of low resistivities corresponding to a higher water content.

ER Data Acquisition and Processing

The array types presented in Figure 1-13 describe some different configurations. The choice of the most convenient type depends on the depth of investigation, the resolution (lateral or horizontal), signal to noise ratio among others (Sjödahl, 2006). The development and automation in the electrical resistivity technique led to the acquisition of larger sets of data that permit its use for monitoring purposes. Following data recording, a 2D pseudo-section is used to plot the apparent resistivities obtained from the field as represented in Figure 1-14 for a Wenner configuration. The apparent resistivities obtained in the field are then inverted to obtain the distribution of resistivity with depth. The mostly used type of inversion is the iterative when a model is created and is

updated for each inversion (Sjödahl, 2006). The average of the data collected from the field or a-priori data will serve as a starting model. Synthetic data are then calculated from the starting model (forward model). Then, the synthetic data are compared to the actual data obtained from the field measurements. χ^2 data misfit and Relative Root Mean Square (RRMS) error are calculated. In case the obtained χ^2 and RRMS values are not satisfactory, the starting model is modified (inversion problem) and the process is repeated until desired values of χ^2 and RRMS are obtained (χ^2 value of 1 means a perfect fit).

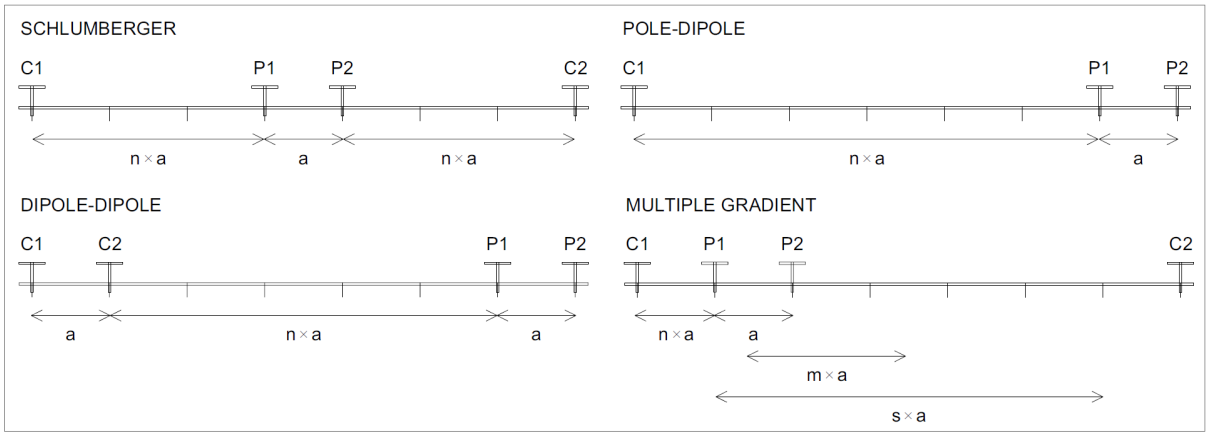

Figure 1-13: Different array types with different a-spacing corresponding to the distance between the potential electrodes and the n×a corresponds to the closest distance between the current and potential electrodes. m×a represents the midpoint distance and s determines the maximum number of potential dipoles available within the distance a (Sjödahl, 2006).

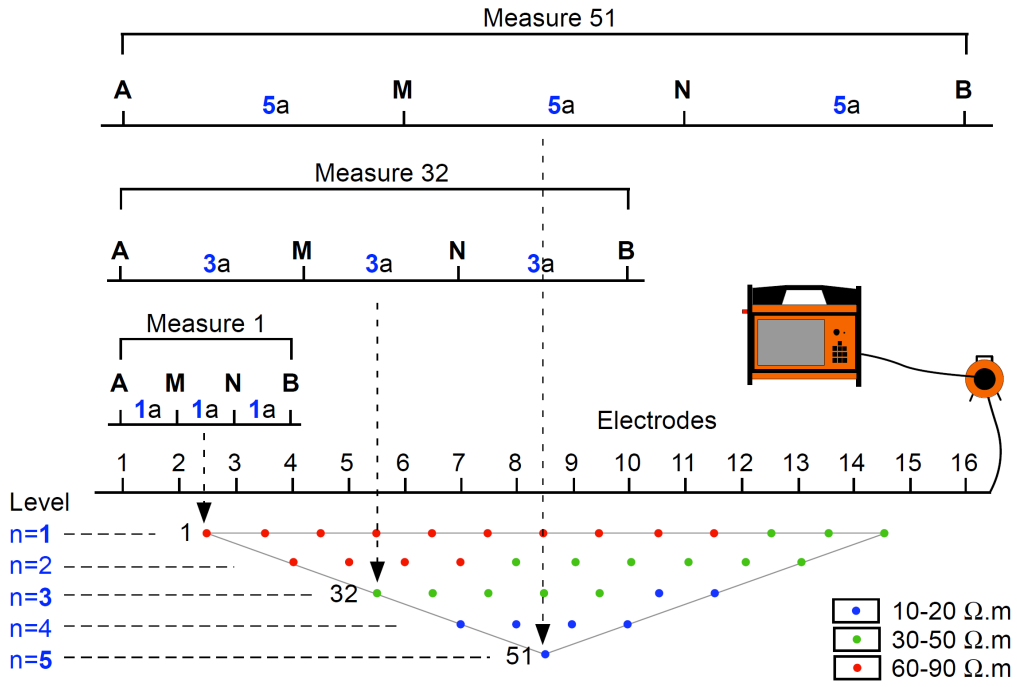

Figure 1-14: Pseudo-section of Wenner apparent resistivity data. The x-axis represents the location of the electrodes and the y-axis shows the pseudo-depth of each reading.

The application of ER can be either to investigate the embankment dam by conducting a single or couple of surveys for a limited timeframe or to monitor the structure continuously by installing permanent electrodes. The investigation of embankment dams has been more common in research studies because it is less time demanding than other geophysical techniques that might need human intervention even though the results obtained will less likely reflect the safety of the embankment dam (Sjödahl, 2006). The studies conducted previously on embankment dams for investigation relied more on detecting anomalous zones (Camarero et al., 2019; Himi et al., 2016; Martínez-Moreno et al., 2018; Tucker-Kulesza et al., 2019).

Earth dam Investigation Using ER

Camarero et al. (2019) conducted a geophysical investigation on the Ipeuna earth dam in Sau Paulo, Brazil to identify water seepage zones. Electrical resistivity technique was used because of its low cost and fast application in addition to its sensitivity to the compositional and moisture related variability. Three profiles along the crest with line 1 being on the downstream side were set. Wenner array configuration was used for data acquisition with an electrode spacing of 2 m and a survey length of 62 m.

Figure 1-15 shows thet ERT result conducted downstream of the Ipeuna dam. The black dashed line delineates the soil/rock interface which was obtained visually. However, the resistivity values of the upper layer of clay/silt (55%) and sand (45%) shows a relatively higher resistivity values (approximately 4,000 Ω.m) than the rock layer (approximately 500 Ω.m). It was hard to identify this interface due to the saturation of the rock layer. The ERT show low resistivity zones of about

60 Ω.m (LRZ1 and LRZ2) of different sizes which represent seepage zones. LRZ1 is located between 4 and 16m and at a depth between 2 and 5m which is at the contact zone between the embankment (soil) and the rock layer. This infiltration zone caused damages visually seen at the downstream.

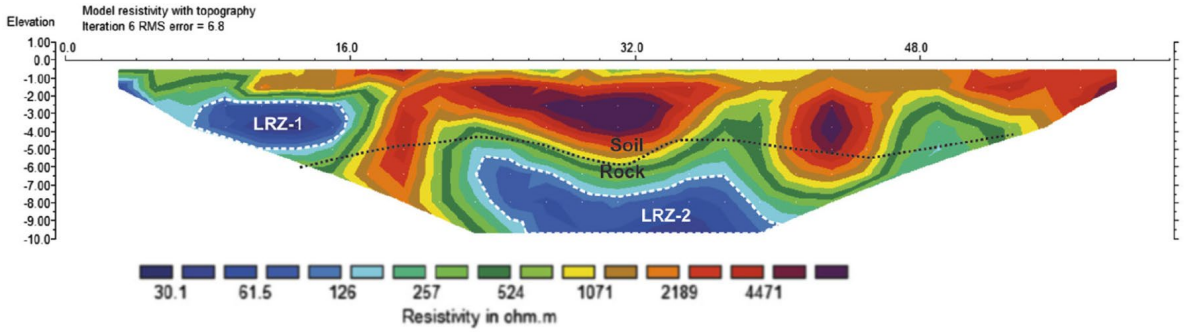

Figure 1-15: ERT conducted downstream identifying LRZ1 and LRZ2 and delineating the soil/rock interface by a dashed line (Camarero et al., 2019)**.**

The one-time application of the ER technique allowed the identification of seepage zones represented by lower resistivities in the ERT. The detection of these zones does not imply that internal erosion took place in any of them. It simply identifies areas of higher water content and heterogeneities.

Earth dam Monitoring Using ER in the Field

A blind test was conducted by Sjodahl et al. (2010) at the Rossvatn embankment dam: three anomalous zones (area of 0.16 m^2 each) were introduced in the dam using permeable material in the core of the structure. The locations of these zones were not revealed until the end of the analysis to avoid biased results (see Figure 1-16A for details). Repeated measurements on the crest were made at the same water level using 63 electrodes at a spacing of 0.67 m. Figure 1-16B shows the difference in inverted resistivity data between the empty dam and the dam being filled to a depth of 3 m. It shows a more important decrease of ER at a depth between 4 and 5 m (highlighted by a circle in Figure 1-16B). This result cannot be conclusive to determine if this zone is indeed a seepage zone. Therefore, another timelapse analysis was conducted between the initial empty tank and the tank empty after being filled to 3m. ERT is shown in Figure 1-16C. The same area detected in Figure 1-16B exhibited a decrease in ER whereas at this depth (3 to 7 m) showed an increase. Even though the electrical resistivity profiles facilitated the identification of the defect (zone B in Figure 1-16A) yet the 2 other zones of the same area were not detected. This could be due to the 3D effects that were not taken into consideration during the data analysis. However, the results are not satisfactory.

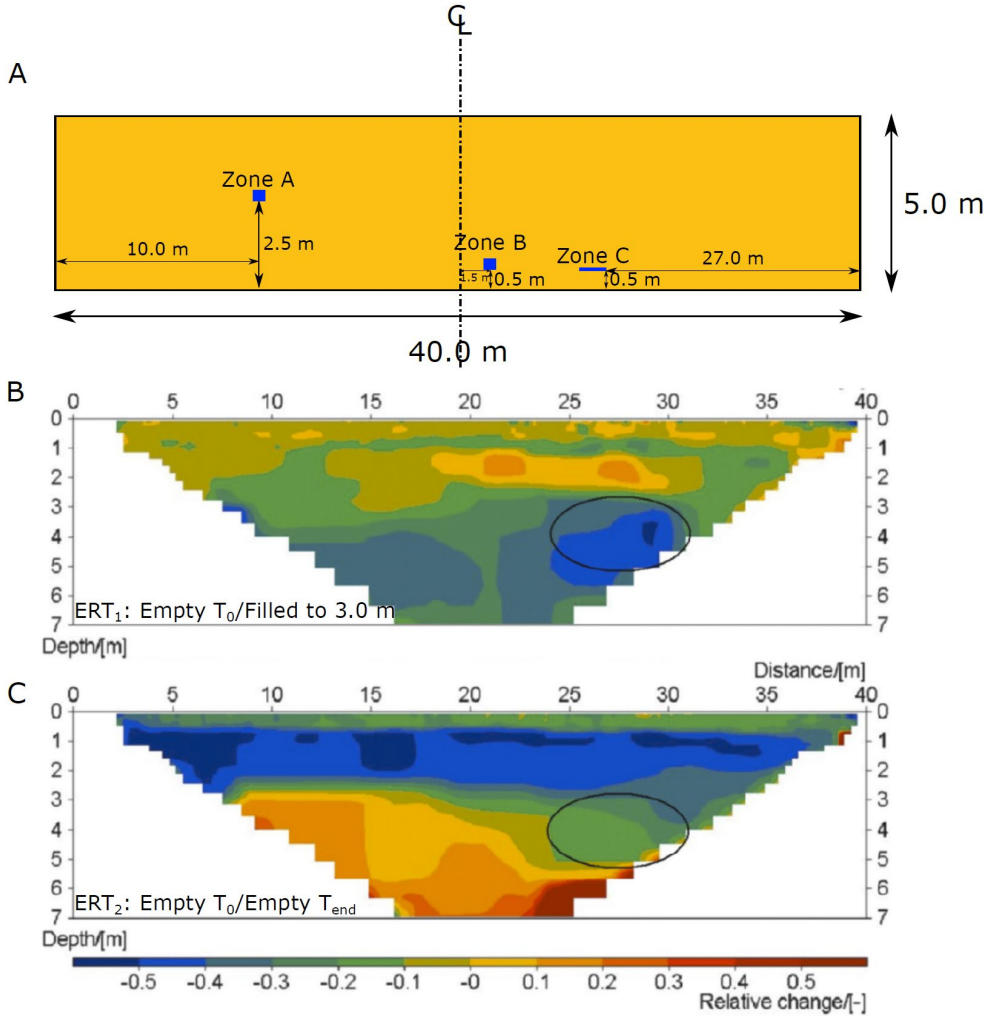

Figure 1-16: ER monitoring: A- showing the cross section of the crest with the 3 anomalous zones noted zones A, B and C; B- empty reservoir and the filling (3m depth) and C- empty reservoir at the beginning of the experiment and empty reservoir at the end of the experiment after being filled (Sjödahl et al., 2010)**.**

Another field experiment was conducted by Sjodahl et al. (2008) on the Hallby dam which is a coarse rockfill zoned embankment dam. It consists of a low permeable central core that is surrounded by filters of sand. Continuous data acquisition (over a 9-year period, from 01/1997 to 01/2006) was conducted on the crest of the dam. 43 electrodes were permanently installed on the crest at a spacing of 7 m and embedded at a depth of 1 m. In order to take into account the temperature variations throughout the seasons, temperature corrections were applied (normalized at 18°C). However, peaks are still detected during summer due to the snowmelt. Figure 1-17A shows the ER time series as a function of depth for location 1 at a distance of 61.25 m. It is noticed that the ER values decrease with depth and they range from 500 Ω.m to 20,000 Ω.m. The amplitude of the variation, similarly, decreases with depth. This is due to highly resistive shallow surface that undergoes freezing during winter. Even though this location represents a healthy location of the dam, however, at a depth of 19.9 m (blue curve), a decrease followed by an increase is observed

on the trend represented by a dashed line (Figure 1-17A). This behavior is not detected at the shallower data. For the second location at a distance of 43.75 m, the ER data repsented as a function of depth and time show an increase at a depth 43.75 m (highlighted in by a red line in Figure 1-17B). The dashed lines representing the trend show an increase of approximately 100 Ω.m. This increase could be due to the changes in the materials that originate from the excessive seepage induced by internal erosion mechanism. It is hard to associate the increase/decrease of the resistivity data with a soil mechanism (erosion or increase in water content) as highlighted in the trend shown in Figure 1-17 as dashed lines. According to the author, a one-time investigation would not have led to the conclusion of detecting this anomalous zone.

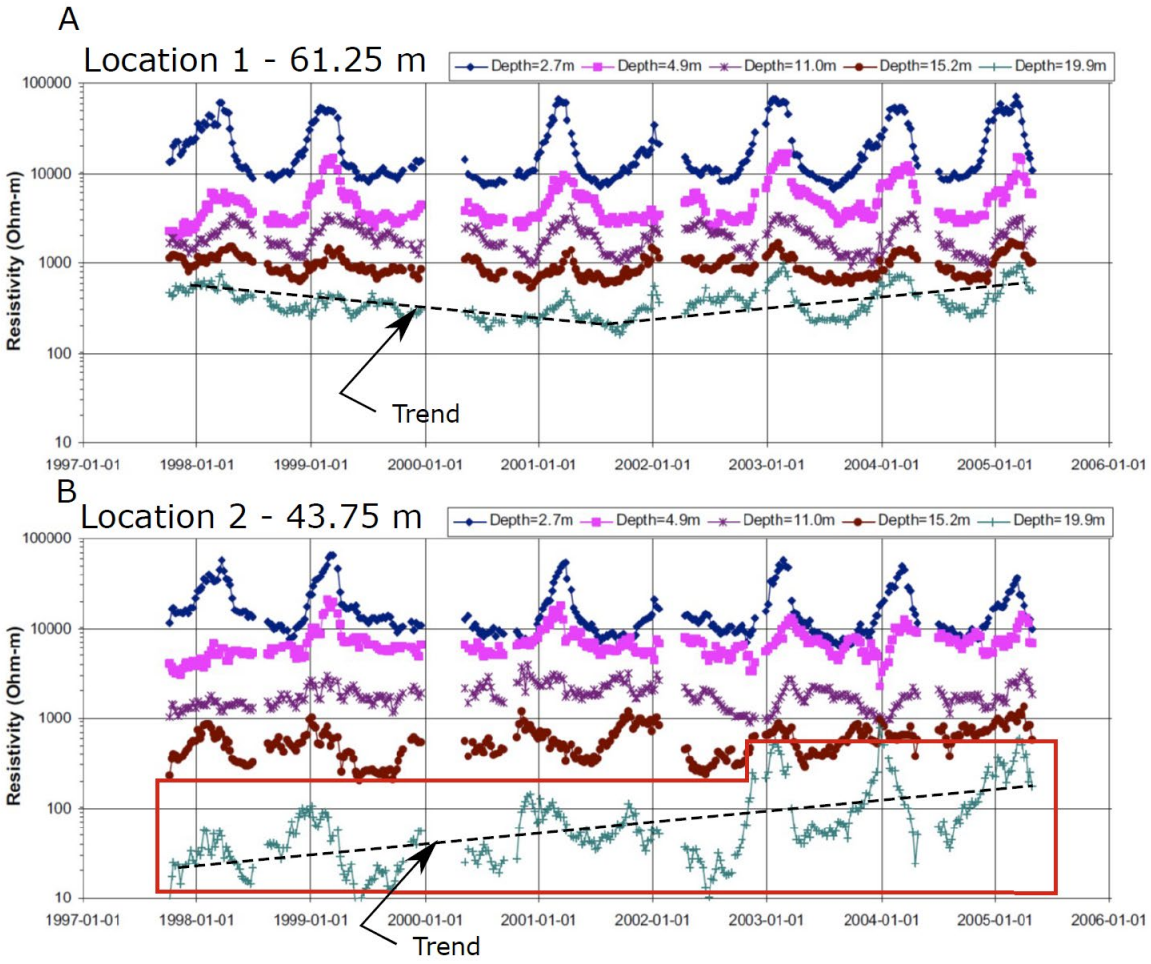

Figure 1-17: Electrical Resistivity results of the Hallby dam monitoring; A: electrical resistivity data at 61.25 m on the crest versus time at different depths and B: electrical resistivity data at 43.75 m on the crest versus time at different depths. Red box indicates the depth of the seepage (Figure 1-17B) (Sjödahl et al., 2008)**.**

The authors discussed the challenges faced during ER analysis. When detecting internal erosion in embankment dams, areas of high resistivities are of interest because of the fine particles being washed out thus leading to an increase in porosity. Contrarily, an increase in water content would

inflict a decrease in electrical resistivity but also, the lower amount of fines in the soil will also increase the electrical resistivity. Those two phenomena compensate each other therefore, it is hard to predict how the electrical resistivity of the material will be affected during internal erosion which would make this technique less reliable. With the varying factors that take place in the field, it is hard to assess and explain the origin of the changes observed in the electrical resistivity data. Therefore, it is important to conduct experimental testing in the laboratory under controlled environment that would help in better identifying the changes that might be encountered.

Internal Erosion Monitoring Using ER in the Laboratory

Shin et al. (2019) conducted a time-lapse resistivity experiment on a laboratory scale earthen dam that was built using fine grained sand of grain size < 0.06mm. An intentional zone of fine grain aggregates with sizes ranging between 5mm and 10mm were introduced in the body of the dam to induce internal erosion - Figure 1-18. 16 electrodes were placed at a spacing of 0.3 m on the crest of the dam. data acquisition required 20 min per survey for 76 data points collected. The data were inverted using spatial and temporal regularization parameters.

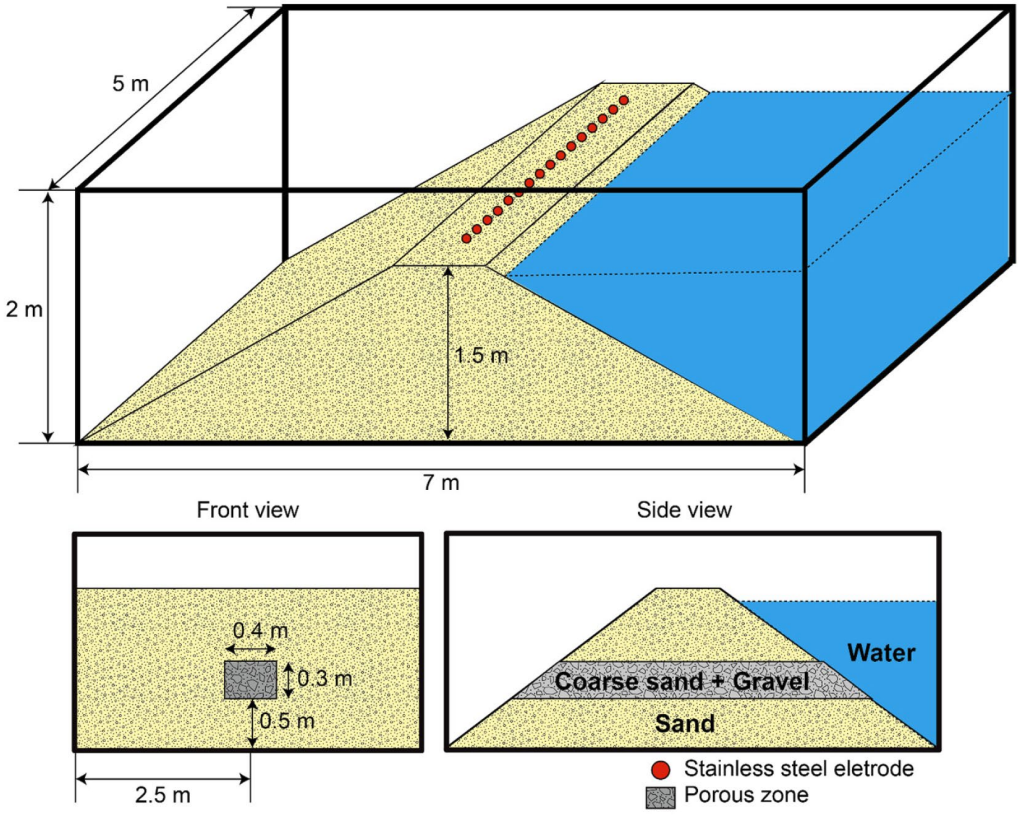

Figure 1-18: Experimental setup of the laboratory scale earthen dam and the anomalous one introduced to induce internal erosion (Shin et al., 2019)**.**

Time lapse analysis was conducted on the data retrieved and the results are shown in Figure 1-19. Two types of time lapse techniques were conducted for the inversion depending on the starting

model chosen. First, using the initial and second, using the preceding model. The increase in the water content was apparent from the decrease in electrical resistivity data but once the increase in water content took place, inverted results did not implicate any change even after the partial failure of the dam.

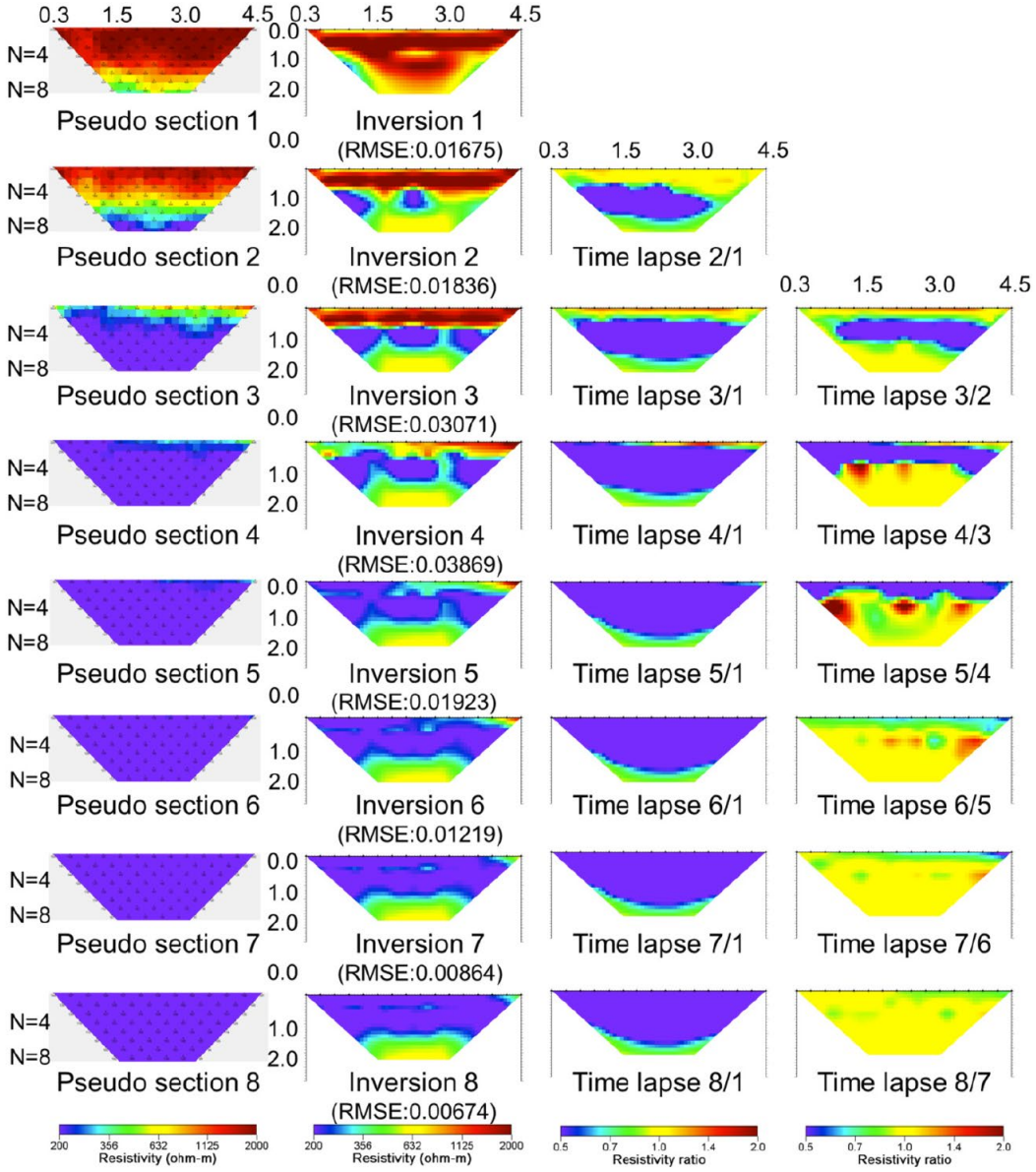

Figure 1-19: Results of the ER data retrieved at different time intervals; Column 1 shows the pseudo sections 1 to 8 from the start of the experiment to the failure respectively; column 2 shows the individual inversions; column 3 is the timelapse analysis using the 1st inversion as starting model and column 4 shows the timelapse analysis with the preceding model as starting model for inversion (Shin et al., 2019)**.**

Even though the electrical resistivity technique is being conducted on earth dams, the effect of internal erosion on the changes in resistivity properties is still not clear. The integration of multiple geophysical techniques has been recommended (Butler et al., 1989).

1.3.3.6 Seismic Monitoring of Earth dams

Seismic techniques rely on the wave propagation in the subsurface to identify the soil mechanical properties, shear strength, internal structure and voids (Park, 2017). The seismic surveys conducted could be either active when a source is used (i.e. a hammer) or passive when relying on the natural noise. There exist two types of seismic waves. The first one is the wave that travels through the body of the earth and is called body wave (P-wave and S-wave). The second type is the surface wave (Rayleigh waves and Love waves). They travel along the surface of the Earth and the nearby layers.

Active Seismic Investigation of Earth dams

The analysis following the active seismic technique leads to the acquisition of the compressional (P-wave) and shear (S-wave) seismic velocities. The use of P-wave (sensitive to the presence of water) and S-wave reflect the changes in shear strength (dynamic shear) and soil stiffness (Young's modulus) in the body of an earth dam (Karl et al., 2011) permitting the identification of different layers. Several active seismic studies have been conducted in the purpose of identifying zones prone to water seepage with a combination of other geophysical techniques such as GPR and ERT and geotechnical testing (Busato et al., 2016; Cardarelli et al., 2014; Karl et al., 2011).

Busato et al. (2016) conducted a combined geophysical study on a river embankment located in North-Eastern Italy. The results obtained from the 2 MASW profiles conducted on the crest show a phase velocity of approximately 120 to 260 m/s originating from the presence of clayey and silty sand (in agreement with the results obtained from the ERT survey and geotechnical investigation whereas the high phase velocities observed in the remediated portion originate from the heterogeneities due to the grout wall construction.

Bievre et al. (2017) conducted a seismic survey to characterize a small-scale earth dyke that included two visible seepage zones at the downstream. The profile was 46 m long and consisted of 24 4.5 Hz horizontal geophones located on the crest. Figure 1-20a shows the seismograms of the shot performed at the first geophone of the profile for the analysis of S and Love waves. Figure 1-20b shows the arrival times of the shots at the end of the profile and a center shot for the determination of the V_p profile. The phase velocity versus frequency was computed for the shot at 18 m and reveals high energy in the frequency band of 10 and 30 Hz as presented in Figure 1-20c. The inversion of the dispersion curve (Figure 1-20d) reveals a two-layered subsurface with a low velocity top layer of V_s = 150 m/s up to a depth of approximately 3 m overlying a high velocity layer with V_s ranging between 400 to 875 m/s. The data analyzed were used for the characterization of the subsurface and were not intended for monitoring purposes. Thus active seismic technique is

useful for imaging the subsurface and have a better understanding of the type of soils encountered in the body of the earth dam.

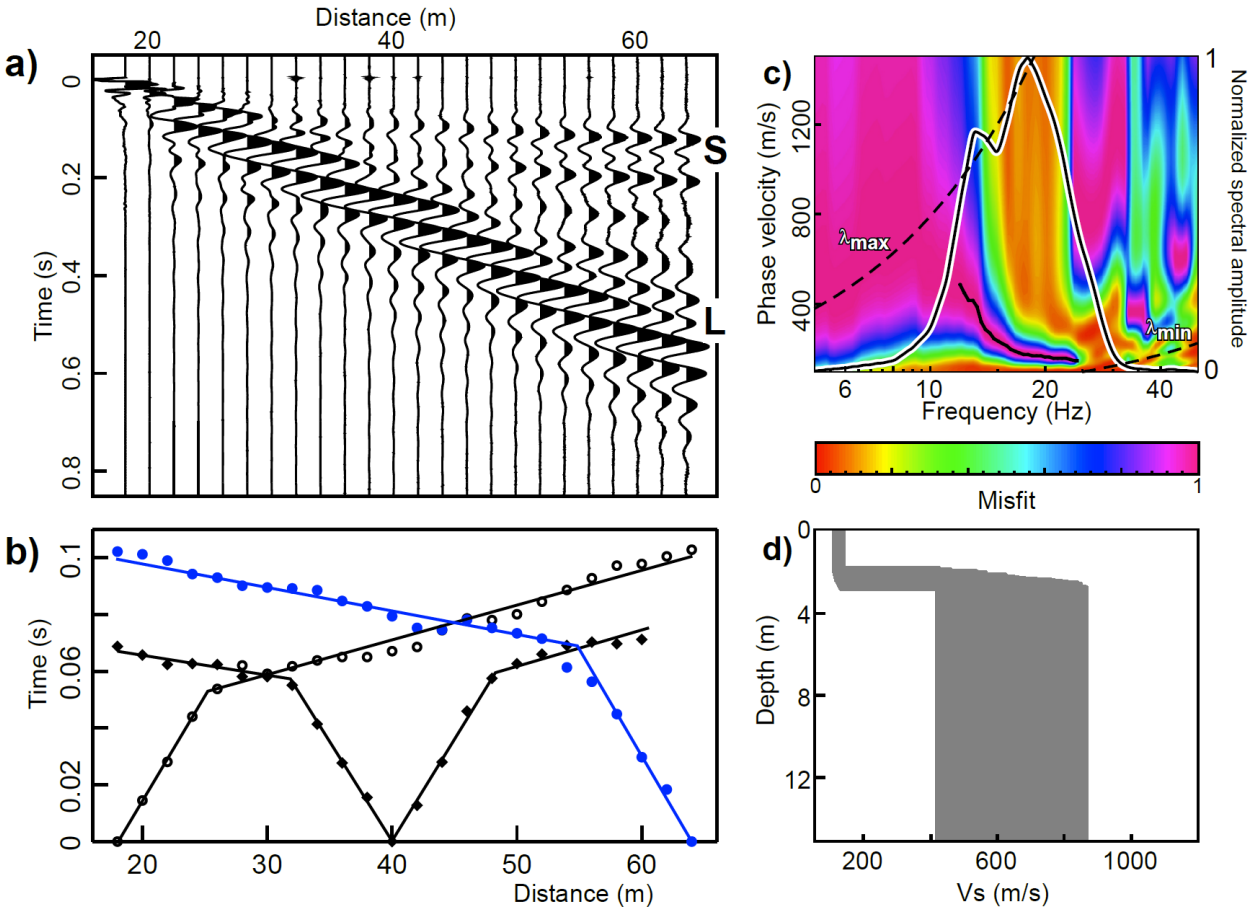

Figure 1-20: Seismic data analysis; (a) Seismograms of the shot at the first geophone of the profile for the analysis of S: S-waves and L: Love waves, (b) Travel-time curves corresponding to 2 shots performed at the end of the profile and one at the center for S-waves analysis, (c) phase velocity versus frequency of the Love waves corresponding to shot at 18 m along the profile and (d) Vs profile following the inversion of the dispersion curve in c) (Bièvre et al., 2017)**.**

The use of active seismic technique permits the identification of heterogeneity within the body of the earth dam but its resolution might not be high enough to capture and identify small anomalies within the embankment. Active seismic technique can be used as a baseline study for further geophysical investigations (Karl et al., 2011). The use of active seismic as a monitoring technique has not been fully explored in the literature because of its difficulty in the acquisition of data that requires an active source that is usually a hammer shot which cannot be done continuously during the operation of the dam. Periodical measurements could be conducted but provide poor temporal resolution.

Seismic Noise Monitoring

The use of elastic waves for numerous seismic tomographies have been widely used in the determination of spatial structure. However, in some geophysical fields, monitoring temporal changes in applications on volcanoes, faults, and dams among others is of great importance. Snieder et al. (2002) have introduced the Coda Wave Interferometry (CWI) to monitor temporal changes in a medium by using its scattering properties as an interferometer. Sens-Schonfelder et al. (2006) used passive imaging in order to get the CWI on a study conducted on Mt. Merapi which is one of the most active volcanoes. The hydrological conditions during the time of the study highlighted the measured changes of the seismic velocities dV/V obtained from the analysis. The seismic monitoring has also been successful in many applications such as groundwater exploration (Clements and Denolle, 2018; Larose et al., 2015; Lecocq et al., 2017; Mordret et al., 2020; Rittgers et al., 2015; Voisin et al., 2016) and in embankment dams (de Wit and Olivier, 2018; Fisher et al., 2016, 2017; Hickey et al., 2009; Parekh, 2016; Planès et al., 2016; Rinehart et al., 2012; Rittgers et al., 2015).

The study conducted by Planes et al. (2016) incorporated noise monitoring on a laboratory scale and an experimental earth dam in the purpose of identifying and monitoring the evolution of internal erosion. The laboratory scale embankment dam was constructed in Colorado, USA, for modeling internal erosion mechanism - Figure 1-21. A metal rod of 1.3 cm diameter was inserted in the structure at a depth of 25 cm to create a pipe for water seepage hence starting the experiment at the progression phase of internal erosion. The materials used for the embankment consisted of low-plasticity silty sand including 15% clay, 20% silt and 64% sand compacted at 98% of maximum dry density for the bottom 30 cm and 87% for the upper part. The embankment dam was monitored using 10 vertical geophones located on the crest at a spacing of 61 cm. The sampling frequency used during the data acquisition was of 2 kHz. The flow downstream due to the piping was recorded. The experiment started (T = 0 h) when the metal rod was removed from the dam and lasted 6.5 h when the pipe reached the crest.

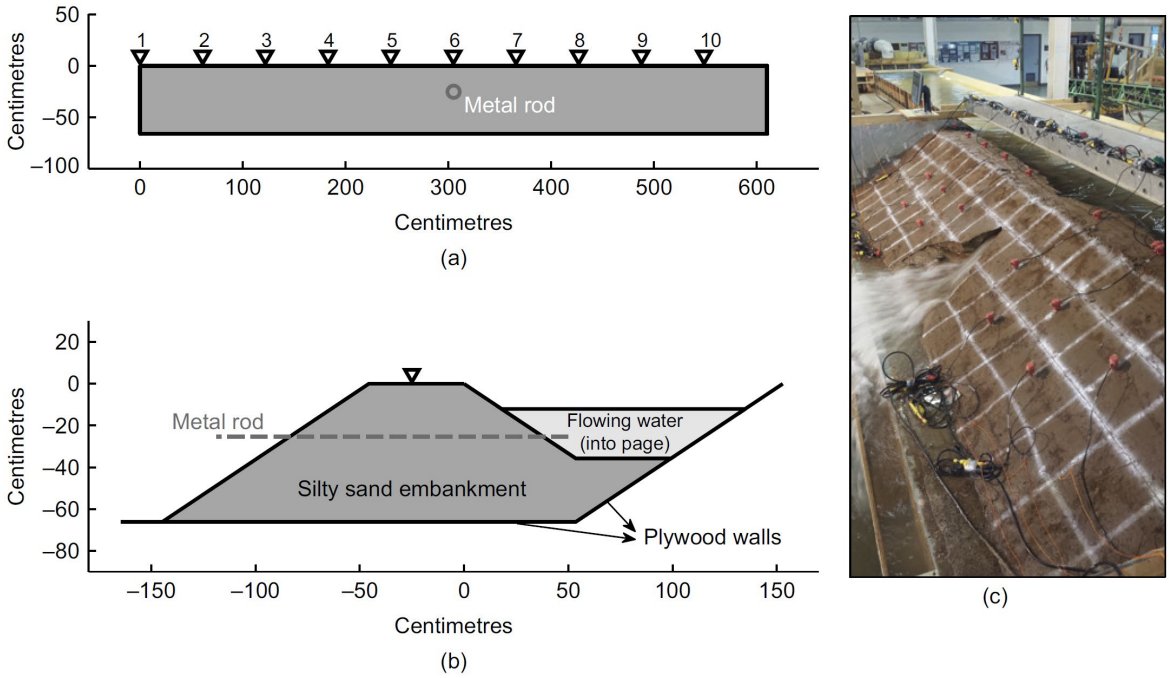

Figure 1-21: (a) The front view drawing of the laboratory scale earth dam of approximately 600 cm width and roughly 70 cm height. The metal rod is located in the center below geophone 6; (b) cross section view of the earth dam and (c) photograph of the piping following 5 h of water seepage (Planès et al., 2016)**.**

The data acquired were filtered around a central frequency of 50 Hz and cross correlations were computed between pairs of sensors located at a distance of 1.2 m for the 4 h duration of the experiment. Due to the degradation of the dam, it was hard to obtain stable results in the interferometry design. Results are shown in Figure 1-22. The relative changes in the velocity (dV/V) represented show the same trend of velocity decrease starting 2 h and not identifying the first 2 h of water seepage. The decrease is more pronounced (20%) for the sensors pairs: 4-6, 5-7 and 6-8 but is presented as a jump then remains constant at -20% whereas for the other sensors pairs, the decrease is continuous. The decrease in dV/V is mainly due to the large modifications taking place around the pipe that originates from stress redistribution.

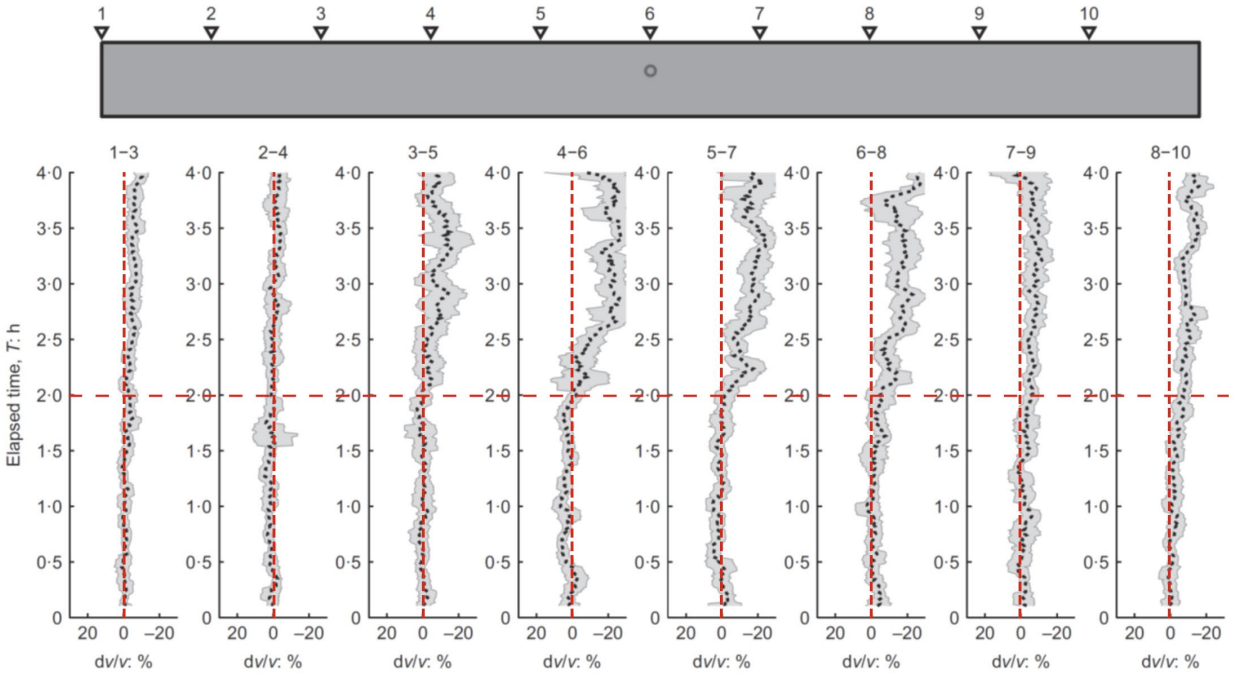

Figure 1-22: Velocity changes obtained following the cross correlation conducted on a 1.2 m spaced pairs of sensors (Planès et al., 2016)**.**

Another test was conducted by Planes et al. (2016) on the IJkdijk experimental levee to reproduce the results obtained in the laboratory at a larger scale (details in Figure 1-23). No metal rod was inserted in the dam. The foundation consisted of a poorly graded sand placed on top of a geomembrane. The embankment consisted of clay compacted at 90% maximum dry density. The upstream was filled with water gradually to better assess real cases. Water travels in the underlying sand layer and propagates backward (backward erosion) to reach the upstream. In order to prevent this from happening and avoid complete failure, a geotextile was placed at 4 m from the toe side. At around 20 h, sand boils started appearing at the downstream because of the concentrated seepage. Following the sand boils, a softening behavior was observed at 90 h (Figure 1-23b). Pore-water pressure was monitored throughout the experiment by installing 4 piezometers at the downstream (Figure 1-23c – circles). The 24 geophones were installed along 3 lines at the downstream acquiring data at a sampling frequency of 1 kHz. The experiment lasted 160 h and unlike the laboratory testing, the dam did not fail.

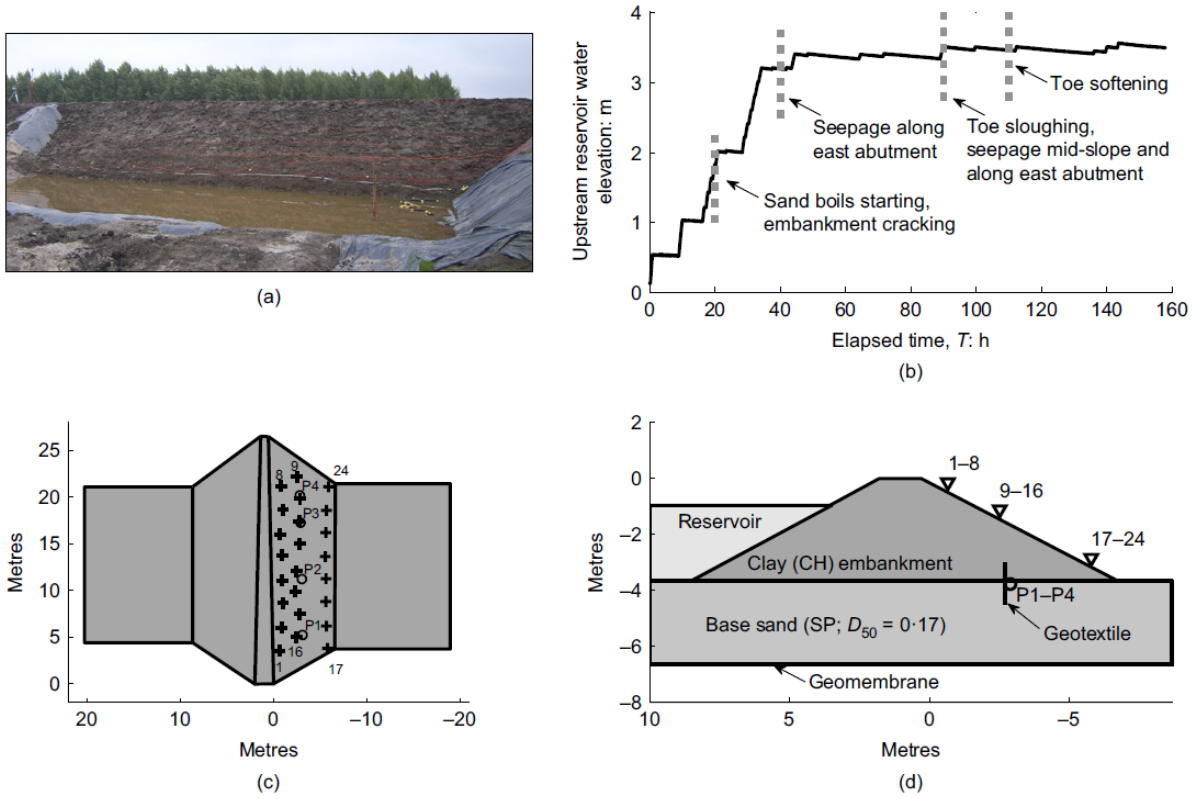

Figure 1-23: (a) representing the downstream and the leaked water, (b) the different upstream reservoir water head with time and the corresponding stages of the experiment, (c) and (d) the top and cross section view respectively of the dam (Planès et al., 2016).

The computed average surface wave velocity following the localization of the source was computed and is shown in Figure 1-24b. The results start at T = 30 h of the experiment because the first portion of the data is not coherent. The leakage at the abutment A and the softening at C (Figure 1-24a) are followed by a decrease in the average velocity (Figure 1-24b). Fluctuations at the T = 90 h are observed probably due to the water elevation upstream. The computations of dV/V for different sensor pairs with the plot of piezometer heads are shown in Figure 1-24c to f. The dV/V shows a decrease with the increase of pressure head. Additional drops are observed (Figure 1-24d and highlighted in red rectangles) between 110 h and 135 h that were not coincident with changes in the pressure head. They could be associated with changes from the sandboils and/or the softening of the clay at the toe.

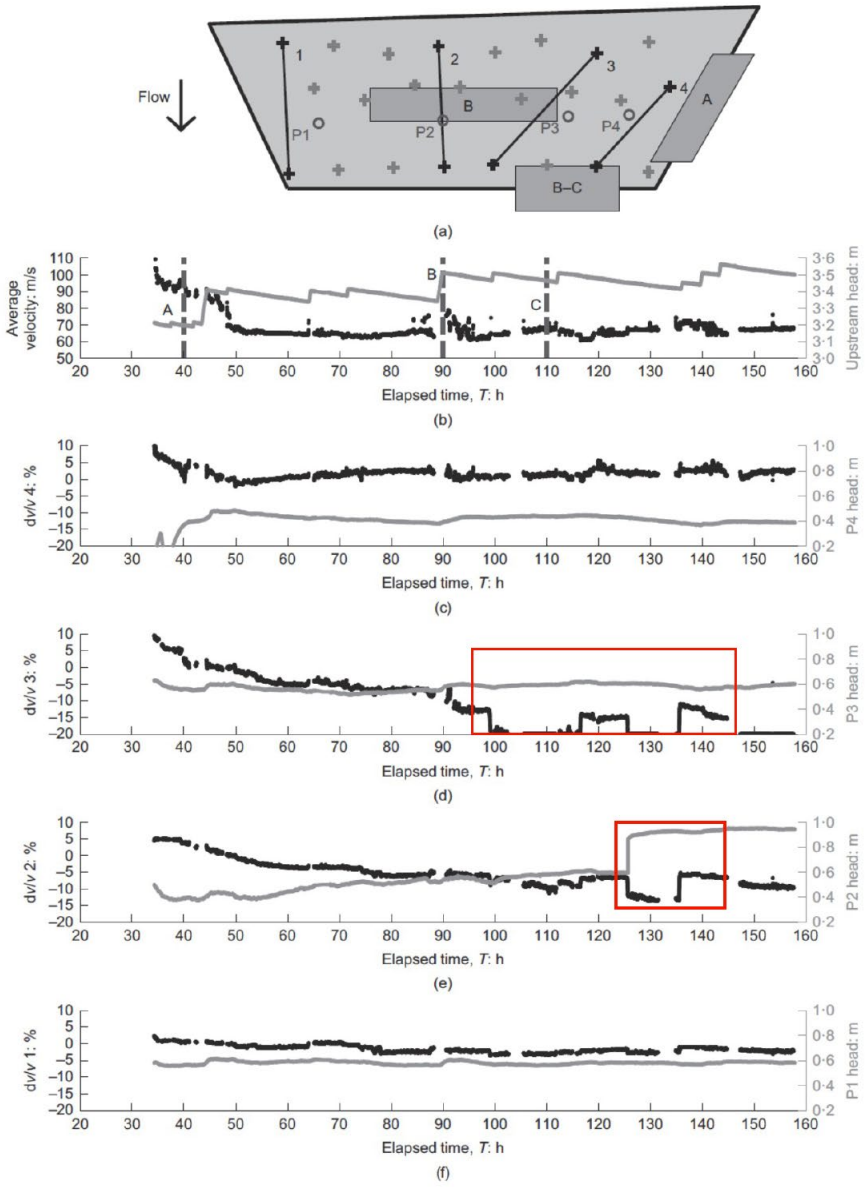

Figure 1-24: (a) Representation of the sensor pairs selected for the analysis of dV/V with the visual leakage locations highlighted by grey rectangles: B and A at the abutment, whereas B-C represents the softening areas; (b) shows the water elevation in the reservoir and the average surface wave velocity, (c) to (f) show dV/V analysis with the sensor pairs selected and shown in part (a) (Planès et al., 2016)

Both of the experiments conducted by Planes et al. (2016) did not show the evolution of internal erosion (starting at the initiation phase until reaching failure). The changes of the dV/V shown highlight the presence of water and water seepage but do not identify the evolution of internal erosion (migration of soil particles) within the body of the structure. Moreover, dV/V does not always reflect the changes observed in the piezometers readings. Thus monitoring earth dams using dV/V could sometimes be misleading.

Moreover, new emerging equipment such as the Distributed Acoustic Sensing (DAS) are being implemented during the construction of new earth dams. A study by Johannsen et al. (2021) reports the use of both temperature and seismic readings to identify leakages in a dam in Sweden. Seismic monitoring shows changes in dV/V yet they were not in line with precipitation and temperature readings hence the need for further analyses techniques.

Passive Seismic Listening

The seismic data acquired is not solely used for seismic noise monitoring but also to assist in listening to what is happening inside the structure. This technique serves to monitor Acoustic Emissions (AE) originating from the flow of water in the porous media, cracking events taking place within the soil structure, rearrangement of soil particles, collapsing of soils in the seepage zone and identify different seepage velocities (Hung et al., 2009; Smith and Dixon, 2019).

Bievre et al. (2017) conducted a combined geotechnical and geophysical experiment on a small earth embankment dam with known defects due to leakages observed downstream caused by internal erosion. Active and passive seismic techniques were conducted with the deployment of 24 vertical geophones at a spacing of 2 m located at the crest. The testing was conducted twice: the first time when the leakage zone existed (before remediation) and the second time following remediation works. The data acquired during active testing was used for the P-wave and S-wave analysis. No anomalies were detected. ERT profiles were conducted one at the crest whereas the second on the downstream side. Data inverted did not reveal the presence of the leakage zones.

Passive seismic data acquired during both times at a sampling frequency of 250 Hz were able to detect higher amplitudes in the seismogram of the geophones at the location of one seepage zone prior to remediation. However, following the remediation works, no higher amplitude was detected in the data. In order to locate the seepage zone, a modified beam forming algorithm on the passive seismic data was able to locate the depth of the seepage zone. Figure 1-25a shows the location of the seepage zone prior to any remediation work and Figure 1-25b shows the analysis after the remediation work where the located seepage zone is outside the seismic survey which is probably due to the low seepage flow after the executed work.

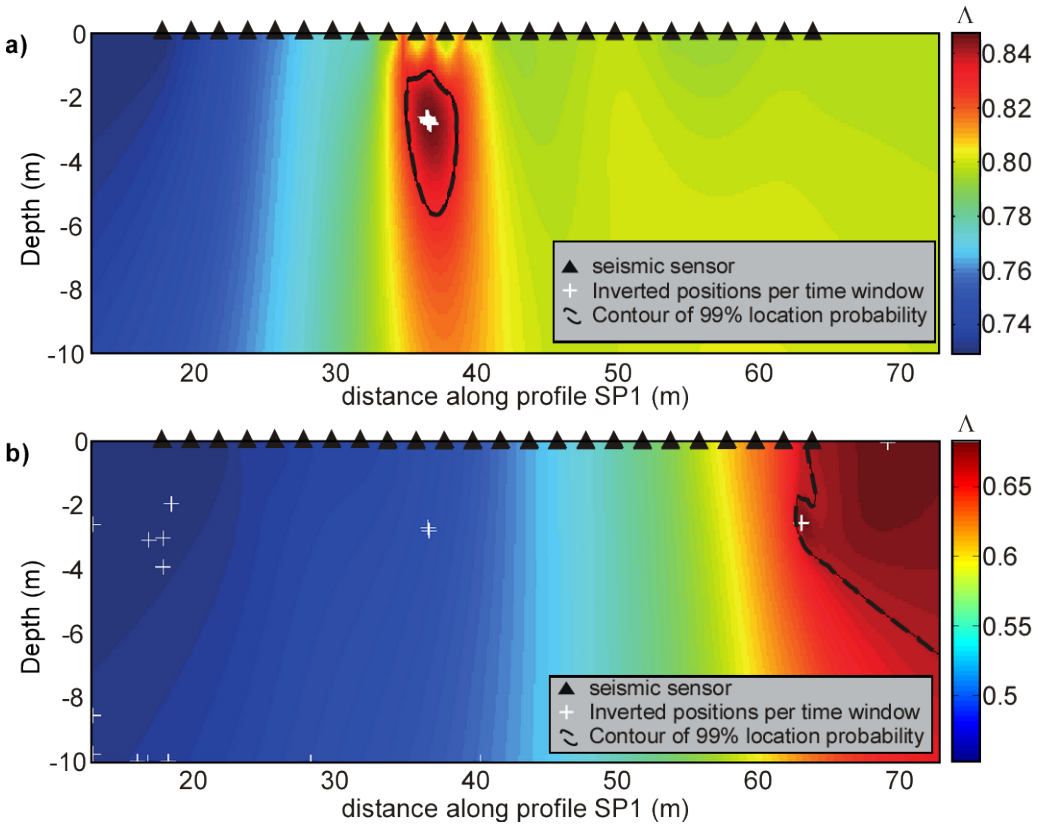

Figure 1-25: Locating the seismic noise source; a) shows the Probability Density Function (PDF) of the seismic source location before any work has been implemented on the site and c) PDF after finishing the remediation works (Bièvre et al., 2017)**.**

Hickey et al. (2009) conducted an experiment in Stillwater, OK at the USDA-ARS Hydraulic Research Unit (HERU) to study passive and ambient seismic techniques on internal erosion mechanism. A 12 m long and 1.25 m high earthen embankment was built with a 38 mm diameter steel pipe mounted in the structure to model water seepage and internal erosion process. Refraction tomography was conducted when the reservoir was empty, after filling, and during seepage. Results showed a drop in the compressional wave velocity tomogram during internal erosion. Passive seismic monitoring was conducted considering the flow of water as a source of seismic energy that would be higher than the background noise; consequently, higher energy was detected during the water seepage and internal erosion that was not present when the earthen dam was empty as depicted in Figure 1-26. The response of the geophones installed a bit further from the pipe also showed this energy but at lower amplitude; thus, indicating that the source of this seismic energy is the flow of water and probably the internal erosion mechanism.

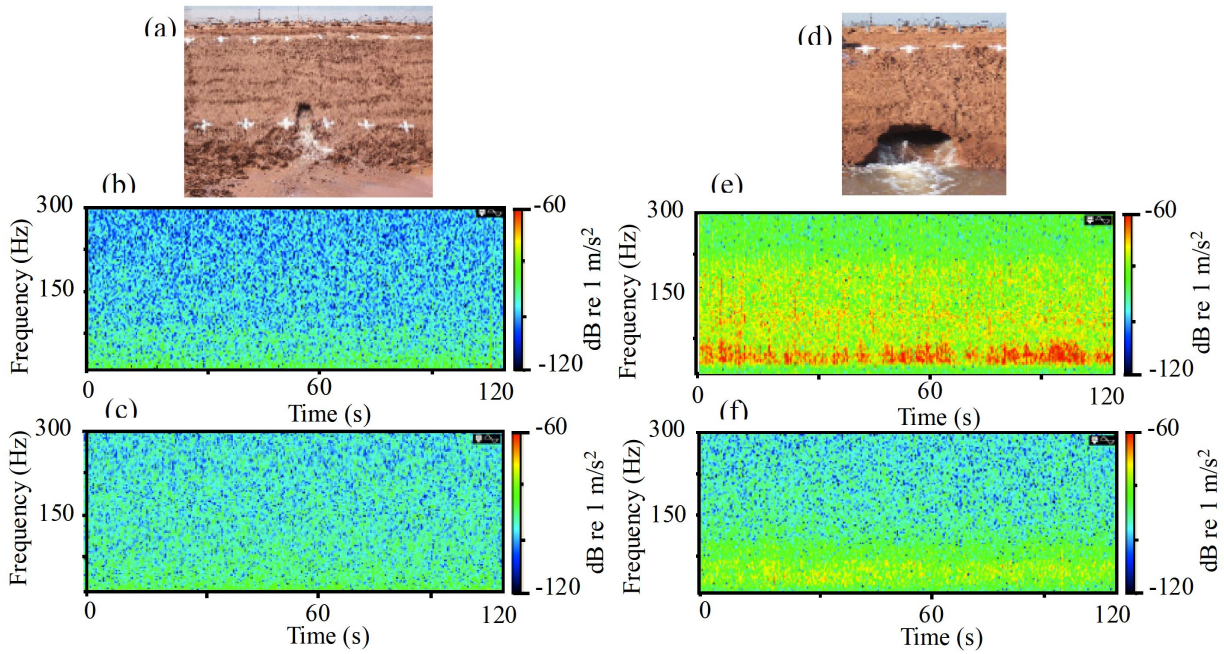

Figure 1-26: Results of the passive seismic monitoring: a) shows the early stage of internal erosion when the pipe diameter was still small, b) the spectrogram from the data collected from the geophone located at a distance of 1m from the erosion pipe at the early stage, c) the spectrogram obtained from the analysis of the data collected from the geophone located at a distance of 3.7m from the pipe, d) view of the enlarged pipe leading to further erosion – late stage, e) the spectrogram showing high activity from the data collected from the geophone located at 1m from the erosion pipe at the late stage and e) the spectrogram of the data collected from the geophone located at a distance of 3.7m from the erosion pipe following at the late stage (Hickey et al., 2009)**.**

Parekh (2016) ran an experiment on the IJkdijk levee embankment in the Netherlands (shown in Figure 1-27). The Upstream Water Level (UWL), pore water pressure and the quantity of sand removed were monitored throughout the experiment. The objective of this study was to show the changes in acoustic emissions (i.e. small vibrations) caused by the concentrated seepage and the internal erosion mechanism. The experimental dam was not brought to failure, and the work consisted on monitoring the AE changes with the increase in head upstream and the quantity of sand extracted downstream. The 24 vertical geophones were deployed on the downstream with a sampling frequency of 1 kHz. The frequency content of the signals showed higher energy in the frequency range lower than 100 Hz. The test lasted approximately 7 days with data acquisition starting 18 h before increasing the head at the upstream to obtain baseline readings (denoted with a negative sign for the time in Figure 1-28). After 18 h, sand boils and water started appearing at the center of the embankment (downstream side) with sand production appearing at 22 h of the experiment.

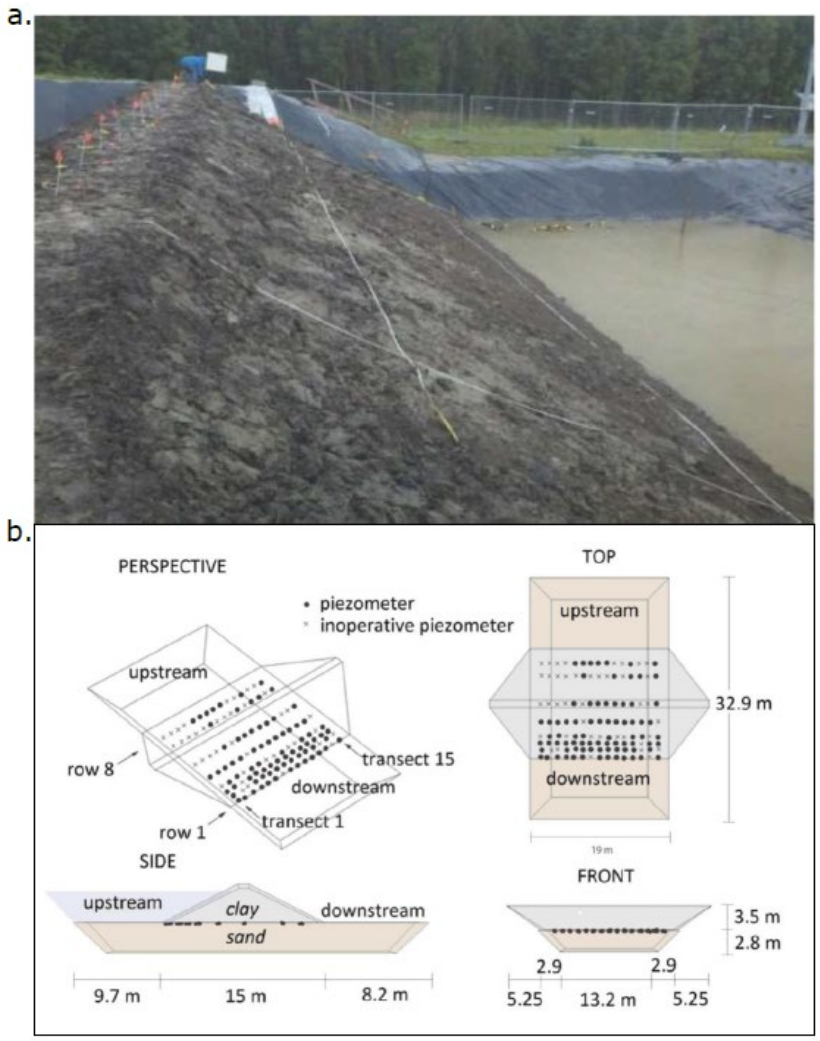

Figure 1-27: IJkdijk dam; a. Upstream view of the embankment dam following construction and b. the dimensions of the embankment dam (Parekh, 2016)**.**

The normalized Root Mean Square (RMS) was computed from the data gathered from the geophones placed on the downstream which showed an increase whenever the seepage and internal erosion started especially at geophone 21 located in the center of the toe. The counts of normalized amplitude exceeding a threshold set to 10 are in line with the increase in UWL (Upstream Water Level) up until 35 h indicating the sensitivity of the method to the increase in the water level thus the start of water seepage Figure 1-28; Cracks and embankment deformations were detected between 20 and 64 hours but were not really detected since the AE decreased from 50 until 75 h. Between 90 and 120 h, increase in sand boils and production was detected which highlighted an increase in the AE counts. The behavior of the AE shows episodes of increase in activity then a decrease which depicts that the system goes into a stable mode where it calms down. The response of the AE is not dependent on the increase in the head suggesting that the process is highly non-linear and is triggered by a threshold head of water when the response is seen (35 h - Figure 1-27)

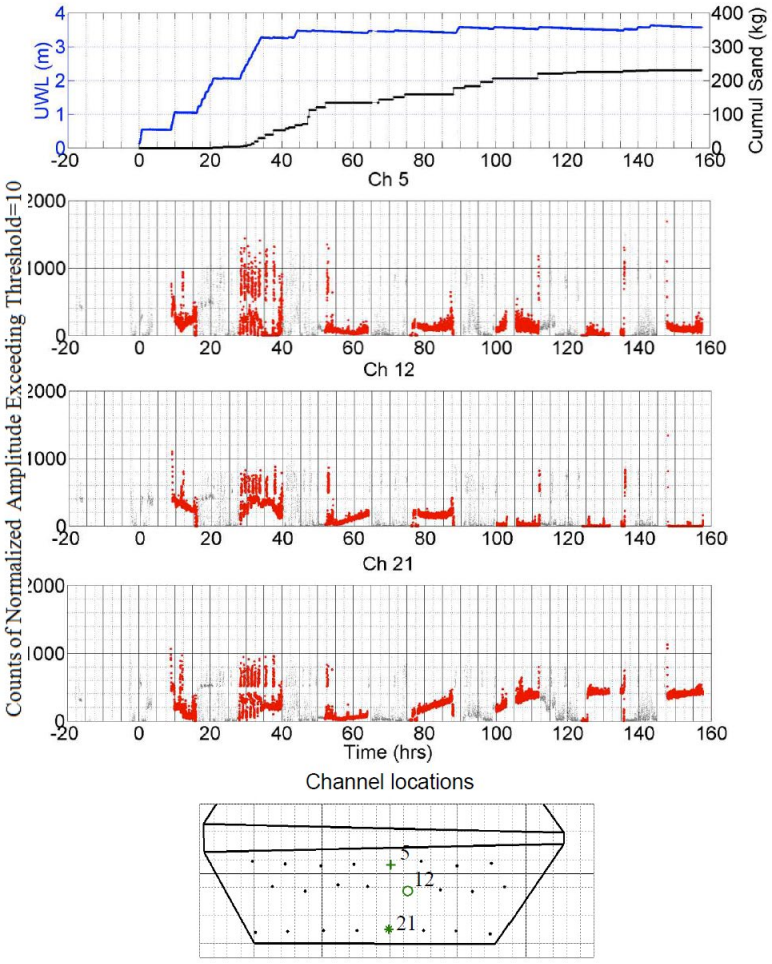

Figure 1-28: Acoustic Emission counts of peaks that exceed a threshold set to 10 detected on three channels at the downstream. Red dots represent the measurements during night time (Parekh, 2016)**.**

1.4 Summary

Extensive studies have been dedicated to the use of geophysical techniques in order to detect anomalous zones prone to internal erosion in earth dams. These studies have shown the ability to detect areas with higher water content and heterogeneities. Geophysical monitoring (mainly electrical resistivity and seismic techniques) has been applied in both laboratory and field experiments in order to show their effectiveness in monitoring seepage zones.

The use of ERT for timelapse analysis for the detection and the evolution of water content in the seepage zones shows promising results. However, for the monitoring of internal erosion mechanisms, it did not show any evolution in the data once the zone is fully saturated due to the multiple factors that might affect the results (higher water content, higher porosity, lower density, changes in temperature among others). In addition, the resolution of the data with time causes a

challenge since for one survey, it is acquiring data representing multiple changes in the medium that would not be helpful in pinpointing the evolution of internal erosion.

Different seismic techniques have been explored in the literature for investigation and monitoring purposes. The use of active methods has been solely dedicated to the imaging of earth dams for identifications of zones that might be prone to seepage and internal erosion. However, this method was not used for continuous monitoring due to the fact that an active source has to be emitted for the data acquisition and it usually requires human interaction. Passive techniques (i.e. noise monitoring and passive seismic listening) have shown promising results in monitoring internal erosion because of the high temporal resolution with data acquisition (sampling frequency) and its sensitivity to changes occurring in the seepage zone (rearrangement of soil particles, changes in flow, crack among others). Nevertheless, the experiments that were conducted did not address the entire process of internal erosion that starts with the seepage of water, particle movement (initiation) the formation of the pipe and finally the breach.

The existence of continuous slow seepage in the body of the dam makes it hard to identify the changes happening in the structure of the porous medium hence the effect of these changes on the flow rate of the seepage that might cause the initiation of internal erosion. In the present study we focus on studying the entire evolution of internal erosion through the use of electrical resistivity and seismic techniques to differentiate between two major components: first the seepage of water in the earth dam and, second the evolution of the porous medium to initiate internal erosion.

CHAPTER 2
WATER SEEPAGE IN POROUS MEDIA: EXPERIMENTAL FIELD TESTING

Earth dams are constructed using low permeability materials. This being said, the flow of water (seepage) still exists but at extremely low rates. At some point, and with the presence of anomalies, heterogeneities and cracks due to the continuous cycles of wetting and drying in the body of the earth dam (or foundation), concentrated seepage might take place and might evolve to internal erosion. The detection of water seepage using geophysical techniques has been extensively studied (see Chapter 1 for details). Following the studies conducted previously, multiple leakages appeared during the experimental work making it challenging to really understand the effect of water seepage on the seismic and the electrical resistivity responses. For this purpose, a study was conducted on an experimental dam constructed in Rouen, France. The dam consists of a fine sand body covered with a concrete layer and a geomembrane to ensure the impermeability of the upstream. Three permeable channels are embedded in the body of the dam to allow water seepage (solely in the channels) at different flow rates. Only one channel will be used in the study. Both techniques used in the laboratory (electrical resistivity and seismic) were adopted in this experiment in the objectives of detecting water flow and quantifying it. In the existing setup, internal erosion is not allowed to take place and that is due to the presence of a mesh downstream.

2.1 Experimental setup

An experimental dam was constructed at CEREMA, Rouen for the purpose of detecting water flow in the body of earth dams. The location of the dam is shown in Figure 2-1.

Figure 2-1: Location of the experimental dam in Cerema near Rouen, France.

The dam measures 22 m in length, 14 m in width and 3 m in height. The height of the reservoir is of 2 m (details shown in Figure 2-2). The dam consists of 10 layers of compacted sand (properties summarized in Table 2-1). The rate of compaction ranged between 98.9% and 102.7% at a water content ranging between 6.1% and 8.0%. During the compaction of the first layer, and at a height of 0.18 cm, a geotextile of 0.089 m/s permeability was laid on the surface that had a slope of 3% to wrap the gravels of sizes ranging between 4 and 6 mm inside the F2 channel (highlighted in red in Figure 2-2B). At the downstream side, a bentonite layer was laid around the channel and at a distance of 1 m from the downstream, a PVC pipe encased the channel. A filter was introduced at the downstream to ensure that no collapse takes places as detailed in Figure 2-3. F2 had a higher permeability than the surrounding sand to ensure that the water infiltrates in it. The maximum flow rate that can be achieved in F2 is theoretically in the order of 9L/min equivalent to a Reynold's number of 0.75 which is considered to be a laminar flow.

At the downstream, a double tipping bucket flowmeter was installed. Water collected from the channel fills one bucket of 1 L capacity and flips to fill the second bucket. Every flip (representing 1 L) was recorded and the data were acquired every 5 minutes (number of flipping bucket in 5 minutes). A fiber optic cable was installed in the dam at different depths (steps of 0.3 m) in order to monitor the changes in the temperature. The experiment started by a baseline when the reservoir was empty. The height of water was increased gradually to reach the maximum capacity of the reservoir which is at 2.0 m.

Table 2-1 Geotechnical properties of the sand

Optimum Moisture Content (OMC)	11%
Dry Unit Weight (γ_d)	18.5 kN/m^3
Angle of friction (Ø´)	36.9°
Cohesion	2 kPa
Permeability (k)	3×10^{-7} m/s

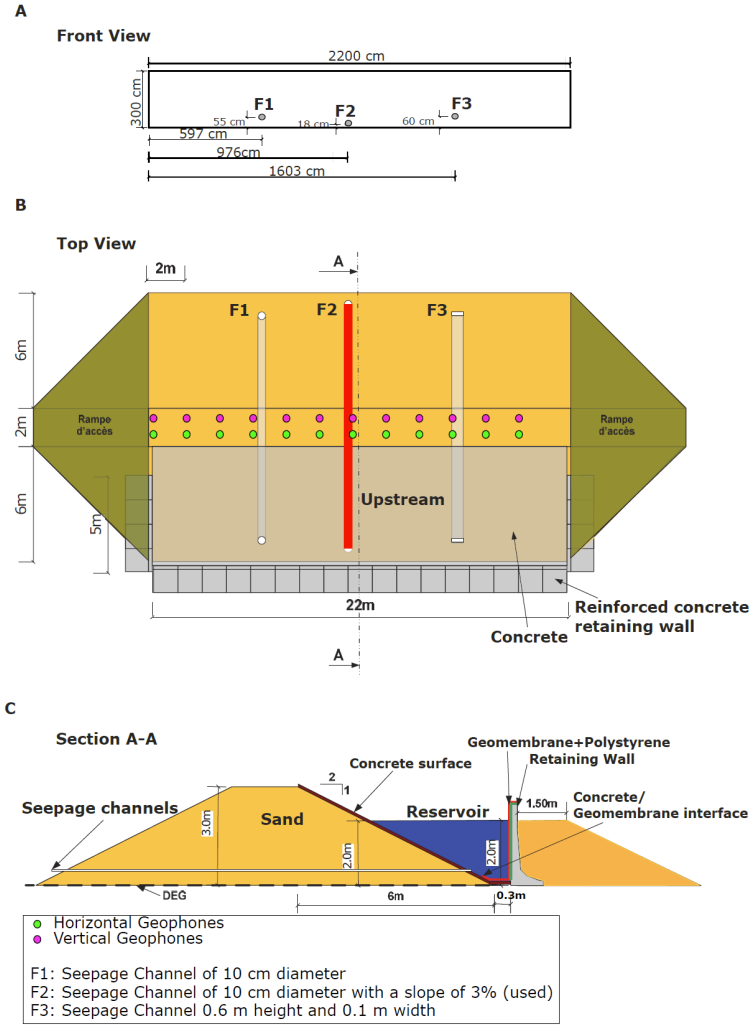

Figure 2-2: Dimensions of the Experimental Dam. A- Front view showing the height of the 3 seepage channels, B- Top view indicating the location of the vertical (pink) and horizontal (green) geophones on the crest and C- Section A-A showing the reservoir and its details.

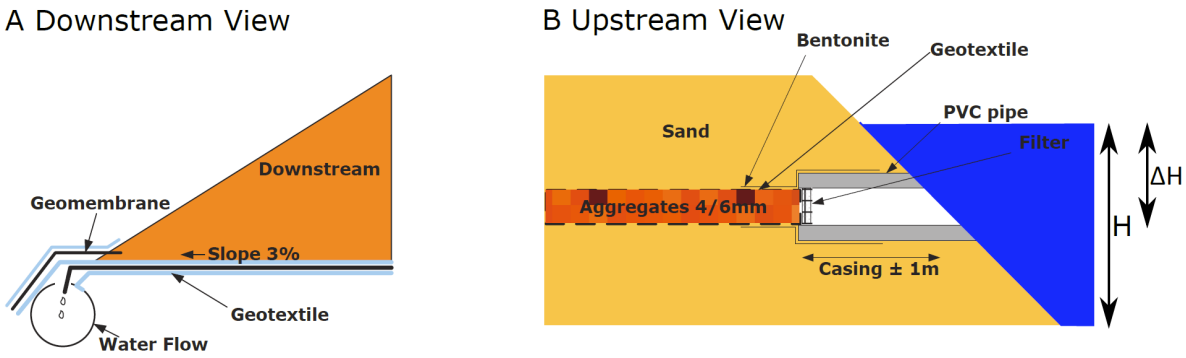

Figure 2-3: Details of F2 seepage channel from A the downstream side showing the geotextile and the geomembrane and B the upstream side showing the PVC pipe, bentonite, filter and the corresponding ΔH.

2.1.1 Electrical Resistivity Tomography

The electrical resistivity monitoring consisted on spreading 32 electrodes at a spacing of 0.50 m on the crest of the experimental dam leading to a total survey length of 16 m. The electrodes were connected to an ABEM SAS1000 resistivimeter. The classical Wenner array was used for data acquisition consisting of 155 measurements. The data was inverted with the BERT package after applying the corrected geometric factor obtained following a forward inversion using F3DM in 3D. The acquired data were inverted in 2D with the use of the apparent resistivities computed with the 3D geometric factors. Following the acquisition of the temperatures throughout the experiment, electrical resistivity was corrected to take into account the effect of temperature by applying the equation detailed in Hayley et al. (2007 and 2010) below :

$$\rho_{Tref} = \rho_T \times \left(1 + 0.0202 \times \left(T - T_{ref}\right)\right) \quad (6)$$

where ρ_{Tref} is the resistivity at the reference temperature (Ω.m), T_{ref} represents the reference temperature (°C) which is of 25°C and ρ_T is the resistivity (Ω.m) at temperature T. Corrected electrical resistivity data were then inverted in 2D using a predefined mesh representing the true geometry of the experimental dam with the inclusion of an insulating boundary which represents the geomembrane at a depth of 3 m.

The timelapse method was adopted during the inversion of the data using the baseline model (initial) as a starting model for further inversions, and thus obtaining the ratio of changes between each timestep and the baseline profile.

2.1.2 Seismic Measurements

A profile consisting of 12 vertical and 12 horizontal geophones with a nominal frequency of 4.5 Hz and a spacing of 1.5 m was laid on the crest of the dam. Geophone 6 and Geophone 19 (vertical and horizontal, respectively), were located on top of the seepage zone F2 (Figure 2-2B).

Two techniques of seismic survey were adopted in this experiment. The first one is the active method in order to characterize the soil layers inside the body of the dam using the shear-wave velocity profile (V_s). It was not intended for monitoring the water seepage inside the channel. Active measurements were conducted by using a sledgehammer as an active source at the two ends of the profile. Shots were performed in a perpendicular direction to the row of receivers. This method enhances the S-wave amplitude and decreases the P-wave amplitude. The testing was repeated at different heights of water. The sampling frequency adopted during data acquisition was of 8,000 Hz. The refraction technique was conducted for the V_s profile by picking the arrival times and computing the wave velocities.

The second method is the passive seismic listening. In this experiment, the main goal behind using seismic monitoring was to be able to detect the seismic activity caused by the water flow at different flow rates. The sampling frequency adopted for the data acquisition is of 500 Hz similar to the sampling frequency used in the laboratory experiment. Data acquired during the increase of the height of the water in the reservoir was not represented in the analysis because the valve was closed during this process. The seismic data represents a study of the time series during the experiment. The time-frequency analysis (spectrogram) is studied for both geophones (horizontal and vertical) on top of the seepage channel (geophone 6 and 19 respectively). The Energy Spectrum Density (PSD) which represents the energy of the signal in the frequency of interest with time is extracted for the vertical and horizontal geophones for a time-window of 2s. The energy obtained at different times of the experiments were smoothened using the Savitzky-Golay smoothing filter at a polynomial order of 1 and a frame length of 101 data points.

2.2 Results

Figure 2-4 represents the timeline of the seismic and electrical resistivity monitoring. Dashed lines correspond to the end of seismic monitoring corresponding to a height of water of 187 cm in the reservoir. The experiment started by first taking measurements when the dam was completely empty followed by readings at different heights of water in the reservoir.

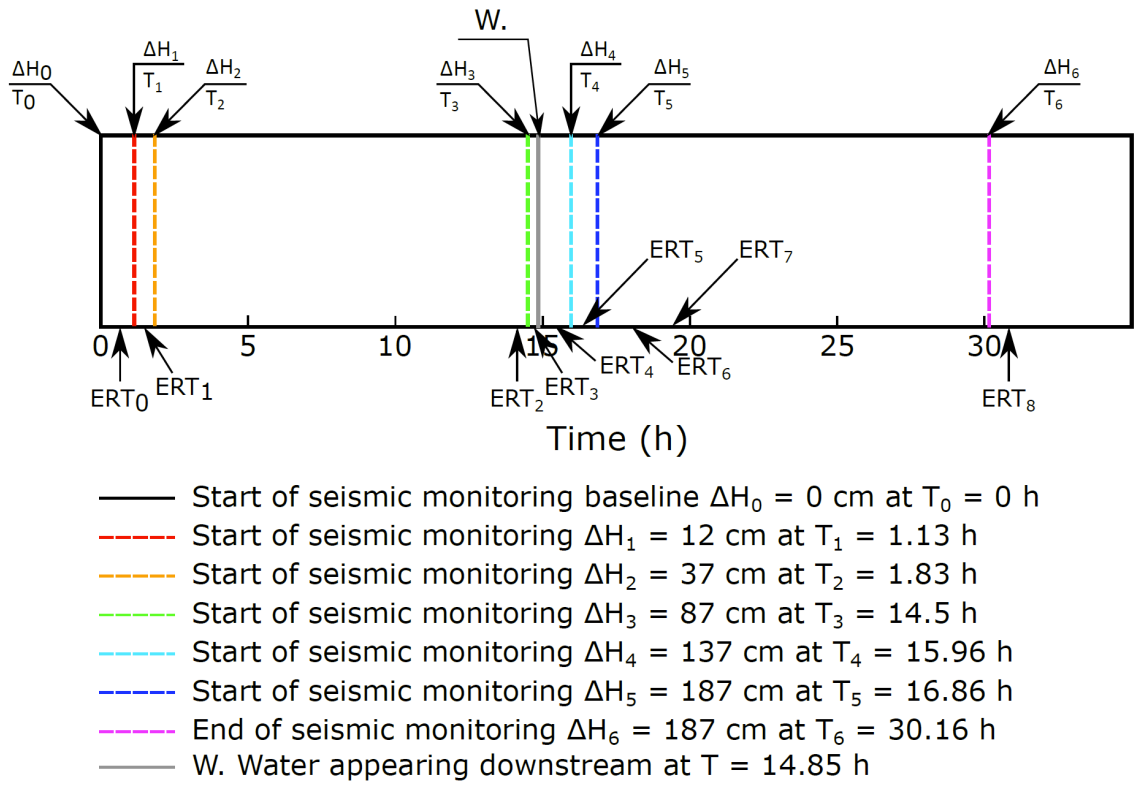

Figure 2-4: Timeline of the geophysical measurements.

2.2.1 **Electrical Resistivity Monitoring**

Geometric factor analysis

Figure 2-5A represents the analytical geometric factor K_a and the corrected geometric factor K_{corr} as a function of the electrode spacing a. It can be noticed that for a small spacing (0.5 and 1 m), the values of the analytical and corrected geometric factors are close as shown in Figure 2-5B. Once the a spacing is larger than 2, K_{corr}/K_a decreases indicating an increase in the difference between the analytical value and the corrected one. Moreover, Figure 2-5A indicates that for a spacing larger than 2, the corrected geometric factor K_{corr} does not increase and reaches a maximum. It starts decreasing and stabilizes at a spacing of 3.5 m which is not the case of the analytical geometric factor K_a that keeps increasing following the equation $K_a = 2\times\pi\times a$ for Wenner configuration.

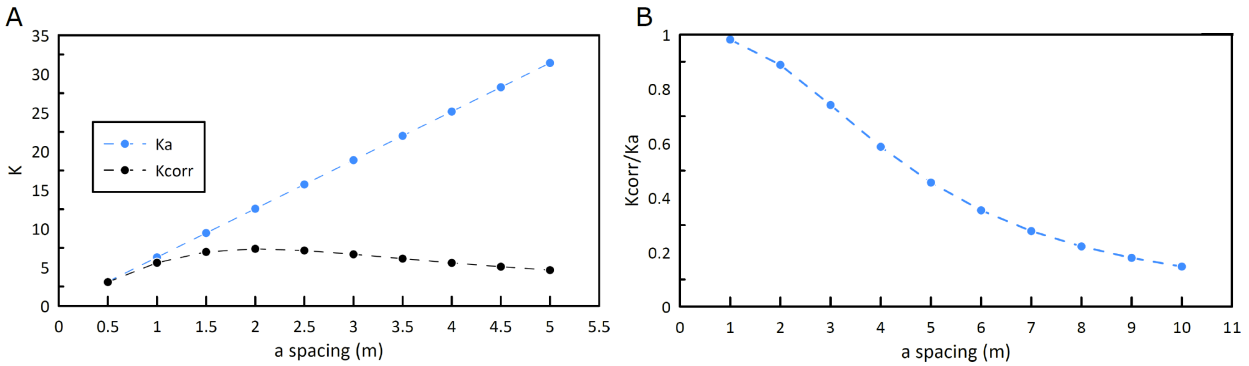

Figure 2-5: A-Representation of the theoretical geometric factor "K_a" for the Wenner configuration and the corrected geometric factor "K_{corr}" as a function of the electrode spacing "a" and B- represents K_{corr}/K_a as a function of the spacing "a".

Timelapse ER analysis

Figure 2-6A shows the coverage and the pre-defined mesh used for the inversion. The coverage is shown to decrease with depth. However, it increases again at a depth 2 m. This could be due to the effect of the geomembrane located at the bottom of the experiment dam.

Figure 2-6B to I represent the timelapse electrical resistivity tomographies corrected for temperature acquired at different heads of water as depicted in Figure 2-4. A high resistivity zone of approximately 200 Ω.m is observed at a depth ranging between 2.0 m to 3.0 m from a distance between 11.0 to 17.0 m. This area corresponds to the presence of the seepage channels F1, F2 and F3. This could originate from the presence of the geomembrane that acts like a barrier to the electric current thus creating this high resistivity zone (observed on all ERTs - Figure 2-6B-I). The body of the dam consists of very fine uniform sand layer as shown in Figure 2-2C thus leading to resistivity values ranging between 20 to 70 Ω.m.

Moreover, it can be seen in Figure 2-6F through I (ERT$_5$ through ERT$_8$ respectively) that the electrical resistivity of the lower area has decreased from 200 Ω.m to approximately 100 Ω.m especially at the location of the F2 seepage channel. This decrease took place when the head was increased to ΔH_4 = 137 cm.

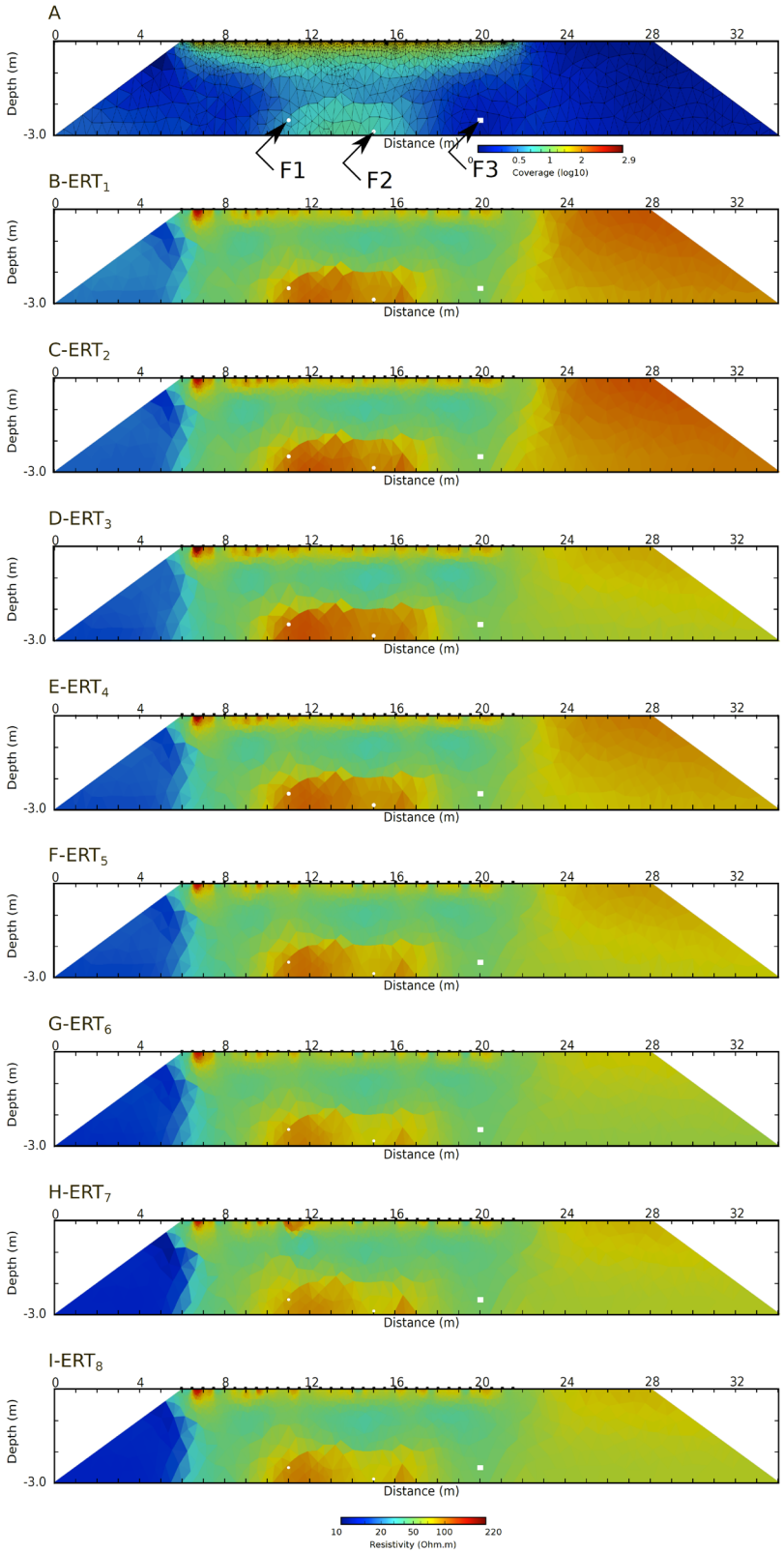
A
B-ERT1
C-ERT2
D-ERT3
E-ERT4
F-ERT5
G-ERT6
H-ERT7
I-ERT8
Depth (m)
-3.0
0
4
8
12
16
20
24
28
32
Distance (m)
F1
F2
F3
0.5
1
2
2.9
Coverage (log10)
10
20
50
100
220
Resistivity (Ohm.m)

Figure 2-6: Electrical resistivity monitoring; A- represents the coverage with the overlayed pre-defined 2D mesh and B through I- represent the timelapse analysis for measurements 1 to 8 respectively as highlighted in Figure 2-4. The seepage channels F1, F2 and F3 are also indicated on the figure.

Timelapse ER ratios

Figure 2-7A to H represent the ratios of ERT_0 to ERT1 through ERT8. There is an increase in the overall resistivity in the body of the experimental dam (ratio approximately of 2). This ratio decreases to approximately 1.5 at ERT_3 when the head of water was of 0.87 m (Figure 2-7C). However, between a distance of 11.0 m and 17.0 m, and at a depth of 2.0 m to 3.0 m, the ER seems to increase slightly above 2. It decreases again to around 1.5 with the increase in the head applied (Figure 2-7D).

Figure 2-7F shows an additional decrease around the location of F2 (distance between 12.0 and 16.0 m; depth between 2.0 m and 3.0 m). This area shows further decreases in the ratios up until ERT_8 in Figure 2-7H.

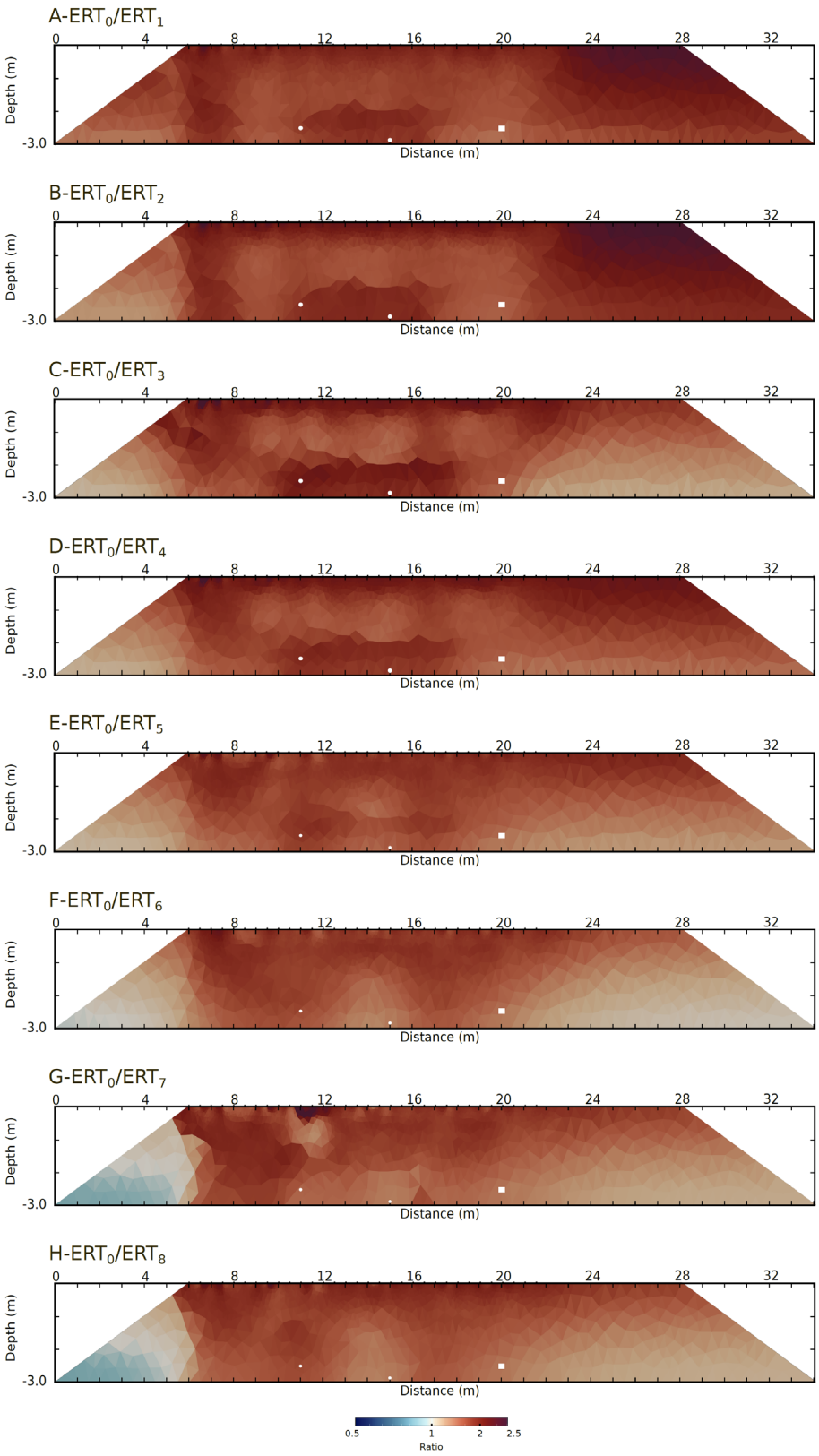

Figure 2-7: Timelapse ER ratios with respect to the baseline ERT_0; A-H represent the ratios of the conducted ERTs (from 1 to 8 respectively) to ERT_0.

2.2.2 **Active Seismic**

The shear wave velocity profile is summarized in Table 2-2. The first layer of 0.7 m depth is of 175 m/s which corresponds to poorly compacted sand layer. A slight increase to 275 m/s is obtained up to a depth of 2.0 m which is due to the further compaction of sand layers with depth. Below 2.0 m, V_s increases to 450 m/s which is close to the base of the dam. At 3.0 m there exists a geomembrane which might affect the velocity of the waves. Repeated measurements analysed did not show any changes with the variation of the head of water in the reservoir. The V_s profile acquired is in agreement with measurements conducted previously on the experimental dam. The depth of 2.7 m achieved instead of 3 m (location of the geomembrane) is due to the resolution of the technique used.

Table 2-2 The corresponding shear wave velocity (V_s) profile.

Layer	V_s (m/s)	Depth (m)
1	175	0.7
2	275	2.0
3	450	

2.2.3 **Seismic Monitoring**

Vertical geophone: Broadband Analysis

The changes in head (*ΔH;* refer to Figure 2-4B) with time is shown in Figure 2-8A. All the seismic recordings in this study consist uniquely of data acquired once the head was reached and the valve was open to allow water to freely seep in F2. The unfiltered data acquired from the vertical geophone located on top of F2 is shown in Figure 2-8B. The time-frequency analysis of the data is shown in Figure 2-8C. The dashed grey lines in all the figures delineate the time and *ΔH* referred to in Figure 2-4.

The first stage (baseline) reflects the background noise captured during the experiment especially that the experimental site is located next to a highway. At T_1, the seismic monitoring for ΔH_1 = 12 cm started. The seismogram for this period (between T_1 and T_2) does not reflect any changes due to the water seepage. On the contrary, the seismogram does not represent increase in amplitude because the activity next to the setup was stopped for better data acquisition. At T_2, the data shows a peak right at the beginning of water seepage at ΔH_2 = 37 cm followed by small amplitude events. The monitoring of ΔH_2 was continuous during the night which is visible in the low amplitude period between T_2 and T_3 due to the decrease of the surrounding activity (people on site, cars on the highway, among others). An increase is observed again during the morning before T_3 which represents the beginning of data acquisition for ΔH_3 = 87 cm. As shown in Figure 2-4 and Figure 2-8A, water appears downstream at T = 14.85 h. The high amplitude seismic events that rose

following the water seeping at the downstream could be due to the presence of a truck during this time. At T_4, monitoring of ΔH_4 = 137 cm took place. No remarkable seismic events appeared on the seismogram. Finally, at T_5, monitoring of ΔH_5 = 187 cm started and continued overnight. High amplitude seismic events took place at the moment water was allowed to flow in F2. Following that, 7 high amplitude bursts are noticed. Similarly to ΔH_2 = 37 cm, low amplitude is noticed during night time. However, it is slightly higher due to the seismic noise originating from the flipping of the double tipping bucket.

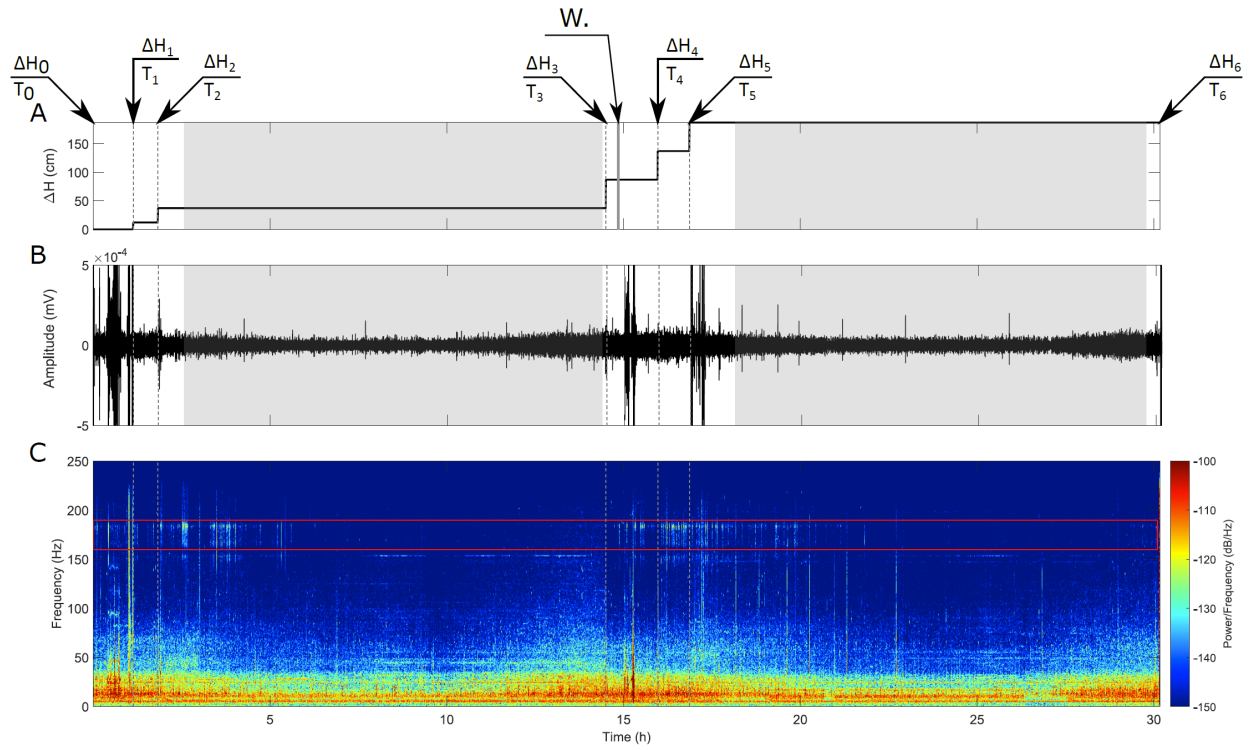

Figure 2-8: Seismic recordings of the vertical geophone located on top of the seepage zone (geophone 6) with varying ΔH; A- Changes in ΔH with time – dashed grey lines delineating the increase in ΔH, B- Time series depicting the seismic activity during the changes in ΔH shown as grey dashed lines and C- Time versus frequency (spectrogram) analysis of the time series shown in B – the dashed grey lines delineate the changes in ΔH. The grey rectangles correspond to the night periods.

The time – frequency analysis in Figure 2-8C permits better understanding of the origin of the seismic events observed in Figure 2-8B. The main dominating part of the spectrogram is the low frequency (between 5 Hz and 25 Hz) background seismic noise that is present throughout the experiment during the day and decreases during the night. Energetic bursts (up to 50 Hz) appear between T_0 and T_1 (baseline) corresponding to the high amplitude event in Figure 2-8B. Another event is shown to radiate up to a frequency of 220 Hz just before T_1 and is most probably due to the activity around the experiment. Another high energy signal is observed between T_3 and T_4 which represents a truck passing next to the experimental dam. Besides the energy captured due to the activity surrounding the experiment, higher energy is observed in the 160 – 190 Hz frequency band (highlighted in Figure 2-8C by a red rectangle) following every increase in ΔH

(ΔH_2, ΔH_3, ΔH_4 and ΔH_5). This energy was not present in the baseline and seems to fade away after a certain time of water seepage.

Vertical geophone: 160 – 190 Hz frequency band analysis

The flow rates recorded using the double tipping bucket of 1 L are shown in Figure 2-9A. No flow rates existed prior to ΔH_3 = 87 cm. The data acquired by geophone 6 is filtered in the frequency band of interest which is of 160 – 190 Hz and is shown in Figure 2-9B. Moreover, the PSD at 170 Hz is shown in Figure 2-9C with the smoothened data in red.

At a first glimpse, seismic activity is identified during the acquisition of the baseline (T_0). This is due to the activity around the experiment making sure that the systems are working. Starting at T_1 for a ΔH_1 = 12 cm, very low seismic activity can be detected and is characterized by low energy in the PSD.

At T_2, for a ΔH_2 = 37 cm, high energy event is observed and is due to the opening of the valve. Approximately 1 h after opening the valve, high seismic energy appears and lasts for 3.5 h then the system seems to go back to a calm stage where very few high amplitudes are noticed during the night time.

In addition, at T_3, one high amplitude event can be observed in Figure 2-9B that is followed by water appearing downstream (W. in Figure 2-9). The system is again triggered and shows an increase in energy for approximately 30 mins then goes back to rest. This increase and decrease in energy coincide with the slight increase and decrease in the flow rate.

Similarly, at T_4, increase in energy is detected with the increase in flow rate. However, the decrease in flow rate did not implicate any decrease in energy and that is observed in both the seismogram and PSD (Figure 2-9B and C respectively). Moreover, at T_5, following the opening of the valve, high energy is detected during the first 30 mins when the flow rate reaches 8 L/min and decreases abruptly to become embedded in the energy generated by the surrounding activity at approximately 20 h.

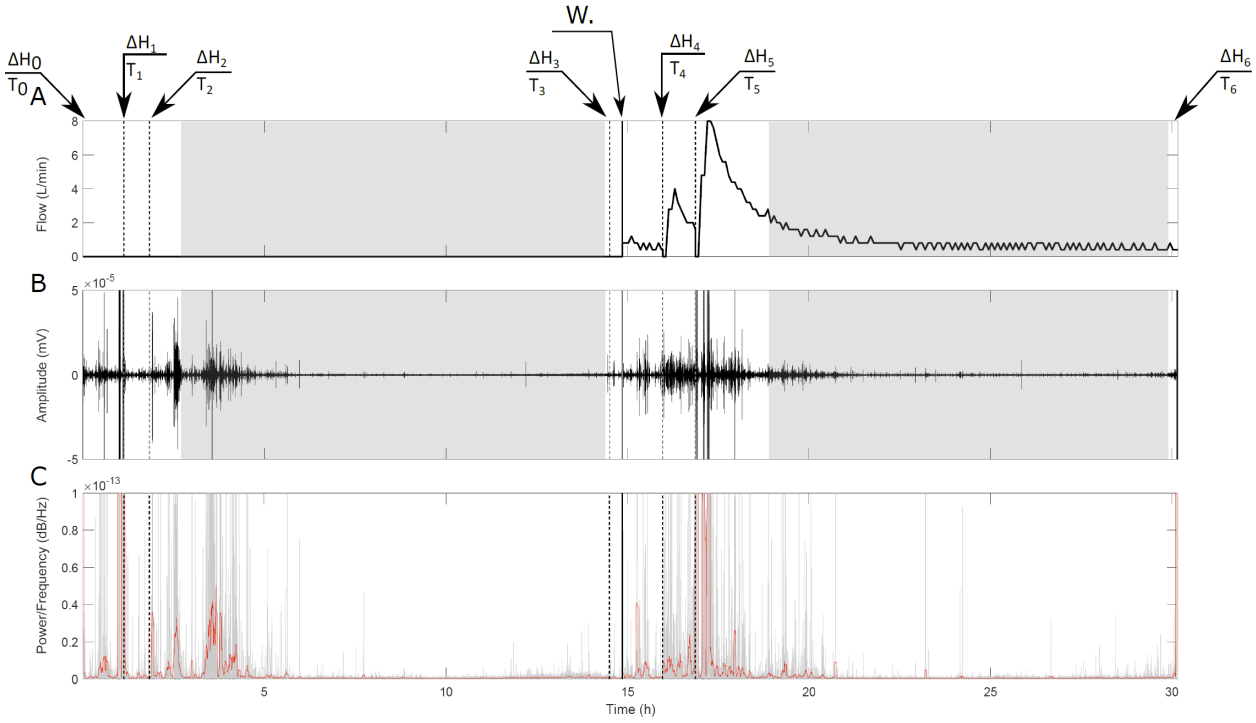

Figure 2-9: A- the flow rate recorded during the experiment, B- the Filtered seismogram of the vertical geophone (6) at a frequency band of 160 – 190 Hz and C- the PSD centered at 170 Hz with the grey and the red data showing the unsmoothed and the smoothed data respectively. The dashed lines represent the times and heads as shown in Figure 2-4.

Horizontal geophone – Broadband Analysis

Figure 2-10 shows the analysis conducted on the horizontal geophone located on top of F2. The horizontal geophone on top of the seepage zone shows an activity in the 160 – 190 Hz band frequency range shown in Figure 2-10C similarly to the laboratory experiment, highlighted in a red rectangle. Moreover, at 200 Hz (frequency band of 180-220 Hz highlighted in the cyan rectangle in Figure 2-10C), which is another multiple of the 50 Hz electric energy, a strong seismic activity is observed after increasing the head to ΔH_5 = 187 cm. This energy seems to decrease with time towards the end of the experiment. It is present as bursts as well in the beginning of the experiment but at a lower energy. In addition, a somehow stable energy (mainly due to the electric energy) is depicted at around 100 Hz (frequency band of 90-120 Hz highlighted by a magenta rectangle in Figure 2-10C) that exhibits changes in the energy at around 3 h following the increase in ΔH to ΔH_2 = 37 cm probably due to the flow of water. The data in this latter frequency band (90 – 120 Hz) is mostly affected by the flipping of the double tipping bucket and its analysis is presented in Appendix C.

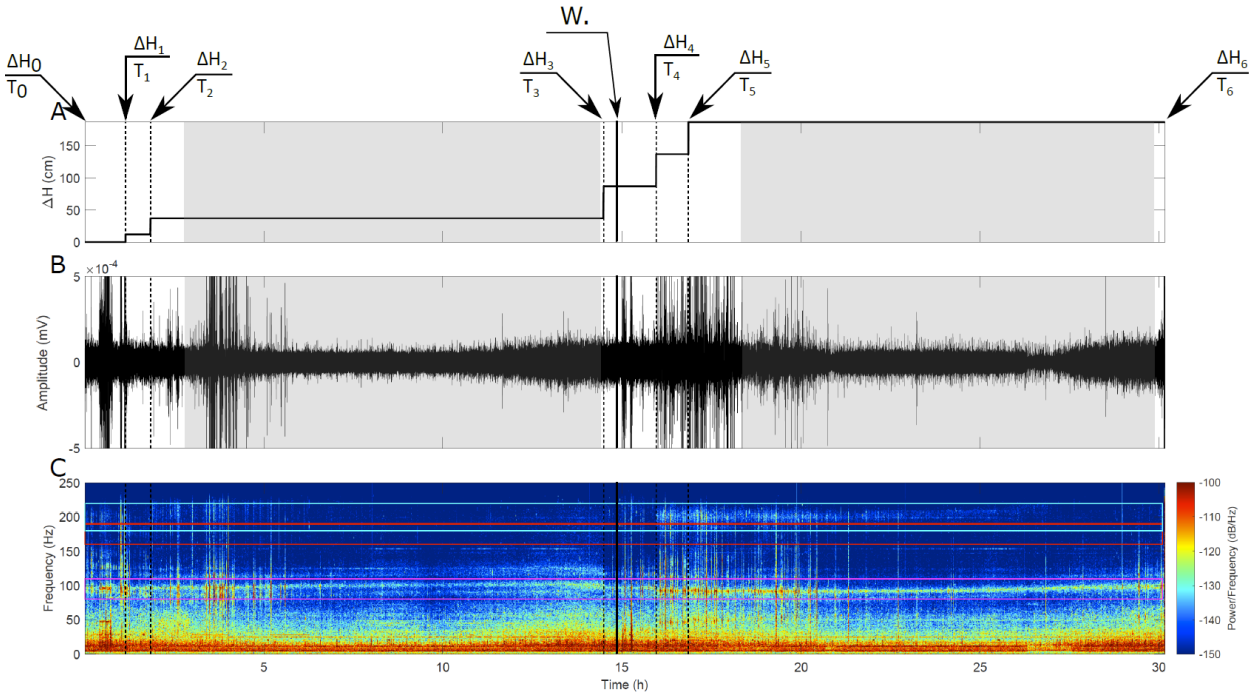

Figure 2-10: Seismic recordings of the horizontal geophone located on top of the seepage zone (geophone 19) with varying ΔH; A- Changes in ΔH with time – dashed black lines delineating the increase in ΔH, B- Time series depicting the seismic activity during the changes in ΔH shown as black dashed lines and C- Time versus frequency (spectrogram) analysis of the time series shown in B – the dashed black lines delineate the changes in ΔH – the magenta rectangle shows the frequency band of 90-120 Hz, the red rectangle shows the frequency band of 160-190 Hz and the cyan rectangle shows the frequency band of 180-220 Hz.

Horizontal geophone: 160 – 190 Hz frequency band analysis

Following the seismic activity detected in the laboratory experiment in the 160 – 190 Hz frequency band, it was chosen to verify whether any activity could be detected similarly in the experimental testing on the horizontal geophone. The seismogram was filtered at a frequency band of 160-190 Hz and is presented Figure 2-11B. The corresponding PSD centred at a frequency of 170 Hz (grey) and the sgolayfilt (red) is shown in Figure 2-11C.

Very low activity is noticed between T_0 and T_2 except at the end of T_1. Whereas at T_2 high amplitude signals are detected following the opening of the valve and is detected in even higher amplitudes during the low activity period highlighted by the grey rectangle.

At T_3, activity is detected that is higher prior to opening of the valve. It is more apparent and marked following ΔH_4 and ΔH_5. It is also present in the low activity period during the night time up to approximately 20 h of the experiment.

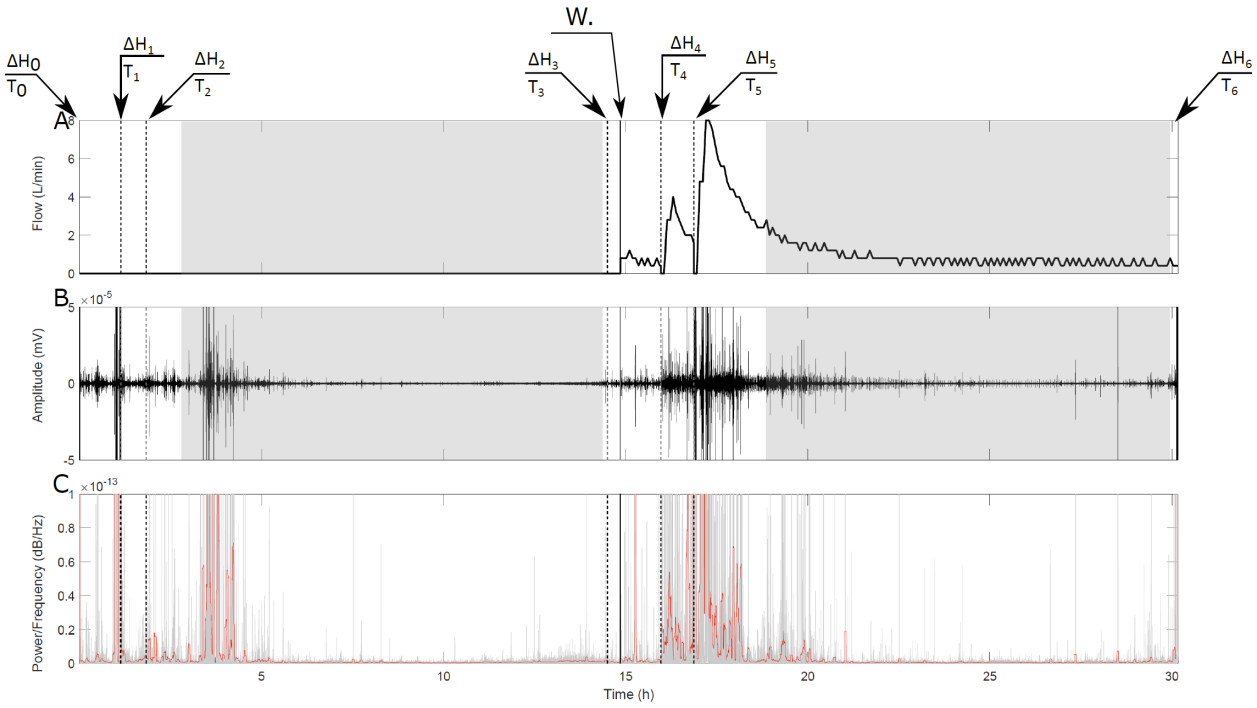

Figure 2-11: Analysis of the horizontal geophone (geophone 19); A- Flowmeter measurements with time of the experiment, B- Filtered seismogram in the 160 - 190 Hz band frequency and C- the PSD of geophone 19 at 170 Hz; the grey data represent the unsmoothed PSD whereas the red data represent the smoothed PSD.

Horizontal geophone (Geophone 19): 180 – 220 Hz frequency band analysis

The recorded flow rates from the double tipping bucket data are shown in Figure 2-12A. No flow rates existed prior to ΔH_3 = 87 cm. In Figure 2-12B, the filtered seismogram at a frequency band of 180 to 220 Hz is represented. It shows high amplitude values following the increases of heads (ΔH_2, ΔH_4 and ΔH_5).

At ΔH_3, lower values of high amplitudes are depicted compared to ΔH_2, ΔH_4 and ΔH_5. Noticeably, repetitive events are noticed at around 23 h and they originate from the flipping of the bucket of the flowmeter equipment installed at the downstream in addition to the ones originating from the seepage zone.

The energy at ΔH_1 is low because the head applied of 12 cm is very low to induce seismic energy. At ΔH_2, the energy increases slightly following the increase in head to 37 cm; but at 3 h, the energy increases gradually and decreases again slightly before 5h. Following this period, the system seems to have entered an at-rest phase where the energy decreases and increases to some extent again following the appearance of the water downstream (W. in Figure 2-12A). Following the increases to ΔH_4 and ΔH_5, the energy increases and decreases gradually with the decrease of the flow rate at

25 h. The energy was high as well during the night (compared to the 37 cm data at night) which indicates that the source is indeed originating from the seepage.

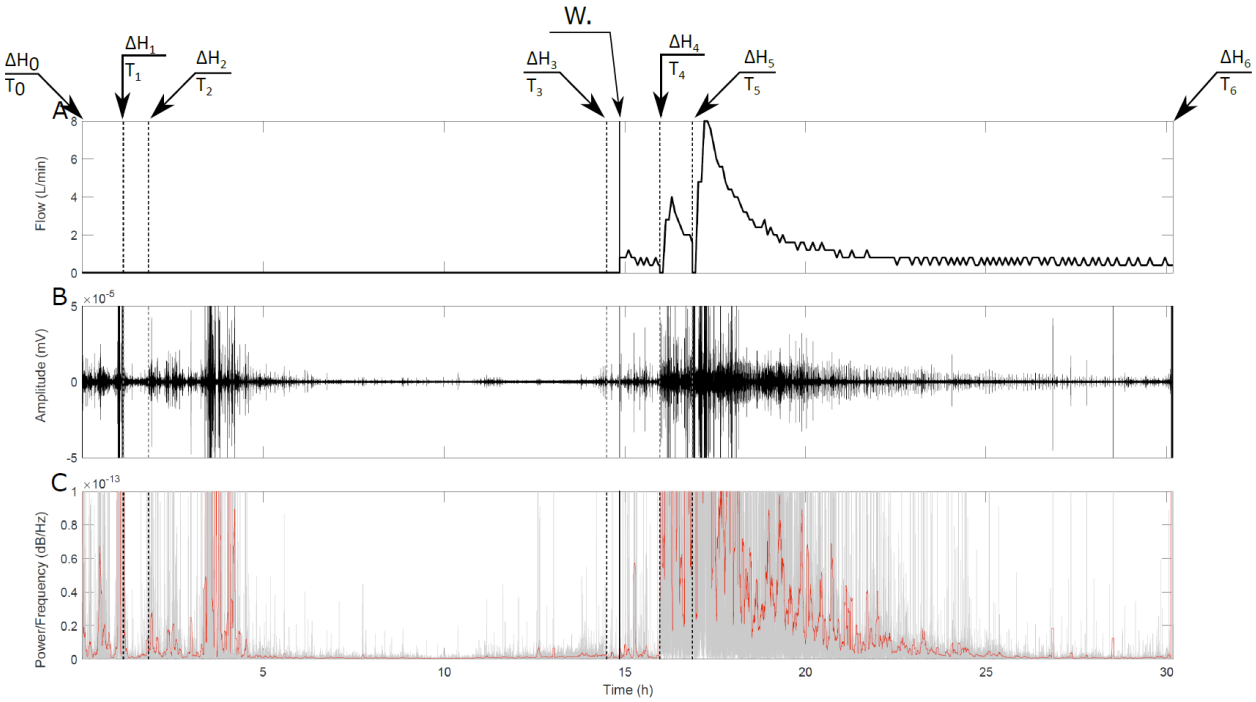

Figure 2-12: A- the flow rate recorded during the experiment, B- the Filtered seismogram of the horizontal geophone (19) at a frequency band of 180-220 Hz and C- the PSD centred at 200 Hz with the grey and the red data showing the unsmoothed and the smoothed data respectively. The dashed black lines represent the different increases in heads.

2.3 Interpretation and Discussion

The electrical resistivity technique used in this experiment does not provide much information about the water flow in the seepage channel (F2). The application of the temperature corrections was necessary in the case of this study because of the important changes in temperatures between the day and night (almost 15°C). The drop in the ratios of ER compared to the initial reading ERT_0 is unlikely to be linked to the presence of water especially that the seepage zone was wrapped in a geotextile. This decrease could be due to the presence of water in the reservoir that is causing this effect.

Active seismic technique allowed the determination of different layers that constitute the experimental dam. However, this technique was not intended to identify leakages or anomalies within the dam.

The results of the passive seismic technique for monitoring water seepage in a porous medium showed an increase in the energy in the 160-190 Hz frequency band related to the increase in the head at the upstream. The increase in the energy was depicted in both the horizontal and vertical

geophones placed on top of the seepage channel (Figure 2-10 and Figure 2-8 respectively). At a head ΔH_2 = 37 cm, no water flow rate was registered at the downstream yet high energy was depicted following the increase in the head (Figure 2-11B). This is due to the water flow inside the channel and the soil/water interaction. For the head of ΔH_5 = 187 cm, a decrease in the energy is observed due to the decrease in the flow as shown in Figure 2-11C. The seismic noise did not disappear but the surrounding noise for this flow rate is higher than the energy emitted by the low flow.

The system constituted of the dam and the water flow undergoes stages of activity and steady state phases. The latter is explained by the increase and decrease in energy that is observed following the soil/water interaction. This decrease in energy is identified at moments when the flow of water decreases. The results obtained are in line with previously conducted studies that show increase in energy related to increases in flow rates (Parekh et al., 2016).

2.4 Limitations

During this experiment, technical problems were encountered. The objective was to reach high flow rates that would induce turbulent flow of water. However, the low flow rate was enough to create seismic activity that was recorded. In addition, the high flow rate could not be monitored during a long period of time and decreased throughout the monitoring. Also, the presence of the geotextile around the seepage channel and the geomembrane placed at the bottom of the dam made it hard to obtain satisfactory results when using the electrical resistivity technique.

2.5 Conclusions and Perspectives

In this experimental field dam, electrical resistivity and seismic techniques were explored to monitor seepage in a porous medium. The experimental dam consisted of 3 channels of high permeability embedded inside a low permeability body of the dam. Only one seepage channel was used in this experiment with varying heads of water applied and flow rates.

The electrical resistivity technique was not very useful in this experiment because of the presence of a geotextile around the seepage channel and the existence of the geomembrane at the bottom of the dam. Even though high resistivity areas are encountered around the locations of the seepage channels (Figure 2-6) that decreased with time (due to water flow). Nonetheless, it was not possible to fully locate the seepage channels. Passive seismic monitoring was more useful and it allowed the detection of the water seepage through the increase in the energy at a frequency of 200 Hz and 170 Hz in the PSD whenever the water head was increased.

This concludes that the seismic energy increases with the increase of the head applied and the increase in the generated water flow. It also shows that the increase is not permanent; after a certain

period, it goes back to the steady state period and is embedded in the surrounding noise whenever the flow of water decreases.

In this experiment, the internal erosion was not tackled because of the geotextile placed at the downstream to inhibit any movement of particles outside the seepage channel. Nonetheless, the techniques applied proved to be useful in the field for detecting impulsive events originating from the seepage of water. However, this energy dissipates in the energy of the surrounding activity and is not detected anymore which paves the way to new experiments attempting to detect the time required and the factors affecting the instability of the seepage channel causing the internal erosion mechanism to take place. This is achieved by various cycles of emptying and filling the experimental dam to monitor the fatigue and aging effect of the materials on the seismic technique.

CHAPTER 3
Water Seepage in Porous Media: Laboratory Experiment

The study conducted in the field in Rouen was focused solely on the water seepage in a confined pipe. However, the understanding of the evolution of the porous medium and monitoring its susceptibility to internal erosion is still complicated and was not tackled. The objective in this chapter is to monitor a porous medium subjected to varying water heads (thus changing flow rates) in order to better understand the changes that are taking place in the structure of the soil sample that would induce internal erosion. For this purpose, a laboratory experimental setup was built in the objective of inducing water flow uniquely in a porous medium excluding water seepages that might take place in other soil areas of the experiment. The same diameter of the pipe was used. The setup was monitored continuously using electrical resistivity and seismic techniques in order to detect the electrical resistivity and seismic responses to changes of heads applied upstream (thus changes in the flow rates).

3.1 Experimental Setup

The laboratory setup consists of a plexiglass tank for water storage, a concrete beam and a hose as schematized in Figure 3-1. The plexiglass tank has a diameter of 0.5 m and a height of 1.25 m and serves as a water supply to the system. A hose was introduced in the tank to increase the water head whenever needed. The beam shown in Figure 3-1 consists of concrete mixed at a low water to cement ratio to increase its strength. A cylindrical hole 0.1 m in diameter was intentionally left to insert the soil specimen. The tank is connected to the seepage zone in the concrete beam through a PVC pipe. The extension of pipes at the downstream is used to conduct a saturation phase prior to increasing the head of water in the tank. A filter consisting of a cloth was placed at the downstream to avoid the collapse of the soil specimen following the first contact with water. The temperature of the water was monitored manually throughout the experiment following every increase in head.

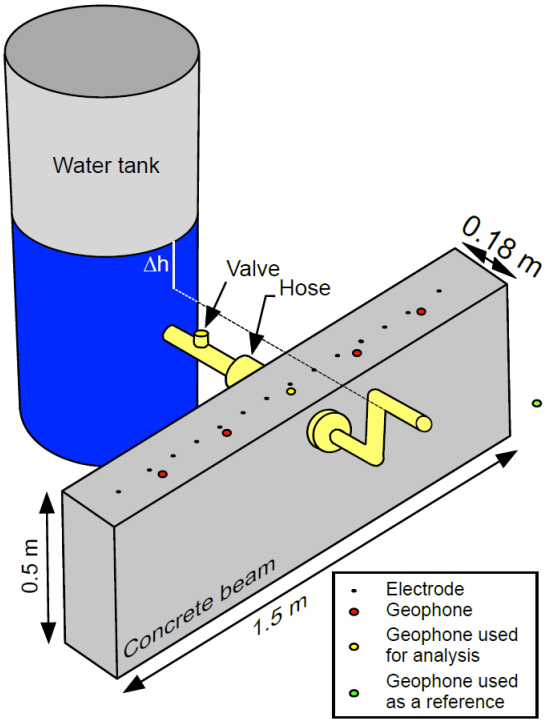

Figure 3-1: Laboratory setup showing the extension of pipes placed downstream for the saturation phase, the geophones and electrodes placed on top of the concrete beam and the tank of water for the control of head.

3.1.1 Geotechnical Characteristics of the Seepage Zone

A mixture of 65% sand and 35% of lean clay was chosen. The sand was passed through sieve no. 4 (4.75 mm opening). The sieve analysis was conducted according to international standard D6913

(ASTM, 2017). The granulometric distribution shows that the soil is a sandy clay with more than 50% retained on the 0.075 mm-opening sieve. The sample was mixed at the Optimum Moisture Content (OMC) of 11.3%. In order to have a longer experiment and increase the acquisition time, the soil sample was compacted to reach a dry density of 18.25 kN/m^3. For this purpose, 5 batches of approximately 550g of the soil mix were introduced in layers and compacted.
The specific gravity G_s was determined using standard D854 (ASTM, 2014) and was estimated to 2.66 ± 0.01. The void ratio was estimated to e = 0.43 ± 0.01, leading to a critical hydraulic gradient i_c of 1.16 ± 0.01. Given the length of the soil sample of 18 cm, the critical head Δh_c (difference between upstream and downstream head) to be used to initiate internal erosion is 20.89 ± 0.01 cm.
At the end of the soil sample preparation, a mesh was installed at the downstream side in order to avoid any soil collapse during saturation phase. The filter mesh was supported by a plastic grid. The filter mesh and the plastic support were both connected with a thread from one side while the other side was extended beyond the downstream pipe to permit its removal following the saturation phase.

3.1.2 **Electrical Resistivity Tomography**

Electrical resistivity was conducted using 14 electrodes at a spacing of 10 cm. Pre-drilled holes were performed in the top of the concrete beam up to a depth of 1 cm and a diameter of 0.5 cm (similar to the diameter of the electrodes) in order to insert the electrodes firmly and decrease the contact resistance as much a possible. Moreover, salty water was introduced only once at the beginning of the experiment in the holes to facilitate the injection of the current. A single channel AGI Supersting resistivimeter was used for data collection. The Dipole Dipole (DDP) array configuration was adopted for the data acquisition using 74 measurements. The single channel equipment would lead to a duration of 10 min per acquisition. However, unaware of the changes that might occur in the soil sample during the increase in head and the rapid evolution of the experiment, it was decided to decrease the number of measurements hence decreasing the acquisition time keeping in mind a good horizontal and vertical resolution. For this purpose, forward-modelling (already conducted in a study by Bièvre et al. in 2018) was conducted using F3DM package (Clement & Moreau, 2016) on a pre-defined mesh built using COMSOL Multiphysics. The pre-measured resistivities of concrete and soil sample were introduced in the forward calculations (500 Ω.m and 300 Ω.m respectively). The sequence with the highest coverage (optimized sequence) in the soil sample compared to the 74 measurements (complete sequence) was chosen.
Data acquired using a 2D profile were inverted using BERT package (Rücker et al., 2006) in 3D with a pre-defined 3D mesh. This technique was adopted because of the particularity of the geometry of the electrodes, the size of the object and a finite domain. The changes in the contact resistance between the concrete and the electrodes could not permit the use of a fixed resistivity in the concrete considering that the changes will exclusively happen in the seepage area. Therefore, inversion was allowed in the entire medium. Considering that most changes should occur in the

soil sample zone, smoothness decoupling was used between the 2 zones (50 % decoupling). Results were evaluated in terms of reconstruction of the resistivity distribution and of statistical results such as χ^2 and Relative Root Mean Square Error (RRMSE, in %).
The use of the timelapse technique with the previous model as the starting was adopted in order to monitor the electrical resistivity changes taking place inside the soil specimen during water seepage at varying heads.
The mean resistivity in the soil sample was computed using a volume and coverage weighted average (Bièvre et al., 2021):

$$\rho_{mean} = \frac{\sum_{i=1}^{n} \rho_i \times V_i \times S_i}{\sum_{i=1}^{n} V_i \times S_i} \quad (5)$$

Where ρ_{mean} is the weighted average resistivity of the soil sample (Ω.m), ρ_i, V_i and S_i correspond to the resistivity (Ω.m), Volume (m^3) and Coverage respectively of a cell i.

3.1.3 Seismic Monitoring

The experiment was continuously monitored using 5 vertical geophones of 4.5 Hz nominal frequency located on top of the concrete beam with a spacing of 30 cm. A reference geophone was placed on the ground next to the concrete beam in order to monitor the seismic activity in the laboratory. Seismic data were collected at a sampling frequency of 500 Hz. The data obtained solely from the geophone on top of the seepage zone will be analysed because the recordings on the 5 geophones show similar results due to the high wave velocities in the concrete beam. Following data collection, the time series at broadband were investigated and the spectrogram obtained following a Fast Fourier Transform (FFT) led to the identification of frequency bands where the presence of high energy is observed post water seepage. The time series were filtered in this frequency band and the Energy Spectrum Density (PSD) at a centred frequency using a 2-s time window was obtained to monitor the changes in the activity following the increase in the heads of water. The Savitzky-Golay smoothing filter at a polynomial order of 1 and a frame length of 101 data points was adopted for PSD data smoothing.

3.2 Results

3.2.1 Experimental Protocol and Visual Interpretation

The experiment consisted on partially saturating the sample prior to increasing the head in the upstream. The head at the downstream remained constant throughout the experiment. The chronological timeline of the water head throughout the experiment is shown in Figure 3-2 and the summary of the stages are indicated in Table 3-1. The experiment starts with baseline (index 0 at $T_0 = 0$) monitoring with no water in the setup. This phase lasted 0.22 h (13.3 min, index 1). Following this phase, water was introduced in the downstream through a squeeze bottle to fill the downstream pipe and in the same time filling the water tank to the same level at the downstream

at 0.49 h – index 2. The ΔH (difference in head between the upstream and the downstream) remained 0 because the head of water at both sides was equal. At 0.56 h (index 3), the water in the tank was increased to reach ΔH = 5.5 cm at 0.75 h (index 4). The head of water upstream was not kept stable Once the desired head was reached, the water supply was cut off and the water was allowed to infiltrate the soil sample freely. Following the increase in the head, the system was monitored until 17.17 h. During this phase, the first drop of water appeared downstream at 0.77 h (index 5). The filter was removed at 16.68 h (index 6). Visual changes such as soil particles detachment at the downstream were observed following the filter removal and turned the water downstream turbid which made it impossible to see the changes at the downstream. After 17.17 h (index 8), the head of water upstream dropped by 1 cm and had to be increased again to reach 5.5 cm at 17.18 h (index 9). The system was again monitored until 25.81 h (index 10) when an additional increase of head was introduced to reach ΔH = 13.5 cm at 26.01 h (index 11). Following this increase, the experiment was monitored until 47.55 h (index 12). The head upstream decreased by 2.5 cm and had to be increased again to ΔH = 13.5 cm at 47.6 h (index 13). Monitoring continued until 48.93 h – index 14 and then the head was increase to reach a ΔH = 18 cm at 49.03 h (index 15) which was still lower than ΔH_c of 20.89 cm. Monitoring proceeded until 52.33 h (index 16) when the head was increased once again to ΔH = 22.5 cm at 52.44 h (index 17). The critical difference in head ΔH_c was exceeded. The experiment was monitored at this head until 53.30 h (index 18) when the water head upstream was increased gradually to attain 60.5 cm at 54.43 h (index 21) when the soil was pushed out of the concrete beam (index 22).

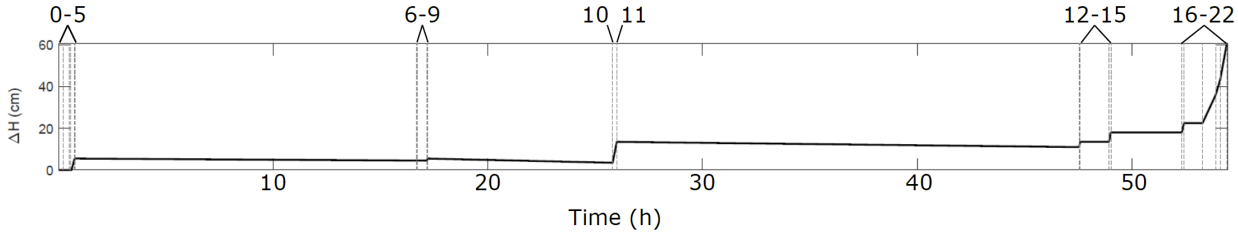

Figure 3-2: Changes in head applied at the upstream as a function of time. The indices represent the stages in the experiment detailed in Table 3-1.

Table 3-1: Summary of the experiment stages

Index	Time (h)	Stage
0	0.00	Baseline
1	0.22	Head Downstream and Upstream
2	0.49	ΔH=0 cm
3	0.56	Increase of Head
4	0.75	ΔH=5.5 cm
5	0.77	Water Downstream
6	16.68	Filter Removal
7	16.70	Changes Downstream
8	17.17	ΔH=4.5 cm/Increase of Head
9	17.18	ΔH=5.5 cm
10	25.81	ΔH=3.5 cm/Increase of Head
11	26.01	ΔH=13.5 cm
12	47.55	ΔH=11 cm/Increase of Head
13	47.60	ΔH=13.5 cm
14	48.93	Increase of Head
15	49.03	ΔH=18 cm
16	52.33	Increase of Head
17	52.44	ΔH=22.5 cm
18	53.30	Increase of Head
19	53.91	ΔH=36 cm
20	54.12	ΔH=43.5 cm
21	54.43	ΔH=43.5 cm/Failure
22	54.48	End of Experiment

3.2.2 **Electrical Resistivity Monitoring Results**

3.2.2.1 Synthetic model of the complete and optimized sequence

Figure 3-3a shows the mesh that has been used for the inversions of the electrical resistivity data with the location of the electrodes, the seepage zone and the slice used for the 2D images extracted from the 3D time lapse inversions. The coverage image of the complete (74 measurements) and optimized (37 measurements) sequences are shown in Figure 3-3b. The difference between the complete and the optimized sequences shows a decrease in coverage in the overall beam due to the decrease in the number of data. The decrease in the seepage zone which is the zone of interest is of approximately 30% which is a relatively high value. The area below the seepage zone is shown to be less affected.

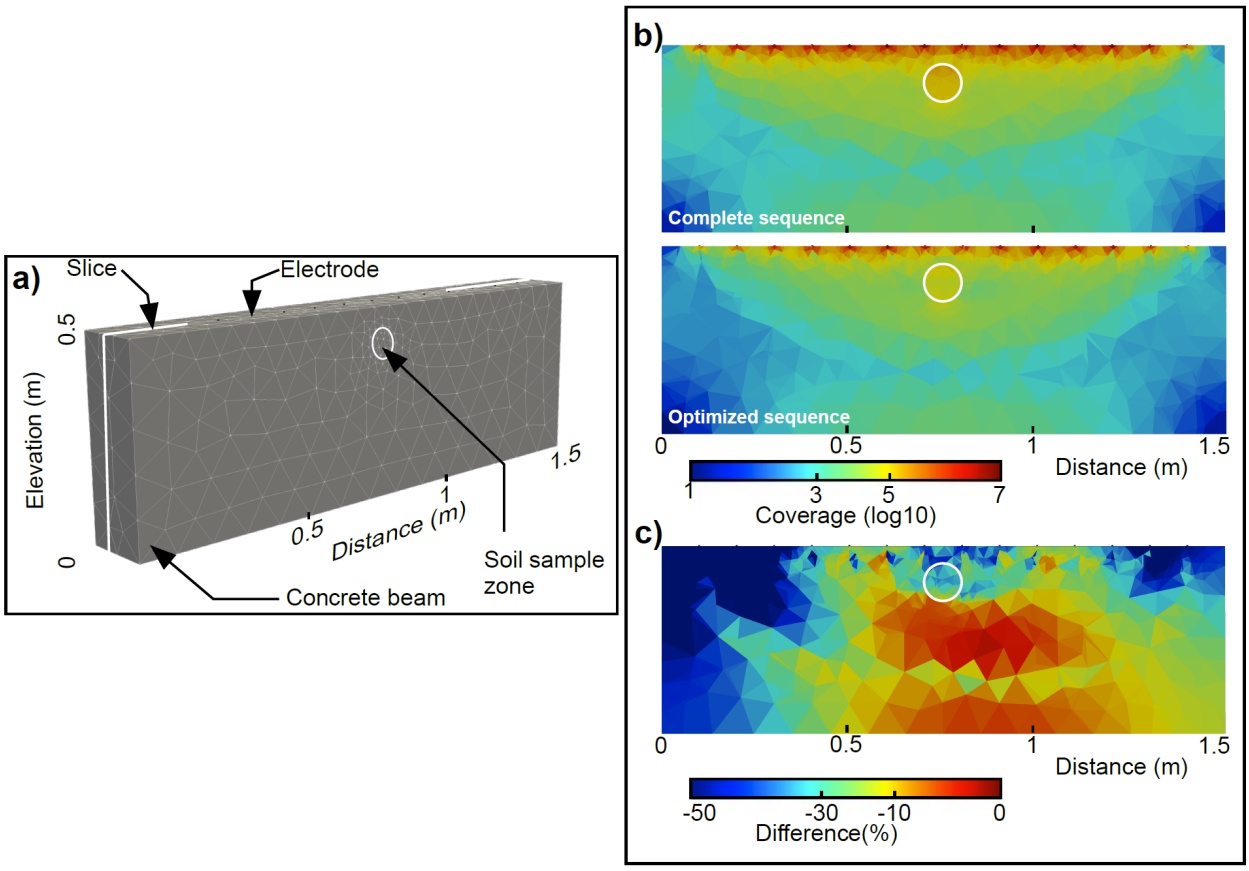

Figure 3-3: Synthetic results with the complete (74 measurements) and the optimized (37 measurements) sequences. a) The mesh used for inversion along with the location of the slice c) Coverage slices from the 3D models along with the difference, expressed in percent, between the complete and optimized sequences. All slices pass through the vertical plane defined by the line of electrodes.

3.2.2.2 ER monitoring of the seepage zone

The acquisition of the water seepage monitoring resulted in 388 files for an approximately 5 min of data acquisition per file. The data in the time slot between 26 h and 49.5 h were registered in a file that was corrupted; hence, there is a lack of a time window of 23.5 h. Figure 3-4A summarizes the changes in heads applied during the experiment in addition to the indices from Table 3-1. Figure 3-4B through F shows the slices of the 3D inversions chosen throughout the experiment at changes of heads applied. The changes reflect a decrease in electrical resistivity data following the introduction of water (Figure 3-4B and C). After 10 hrs, the resistivity starts increasing in the seepage zone which could be the result of higher contact resistances (Figure 3-4D). At 22.5 hours, and following the increase in head to again to 5.5 cm (index 9-10), the resistivity decreases (Figure 3-4E) to increase again towards the end of the experiment (Figure 3-4F).

To better assimilate the changes with time, the average weighted electrical resistivity was computed in the soil sample solely and is presented in Figure 3-4G. It can be noticed that the

starting resistivity value is of around 375 Ω.m that decreases within 12 min to 290 Ω.m. This drop in electrical resistivity data corresponds to the incorporation of salty water in the pre-drilled holes. This facilitated the injection of the current in the concrete and not to the water seepage in the soil specimen since water appeared downstream at 0.77 h (refer to Table 3-1). When time passed, the concrete beam absorbed the salty water and induced an increase in contact resistance between the concrete and the electrodes that resulted in the progressive increase in electrical resistivity up to 380 Ω.m until approximately 16 h.

Following the filter removal and the increase in head, a decrease in resistivity is noticed reaching 360 Ω.m. This decrease can be explained by the increase in water content in the soil specimen. The resistivity is somehow constant (±5 Ω.m) up until 26 h when the last file was acquired.

After re-initiation of the equipment following the corrupted data, the resistivity at 49.5 h has increased again to reach approximately 390 Ω.m. This increase could be explained by changes that took place in the soil medium. It is hard to interpret the type of changes that could have led to this increase. This mechanism could lead to porous voids that would increase the electrical resistivity values especially at the top between the soil sample and the concrete where air bubbles could be trapped.

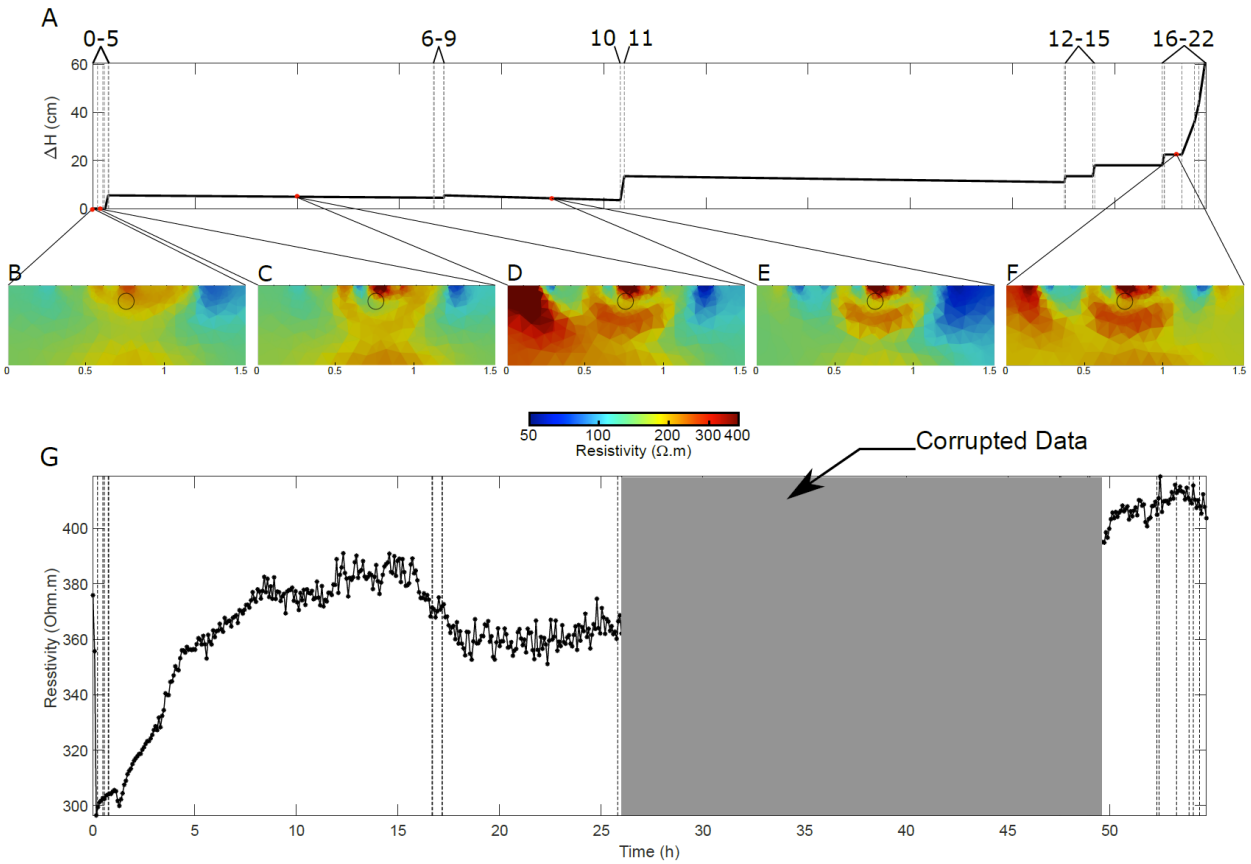

Figure 3-4: A- Changes in heads of water with time and B-F 2D slices performed on the 3D inversions at different times of the experiment and G- Weighted average of the electrical resistivity data in the soil sample with time; the grey rectangle represents the corrupted data that were not successfully retrieved. The dashed grey lines represent the different stages of water filling detailed in Figure 3-2.

3.2.2.3 ER monitoring of the upper and lower part of the seepage zone

To evaluate potential differential resistivity variations between the upper part and lower part of the seepage zone throughout the experiment, the average weighted electrical resistivity data representing the upper and lower parts were presented in black and red respectively in Figure 3-5. The upper portion corresponds to the mid-section of the seepage zone up to higher part . The lower part is the mid-section down to the bottom of the seepage zone. It can be noticed that the values of the upper part throughout the experiment are always higher than the lower part. However, at around a time of 1 h, and following the water flow downstream (index 5), there is a drop in the ER of the lower bound that is not seen in the upper part. This could be due to the increase in water content during this time. A similar change is observed at around 9 h.

At 12 h, there is an increase in the ER in the lower part that is vaguely noticed at the upper part. This could originate from the decrease in water content at the lower part due to decrease in head.

Following the increase in head (index 9), there is a drop of 15 Ω.m in the lower bound and approximately 5 Ω.m in the upper bound which can explained by the increase in water content at the lower part of the medium.

At approximately 49.5 h, both areas of the seepage zone exhibit an increase in the ER values, at 53.30 h (index 18) the lower bound shows a decrease whereas the upper bound shows further increases that would be explained by the further saturation of the soil sample leading the air bubbles and voids to form at the upper part of the seepage zone.

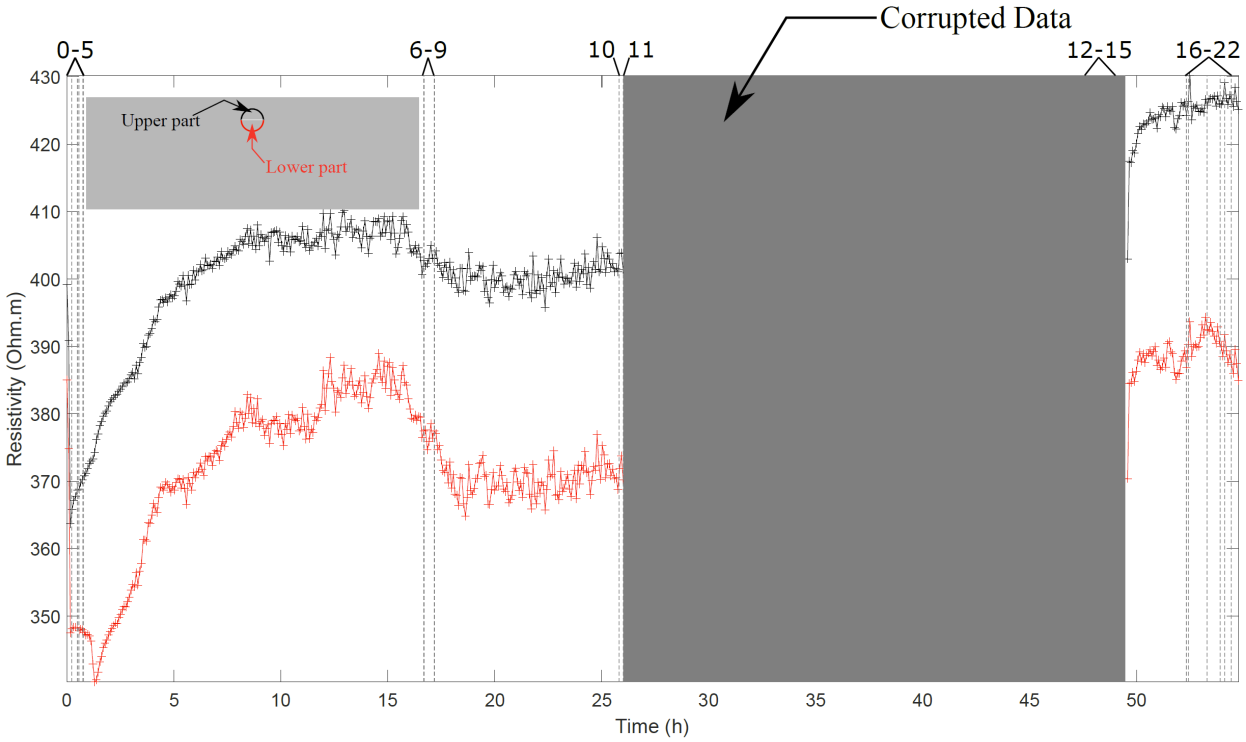

Figure 3-5: Average weighted ER monitoring of the upper part and lower part of the seepage zone presented in black and red respectively. The indices represent the stages of the experiment detailed in Table 3-1.

3.2.3 **Seismic Monitoring**

3.2.3.4 Broadband analysis

The differences in head during the experiment are shown in Figure 3-6A. Seismic data were collected throughout the experiment and are shown in Figure 3-6B. The time series in Figure 3-6B represents the amplitude as a function of time and head difference ΔH in Figure 3-6A. The grey dashed lines represent the stages of the experiment detailed in Figure 3-2 and the grey rectangles highlight the night periods where very little activity was taking place in the laboratory next to the experimental setup.

At first glimpse, high amplitude signals appearing in the time series (Figure 3-6B) are present during the times when there was activity next to the experimental setup (day time) from students working, machineries, the operation of the experiment (increase in head) and water seepage. Whereas during night time (grey rectangles), very few signals of high amplitude can be depicted that might be linked to the water seepage inside the soil medium.

The frequency content of the signal is shown in Figure 3-6C. Lines indicating high energy at 25, 50, 100, 150 and 200 Hz represent the electrical energy frequencies. High energy is observed below 25 Hz and seems to decrease and increase during the experiment. The energy in this band corresponds to the activity in the laboratory that decreases during the night time and increases again during the day. Energies are observed in the 160 – 190 Hz frequency band highlighted by a red rectangle in Figure 3-6C. This energy appears slightly after the initial increase in head (index 4) then seems to fade away up until it appears again at 30 h even though at this time no increase in head was made. This energy seems to originate from events in the soil or water flow since they are depicted in the night period as well. They do not exist at all times of the experiment and they stop and start abruptly. Strangely, they are not linked to the events shown in Figure 3-6B. However, they seem to be linked to the changes taking place in the soil medium because following the increase in the head (index 15) they seem to reappear until the end of the experiment.

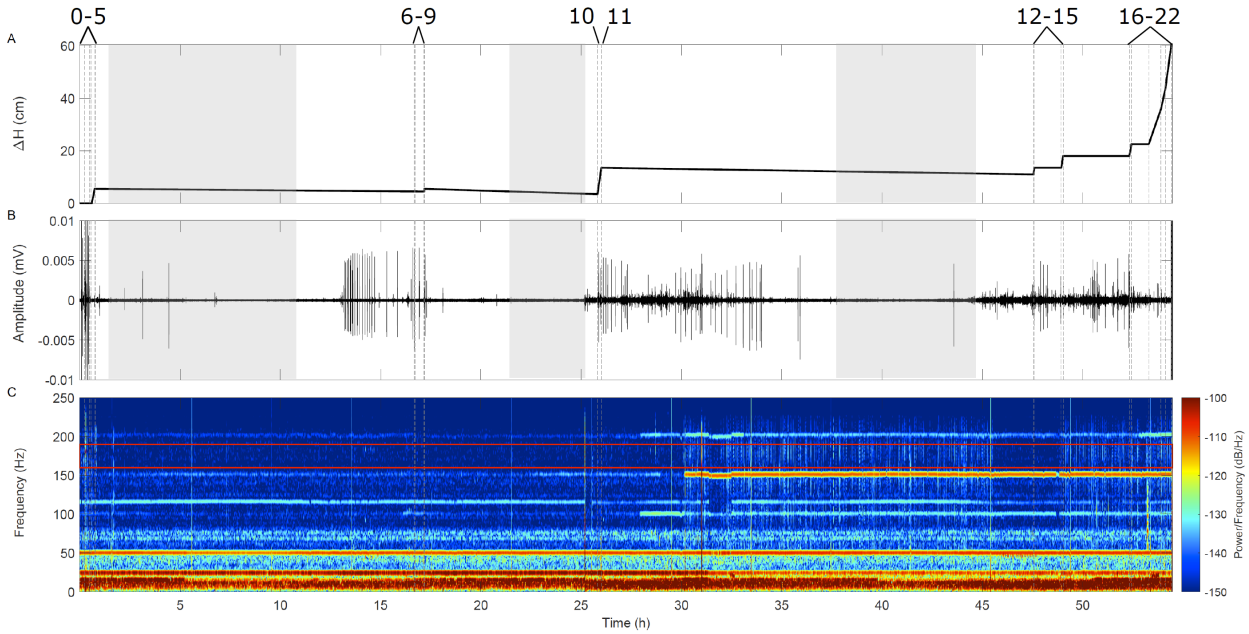

Figure 3-6: Seismic monitoring of the experiment: A- Corresponding ΔH with respect to the time of the experiment; B- Broadband time series; C- Corresponding spectrogram of the experiment. The grey dashed lines correspond to the indices defined in Figure 3-2 and Table 3-1: Summary of the experiment stages and the grey rectangles show phases of low activity (night time) next to the experimental setup.

3.2.3.5 160 – 190 Hz frequency band analysis

The frequency band of 160 – 190 Hz where the energy takes place in Figure 3-6C is exploited in Figure 3-7. For this purpose, the time series is filtered in this frequency band (160 – 190 Hz) with low activity periods shown in grey zones (Figure 3-7B) and the corresponding Energy Spectrum Density (PSD) is presented in (Figure 3-7C).

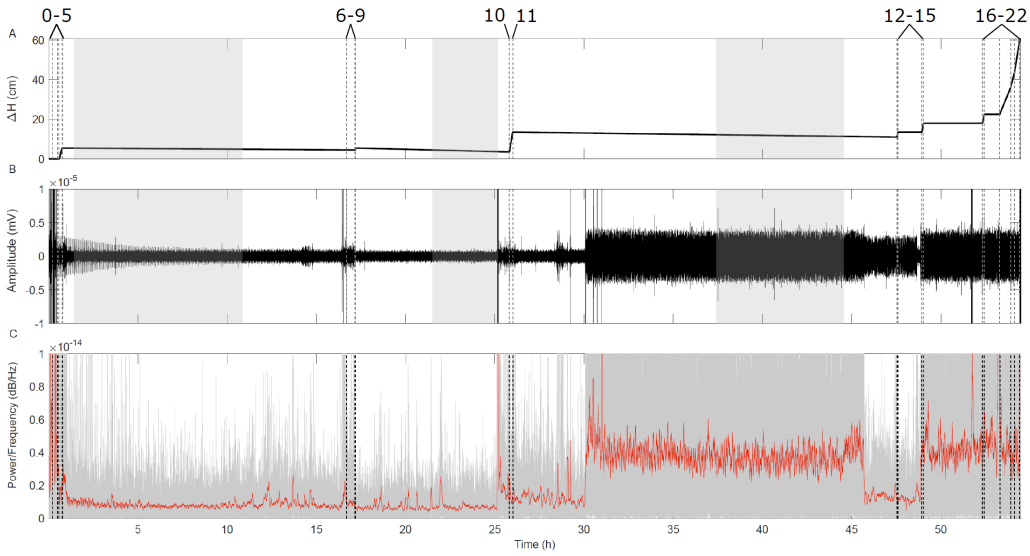

Figure 3-7: Seismic monitoring as a function of the head of water; A- Changes of the heads of water applied, B- Seismogam filtered between 160 and 190 Hz and C- the Energy Spectrum Density (PSD) as a function of time centered at a frequency of 170 Hz.

The seismogram in Figure 3-7B shows a series of events at the beginning of the experiment (first contact with the water, index 1) with a decrease in amplitude with time up to approximately 7 h. These events could be due to the water seepage in the soil medium especially that they are seen at night time as well. They seem to decrease gradually and become part of the surrounding noise with the decrease in water head presented in Figure 3-7A. Following that, few signals are depicted with amplitudes higher than the surrounding noise existing particularly during the day time which could be explained by the increase in activity in the laboratory. Events are spotted around 29 h that could be due to the activity around the experiment or changes in the soil matrix (could be a trigger) that is followed by a band of high amplitude that emerges after 3.5 h from the increase in head to ΔH = 13.5 cm (index 11). It lasts until 45 h when it stops abruptly. It is also existent during night time which probably shows that it is linked to the soil water interaction in the seepage zone. No changes are detected from 45 h until 49 h even though the head was increased again to 13.5 cm at 47.6 h (index 12-13). Following the increase in head to ΔH = 18 cm (index 18), the amplitude increases again up to the end of the experiment.

The PSD in Figure 3-7C centered at a frequency of 170 Hz reflects the energy content of the seismogram of Figure 3-7B. The energy seems to increase when the water was first introduced in the system (index 1) and then at the increase of ΔH to 5.5 cm (index 5). Following the increase in the energy with the increase in the head, the system goes back to a stable state at around 1 h. No changes are depicted during the night period and very few are detected during the day caused by the increase in activity around the experiment. At 30 h, the energy is noticed to highly increase with the appearance of the high amplitude band in Figure 3-7B. No changes were depicted visually which might imply that the sudden increase in energy is related to the modifications in the soil

structure that are taking place due to the increase in head. However, at 45 h, the energy decreases and following the further increases in heads (ΔH =13.5 cm – index 12) the energy remains low until ΔH = 18 cm (index 15) when the system seems to be reactivated again and higher energy is depicted until the end of the experiment.

3.2.3.6 Events analysis in the 160 – 190 Hz frequency band

The series of higher amplitude events observed in Figure 3-7B following the increase in heads of water applied are shown in close-ups in Figure 3-8. The water head ΔH and the seismogram filtered at a frequency band of 160-190 Hz are shown in Figure 3-8A and B, respectively. Figure 3-8C to F show the close-up (time windows of 6 min) on different stages of the experiment to compare the events that are seen with the changes in the heads. Moreover, another 45 s close up (represented by the red rectangle) is applied to highlight the resemblance of the events. Figure 3-8C to F are represented using the same amplitude scale with time windows of 6 min and 45 s to better compare the energy and duration respectively of the seismic events.

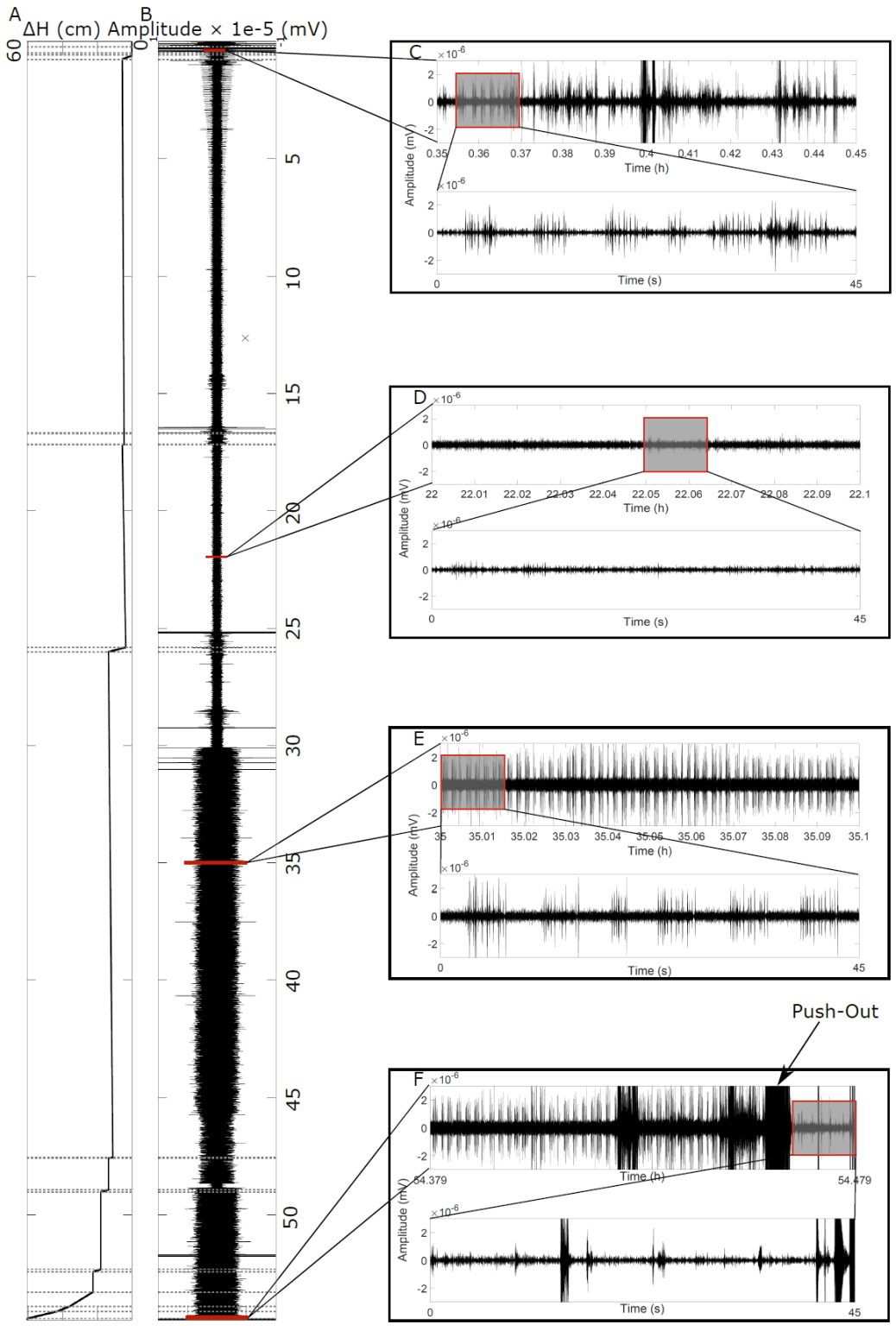

Figure 3-8 Identification of the events detected. A- Changes in the water head with time, B- Filtered seismogram in the 160-190 Hz frequency band showing red rectangles of a 6 min duration, C, D, E and F represent the close-up on the 6 min events identified during the water seepage including a 45 s close up window to represent the events observed; they are all represented in the same time and amplitude scales.

Figure 3-8C represents the time window between 0.35 and 0.36 h (which is the time of the first noticed events). It happens when the water was first introduced in the system. A series of events start taking place that looks erratic and not very regular. They appear before the water starts flowing downstream (index 5 at 0.77 h).

Figure 3-8D is a close-up between 22 and 22.1 h when the events seem to fade out in the seismogram. However, these events still exist but are of a very low amplitude (a bit higher than the surrounding noise originating from the activity in the laboratory) probably due to the decrease in water head.

Figure 3-8E shows the time period following the increase in head to $\Delta H = 13.5$ cm (index 11). The same family of events observed in Figure 3-8C are identified. However, they look more regular and more energetic.

Figure 3-8F shows the end of the experiment. The moment of the push out of the soil sample from the concrete beam is represented on the figure. It is noticed that prior to the failure, the events can be seen and following the push out of the soil sample, the events disappear which shows that the origin of these events is the water seepage inside in the soil sample.

3.2.3.7 Reference geophone analysis at 160 – 190 Hz frequency band

In order to check whether the events identified in Figure 3-8 originate from the surrounding activity in the laboratory a vertical geophone that was located next to the concrete beam was used as a reference to compare the results and identify activities taking place in the soil sample and not originating from human interaction. Figure 3-9A and B show the changes in ΔH and the seismogram of the reference geophone filtered at a frequency band of 160-190 Hz. The high amplitude observed at every change of head corresponds to the activity in the laboratory originating from footsteps next to the beam and water filling of the tank. However, following the increase in head, very few high amplitudes are depicted. Moreover, the events detected in Figure 3-8 are not identified in this geophone. Therefore, these events originate from the soil sample. Figure 3-9C does not illustrate the drop in energy that is observed in Figure 3-7C between 45 h and 49.5 h which rules out a malfunction in the equipment since the reference geophone exhibit an increase in energy due to the activity around the experimental setup.

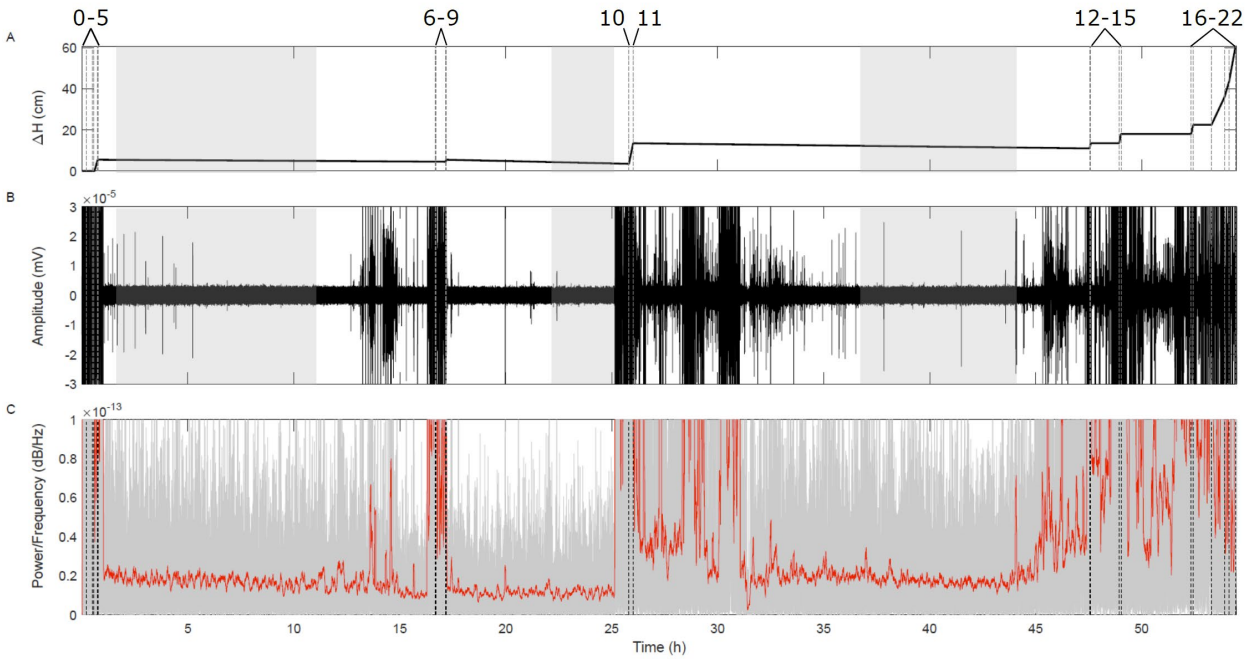

Figure 3-9 A- Changes in head with time and B- the filtered seismogram in the 160-190 band frequency of the vertical geophone placed as a reference next to the experimental setup

3.3 Interpretation and Discussion

Following the water being introduced in the experimental setup, water will infiltrate in the seepage zone (Figure 3-10A). This mechanism will lead to soil particles rearrangement, detachment from the soil matrix and pores between the soil particles will be replaced by water (Figure 3-10B). This mechanism allows the air bubbles to escape upwards through pores in the upper layers to finally settle at the surface between the soil and the concrete. Further increases in heads upstream will lead to further air bubbles exiting and settling between the soil and the concrete interface (Figure 3-10C).

Electrical resistivity monitoring showed changes in the weighted average data inside the seepage zone. At first, a decrease is depicted due to the water infiltration thus the increase in water content. However, following this decrease, an increase is noticed that is affected by the increase in the contact resistance between the electrodes and the concrete which was not continuously measured due to equipment restrictions. Following the increase in head, a decrease is depicted which is larger in the lower part of the seepage zone than in its upper (Figure 3-5 – index 10). That is due to the seepage path of water that reveals a higher water content zone at the bottom. Following the further increase in the head upstream, the electrical resistivity at the upper part shows an increase due to the additional entrapped air bubbles at the top and contrarily a further decrease on the lower part explained by the further increase of water content (details of the air bubbles at the top of the seepage zone is highlighted by a series of screenshots taken during an experiment conducted in a

pexiglass tube that aids in the visualization of the evolution of the experiment following water seepage – Appendix B).

Passive seismic monitoring shows changes in the energy level originating from the water seepage inside the soil sample. It is identified at a frequency band of 160 – 190 Hz. It is linked to the increase in head upstream thus resulting an increase in the flow leading to an increase in the energy of the seismic signal recorded. Signals detected following the water seepage explains the increase in energy observed throughout the experiment. They consist of a series of events that increase in amplitude and recurrency with the increase in head applied. Contrarily, with the decrease in head, they become less frequent and their amplitudes decrease to become at some point embedded in the surrounding noise. These events could originate from the saturation of the soil sample that would lead the air bubbles to escape to the upper part of the soil sample and settle in the upper soil layer (details in the snapshots in the figures in Appendix B), the impact of the seeping water on the soil pipe walls, the soil particles detachment as well as interparticle interaction (Lin et al., 2020; Lu & Wilson, 2012). Consequently, this would explain why they stop abruptly and do not initiate until the head is increased even more. The events are not depicted in the reference geophone which concludes that these events originate from the soil medium. Moreover, they disappear when the soil sample was pushed out of the concrete beam which causes the release of the air bubbles.

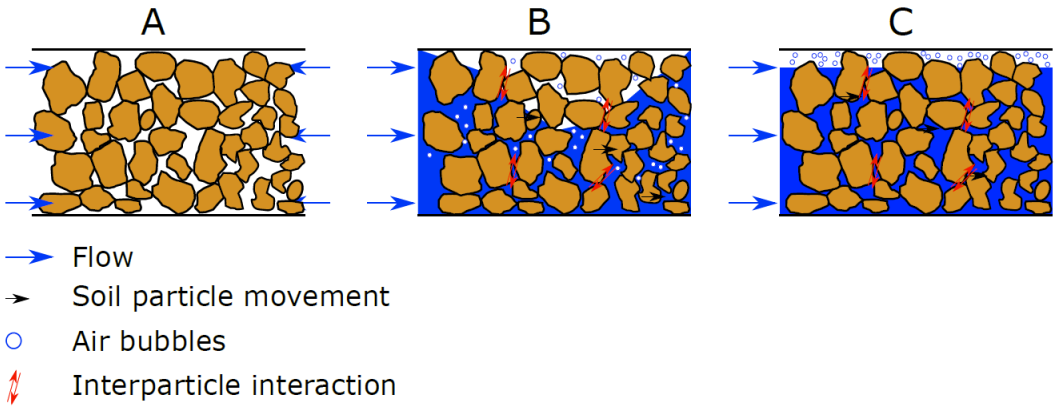

Figure 3-10 Schematic representation of the water flow inside the soil sample; A- represents the initial stage of the soil sample at OMC, B- is the saturation phase with the air bubbles moving upwards and the soil particles rearrangement and interparticle interaction and C- shows the entrapped air bubbles at the top of the soil sample.

3.4 Limitations

During this long experiment to monitor water seepage, various limitations were encountered in the setup. Keeping the fixed head was not possible because a pump was not installed. Moreover, the soil sample was pushed out of the concrete beam (forced to fail) and did not evolve to encounter the 4 stages of internal erosion and fail. In addition, the continuous measurements of the flow were not done which could have given a clear idea about the causes of the increase in energy when the water head was increased. Concerning the techniques used, the resistivimeter used did not acquire

contact resistances at each measurement which could have been used in the interpretation of the changes in electrical resistivity data.

3.5 Conclusions and Perspectives

The objective of this chapter was to detect and monitor water seepage in porous medium through a controlled laboratory setup and a continuous monitoring using electrical resistivity and seismic techniques. The use of electrical resistivity was hardly affected by the changes in water heads applied upstream. Even though variations were observed, but a correlation between the increase in head, increase in flow and changes in electrical resistivity data were not concluded.

Passive seismic listening was able to detect water seepage in the porous medium and its ability to quantify through events detected in the 160-190 Hz frequency band when water was introduced in the setup. These events originated from various changes inside the soil matrix such as re-arrangement of soil particles, air bubbles displacement and interparticle interaction. The cycles of activation and steady state of the system were detected as well as an increase in the energy of the seismic signal following the increase of head to be higher than the critical head for initiation of internal erosion. These results strongly support a complex and episodical process of water seepage and erosion with the presence of several phases of activation separated by more quiescent periods.

The techniques applied in the monitoring of water seepage were successful at the laboratory setup under controlled environment. The problems encountered during the experiment, such as malfunction in the resistivimeter and excessive activity next to the setup might have affected the results. However, the results presented the detection of a trend between the seismic energy and the increase in head thus the flow.

The setup used pave the way to implement similar monitoring techniques. First, on experimental dams in the field with more variables in question in order to verify whether same behaviors/cycles could be detected at larger scales. Second, additional experiments could be conducted where the full seepage and internal erosion stages are shown with the use of a setup that would lead to shorter durations to avoid any data corruption and contamination from students' activity and machineries in the laboratory. Third, it would be interesting to be able to classify the seismic events observed according to their origins. For example, a 3D printed porous medium that would replace the soil sample. With a similar setup, seismic energy originating from the water flow would be better characterized and differentiated from interparticle soil interaction caused by the seepage of water.

CHAPTER 4

INTERNAL EROSION IN POROUS MEDIA: GEOPHYSICAL MONITORING OF A LABORATORY SCALE EXPERIMENT

Following the results obtained in the laboratory setup to monitor seepage of water in porous media and the problems that were faced during the long experiment of water seepage, it was interesting to conduct a shorter experiment that would lead to internal erosion. For this purpose, changes in the soil properties were made to induce internal erosion in approximately 8 minutes leading to less activity interference in the laboratory and lower chances of equipment malfunction. The objective behind this experiment is to demonstrate the whole process of internal erosion starting by the simple seepage of water, followed by initiation of internal erosion, its continuation progression and finally the failure. The experiment was monitored using both electrical resistivity and seismic technique.

This chapter was submitted to the journal "Near Surface Geophysics" on July 24, 2021: ID: nsg-2021-2146 (REX-PROD-1-63775064-FE49-4B41-B33B-8F7600F7451D-C9BCA078-B8C7-4FCB-908D-3E4006050519)

Geophysical monitoring of a laboratory scale internal erosion experiment

Running title: geophysical monitoring of internal erosion

Yara Maalouf[a*], Grégory Bièvre[a], Christophe Voisin[a] and Naji Khoury[b]

[a] Univ. Grenoble Alpes, Univ. Savoie Mont-Blanc, CNRS, IRD, Univ. Gustave Eiffel, ISTerre, 38000 Grenoble, France

[b] Notre Dame University – Louaize, 72 Zouk Mikael, Lebanon

*Corresponding author: yara.maalouf@univ-grenoble-alpes.fr

Abstract

Earth dams are structures used worldwide for water management. Their failure over time is notably due to water seepage generating internal erosion. There is a growing need to detect the processes at work as early as possible. This study presents a controlled laboratory experiment aimed at detecting and monitoring the water seepage into a soil sample. The experiment was monitored with electrical resistivity tomography (ERT), velocimeters and video recording. The video recording of the downstream side of the soil sample shows successive episodes of mass movements associated with a progressive water flow increase. The ERT, limited by a low temporal resolution, shows an evolution of the resistivity in agreement with the evolution of the soil sample (e.g. saturation, mass movements) but with, however, strong limitations regarding the robustness of the results. The continuous seismic recording reveals extra rupture episodes that occur inside the volume of the soil sample, which was not recorded by the video. Their distribution in time and energy illustrates strongly nonlinear changes in the soil sample, with several phases of acceleration. A controlled source monitoring using external repetitive events allows probing the medium with an enhanced temporal resolution with respect to ERT. The apparent seismic velocity of the soil sample reveals a nonlinear decrease, high in the beginning of the experiment, and then stalled until the different mass movements enlarge the amount of water inside the sample along with the water flow. The different techniques used, especially seismic monitoring, describe a complex and strongly nonlinear process of internal erosion centred around the coupling between water flow and internal damage. Finally, these findings suggest that seismic methods could be able to distinguish the four different phases of internal erosion (namely, initiation, continuation, progression, and failure) discussed in the geotechnical literature.

Keywords: internal erosion, piping, laboratory experiment, seismic monitoring, electrical resistivity.

4.1 Introduction

Earth dams, such as levees, embankments and dykes have existed for centuries ago and are the most abundant types of dam in the world (Morales-Nápoles et al., 2014). The sudden failure and the subsequent massive release of water within a rapid timeframe (Fell et al., 2003) has caused massive losses in lives and lands throughout the years (Foster et al., 2000a; Silva Rotta et al., 2020). Based on the literature of dam failures and the register of dams stated in the International Commission on Large Dams database (ICOLD, 2001; 2017), 48% of failures of dams constructed between 1800 and 1986 resulted from overtopping, 6% were caused by static and seismic instability and, finally, 46% of worldwide dam failures resulted from internal erosion.

Internal erosion is defined as the process of soil particles movement from the core of the structure towards the downstream by seepage (Terzaghi et al., 1996). Statistical results showed that 31% of erosion failures were caused by piping through the embankment (Foster et al., 2000b, a) which is due to the excessive seepage of water and transport of soil particles until the formation of a pipe inside the body of the structure. Moreover, the results of the study conducted by Foster et al. (1998) indicate that about 1 in 200 dams failed due to piping and 1 in 60 experienced a piping incident. According to Foster and Fell (1999) and to Fell et al. (2015), internal erosion may develop through the embankment, the foundation, and also from the embankment into (or at) the foundation. The causes of degradation of dams vary but are mainly due to the fill material used, the increase in loading, the bad design of filters, or the improper selection of the embankment core materials.

The internal erosion and piping processes are described by different stages, the relative duration of which is unknown, as illustrated in figure 4-1. The first stage, called initiation, is either related to the development of a concentrated leak, suffusion, or backward erosion (Van Beek et al., 2013; ICOLD, 2017). The second stage of internal erosion is called continuation. In this stage, internal erosion can be stopped if the filters are properly designed to prevent the washout of fine materials; otherwise, internal erosion will proceed to stage 3, called progression (Foster et al., 2000a). It corresponds to the formation of a pipe in the body of the dam. Once the pipe is created, internal erosion process accelerates up to the failure (stage 4; Fell et al., 2003). The potential loss of lives caused by the failure of a dam relies mostly on

the warning time given to evacuate areas at risk at the downstream of the dam (Fell et al., 2003). For example, around 20 years ago, the United States Bureau of Reclamation recommended that the warning time of failure be of a minimum of 60 minutes in order to save lives (Graham, 1999). According to Fell et al. (2015), internal erosion is more likely to be detected in the advanced stages of progression and breach formation (i.e. late stage 3 and stage 4). Hence, it appears crucial to detect as early as possible an ongoing internal erosion process and identify its current stage (1,2 or 3).

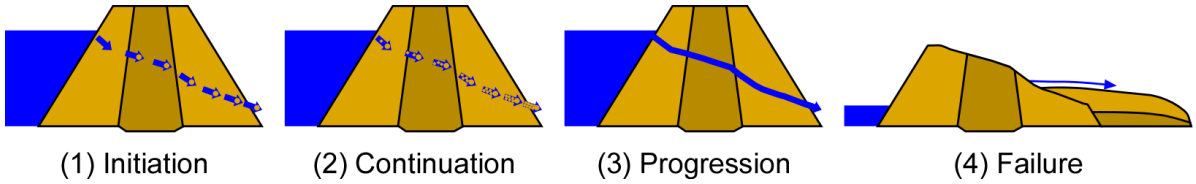

Figure 4-1: The different stages of internal erosion in the backward erosion type (modified from Fell et al., 2015). (1) Initiation, when the first soil particle is driven downstream. (2) Continuation, when additional soil particles are washed away. (3) Progression is the formation of the pipe in the embankment. (4) The breach represents the complete failure of a part of the dam and allows the water to flow out of the reservoir.

Fell and Fry (2007) proposed a three-step methodology to detect weak zones within earth dams. It consists of (1) non-destructive (among which geophysical) techniques to determine probable weak zones, (2) detailed (geophysical and geotechnical) investigation of the weak area to determine its state and (3) undergo geotechnical testing to determine physical properties of the soil. Beyond the identification of potential weak zones within these structures, geophysical techniques can be used to monitor their temporal evolution. Repetitive active measurements (e.g. time-lapse approach) have shown to be successful to detect and monitor leakage and seepage path, especially using Electrical Resistivity Tomography (ERT; Sjödahl et al., 2009; Weller et al., 2014). Monitoring of earth dams using active seismic methods has been poorly reported so far. These approaches require, however, periodic reinstallations of experimental setups in the field and provide only poorly-constrained temporal resolution (see discussion by Hirose et al., 2017). An alternative is to perform a continuous monitoring of the structure. This can be achieved using permanently installed devices, which have been mainly reported for ERT so far (Gunn et al., 2018). Continuous passive seismic recordings allow to monitor the structure and its evolution by detecting seismic events that reflect the changes and reorganizations of the internal structure. A study conducted by Rittgers et al. (2015) on the IJkdijk experimental field dam (Netherlands) showed the ability of self-potential combined with passive seismic monitoring to detect, localize and monitor changes in porous media. The acoustic events (AE) detected

in the passive seismic monitoring were isolated, arrival times were obtained and used to localize the source of these events in the dam. A geophysical study was conducted on a real dyke in France using, among others, seismic techniques (Bièvre et al., 2017). This study showed increases in seismic amplitudes recorded by a group of 4 geophones (over a spread of 24 located on the crest of the dyke) located above a seepage zone. The impulsive signals were also used to successfully locate at 3.4 m depth a 0.2-0.3 m-wide seepage zone within the dyke. After remediation works, no high amplitude nor impulsive signals were observed.

Additionally, seismic noise can be turned into a tool for monitoring seismic velocity variations at various scales (from the Earth's crust to laboratory experiment) through cross-correlation of successive time windows. As water affects the seismic wave velocity, the application of seismic noise interferometry to groundwater monitoring has been used to detect changes in water table (Voisin et al., 2016; Clements and Denolle, 2018; Garambois et al., 2019). Planès et al. (2016) reported the seismic monitoring of a 6 m-long and 0.6 m-high canal embankment made of silty sand. They introduced a 1.3 cm diameter metal rod in the embankment that was pulled out to initiate the piping process (i.e. the experiment started directly at internal erosion stage 3, namely progression; Figure 4-1). They recorded semi-continuously the ambient noise with 10 vertical geophones. Using seismic interferometry, they monitored a wave velocity drop of 20% and further interpreted it as originating from a structure modification associated to an increase of the water flow. Using the same methodology on a real site, Olivier at al. (2016) were able to detect velocity variations down to -2 % that they related to a local increase in water level in the dam.

The main objective of this work is to capture the complete process of internal erosion, from the generation of water seepage until failure. For this, a laboratory experiment was designed in which water is forced to pass into a cylindrical soil sample held into a concrete beam. The ability of 2D ERT to detect changes with this particular setup was first evaluated numerically. ERT and passive seismic monitoring data (event detection and correlation) were then processed and the obtained time-series are eventually interpreted in reference to internal erosion.

4.2 Materials and methods

Many laboratory experiments devoted to the study of internal erosion consist in building small-scale earth dams contained in tanks and encompassing artificial defects (Planes et al., 2016). However, in this configuration, water leakage may develop at the interface between the earth dam and the tank. These water leakages at the interfaces may be much more important than the one developing in the artificial weak zone. Furthermore, they prevent the detection of weak seismic signals that could correspond to early stages of internal erosion. To avoid this issue, it was then decided to force a constant head of water to flow only in a weak zone, made here of a cylindrical soil sample embedded into a concrete beam. The system was then left to evolve naturally from progressive saturation up to failure.

4.2.1 **Experimental setup**

The laboratory setup consists of a plexiglass tank for water storage, a concrete beam and a hose as schematized in figure 4-3. The plexiglass tank has a diameter of 0.5 m and a height of 1.25 m and serves as a water supply to the system. The beam shown in figure 4-3 consists of concrete mixed at a low water-to-cement ratio (0.53) to increase its strength. A cylindrical hole 0.1 m in diameter was intentionally left to insert the soil specimen. The tank is connected to the seepage zone in the concrete beam through a PVC pipe. A valve controls the water flow. Three cameras were also used to monitor the experiment (rate of 30 frames per second). One camera was placed on the tank to monitor the water level. The two others were placed apart from the soil sample (i.e. upstream and downstream) to timestamp the observed events.

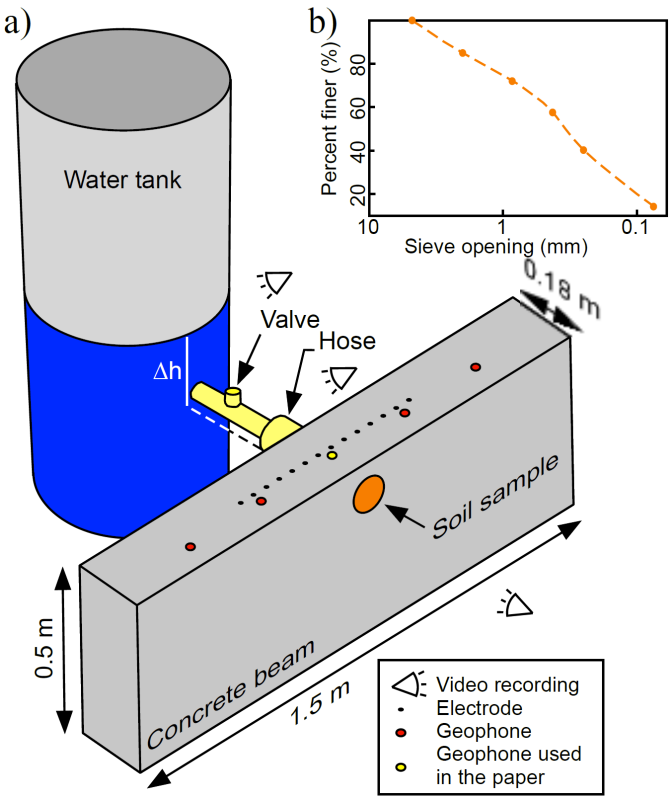

Figure 4-2: a) Laboratory setup of the seepage experiment. Δh represents the difference in water height between the water level in the tank and the bottom of the soil sample zone. b) The granulometric distribution of the soil sample is shown.

4.2.2 Geotechnical characteristics of the seepage zone

Soil erodibility controls the duration of any internal erosion test. The soil sample was devised as a mixture of sand and clay. A mixture of 65% sand and 35% of lean clay was chosen. The sand was passed through sieve no. 4 (4.75 mm opening). The sieve analysis was conducted according to international standard D6913 (ASTM, 2017). The granulometric distribution in figure 4-3 shows that the soil is a sandy clay with more than 50% retained on the 0.075 mm-opening sieve. The sample was mixed at the Optimum Moisture Content (OMC) of 11.3%. The Erosion Rate Index (ERI) of the soil sample was evaluated following the Hole Erosion Test (HET; Wan and Fell, 2004). It presents a value of 2, which corresponds to a very rapid erosion with a duration between initiation and failure lower than 3 h after Fell et al. (2003). The soil was then compacted inside the concrete beam, perpendicular to the flow (which is not the conventional compaction method with respect to the direction of the water flow in a

real earth dam; but it does not cause a problem during the experiment), in 5 layers of 400 g each using a wood piece to a height of 3.6 cm leading to a dry density of 13.49 kN/m^3.

Before the beginning of the experiment, the soil sample (prepared at its OMC of 11.3%) is not saturated with water. The experiment started by filling the tank with water at the desired height to reach the targeted hydraulic gradient. The valve was then opened to place the water in contact with the soil sample. From this time, the experiment evolved naturally without any external forcing. Under these experimental conditions, the time to failure of the soil sample is only controlled by the hydraulic gradient i (dimensionless) with respect to the critical hydraulic gradient i_c. Piping is initiated when i equals or is greater than i_c (Terzaghi et al., 1996). i is defined as:

$$i = \frac{\Delta h}{L}, \quad (1)$$

where Δh is the head difference of water between the upstream and the downstream (m) and L is the length of the soil specimen (0.18 m in the experiment). The critical hydraulic gradient i_c (dimensionless) reads as:

$$i_c = \frac{\gamma'}{\gamma_w} = \frac{G_s - 1}{1 + e}, \quad (2)$$

where γ is the submerged unit weight of soil (kN/m^3), γ_w is the unit weight of water (kN/m^3), G_s is the specific gravity and e is the void ratio (both dimensionless).

The specific gravity G_s was determined using standard D854 (ASTM, 2014) and was estimated to 2.66 ± 0.01. The void ratio was estimated to e = 0.93 ± 0.01, leading to a critical hydraulic gradient i_c of 0.86 ± 0.01. Given the length of the soil sample of 18 cm, the critical head H_c to be used to initiate internal erosion is 15.48 cm. A height of 15.5 cm was then chosen for the experiment. Given the large diameter of the water tank (50 cm), the hydraulic gradient is maintained slightly above the critical value throughout the experiment to insure the eventual failure of the soil sample. The latter is controlled primarily by the hydraulic gradient, but also by the soil compaction. Three preliminary feasibility tests were performed under the chosen experimental conditions and soil sample properties. They aimed at evaluating the time to failure, and the mode of failure (sudden or with intermediary mass movements). They showed times to failure between 5 and 10 min with an average of 7.6 ± 1.8 min.

4.2.3 **Electrical resistivity tomography**

Electrical resistivity represents the ability of a material to oppose the flow of electrical current. Apparent electrical resistivity is measured using a quadrupole with two current-injecting electrodes and two other electrodes to measure the induced voltage. The measured resistance R (Ω) is multiplied by a geometric factor K (m) to obtain the apparent electrical resistivity ρ_a (Ω.m). Fourteen electrodes were linearly spread with a regular spacing of 5 cm on the top of the concrete beam (Figure 2). The centre of this 0.65 m-long profile was positioned above the soil sample. Holes were drilled to a depth of 1 cm on the top of the concrete beam of the same diameter of the steel electrodes inserted (0.5 cm). Holes were filled with a salt water solution to decrease contact resistance as much as possible. Electrodes were connected to a single channel AGI SuperSting resistivimeter (Advanced Geosciences, Inc.).

A Dipole-Dipole (DDP) configuration array was chosen for the measurements. An average DDP sequence with 14 electrodes and a spacing multiplication factor interval up to 5 includes 74 direct measurements. Adapting delay and measurement times leads, with the device, to a duration of around 10 min for the whole sequence. after the feasability tests, the time to failure of the soil sample (around 8 min) required the definition of a resistivity measurement sequence much shorter than 10 min to get several sequences during the experiments gaining, however, sufficient resolution. This was achieved using the forward-modelling F3DM package (Clément and Moreau, 2016). Forward modelling was conducted using a methodology already applied to earth dykes (Bièvre et al., 2018). Succinctly, the 3D mesh was built with the Comsol Multiphysics software and resulted in around 23 000 tetrahedrons with a maximum volume of 1.5×10^{-4} m^3 in the concrete. The resistivity of the concrete and of the soil sample at its OMC was measured (500 and 300 Ω.m, respectively). These values were further used for forward computations, in order to use realistic parameters. Notably, the resistivity of the soil zone is representative of earth dams built in Lebanon. Since moderate resistivity variations are expected, only one configuration was used for forward computing, namely the concrete (500 Ω.m) and the soil zone at its optimum moisture content (300 Ω.m). Different configurations with reduced measurements were generated and computed using a trial-and-error approach. For a matter of time of acquisition, only direct measurements were considered. Considering the limited amount of measurements of the initial sequence (74), the reduction of measurements per sequence was conducted manually by keeping measurements, the location on the pseudo-section of which, was focused on the soil sample zone. The results were compared in terms of coverage with respect to the initial sequence made of 74 measurements (further referred to as the complete sequence). The optimized sequence

providing the highest coverage in the soil sample zone was eventually selected. Finally, it must be stressed out that the objective with ERT is not to image the soil zone but rather to monitor changes with time.

Measured apparent resistivity data were inverted using the BERT package (Günther et al., 2006; Rücker et al., 2006) with a custom 3D mesh made of around 17 500 tetrahedrons. The goal of inversion is to provide a 1D to 3D model depicting the spatial distribution of resistivity, and which explains satisfactorily the experimental apparent resistivity data. Although measurements were conducted in 2D, 3D inversion was preferred to take into account the particular geometry of the experiment with small dimensions and a finite domain. Variations of coupling between the electrodes and the concrete during experiments did not allow to consider a homogeneous resistivity for the concrete along the time-lapse experiment. Consequently, the resistivity of the concrete could not be set homogeneous during inversion. However, considering that most changes should occur in the soil sample zone, smoothness decoupling was used between the 2 zones (50 % decoupling). Time-lapse data were inverted using different strategies: individual inversion, and also ratio and difference inversion. The best results were obtained using the difference inversion (LaBrecque and Yang, 2001) using the model obtained with the initial dataset as a starting model for further inversions. Results were evaluated in terms of reconstruction of the resistivity distribution and of statistical results such as χ^2 and Relative Root Mean Square Error (RRMSE, in %). For analysing the evolution of resistivity, the averages were computed using individual weighting of each cell in the model in terms of volume and coverage (details in Bièvre et al., 2021).

4.2.4 **Seismic monitoring**

The preliminary intent of the seismic monitoring of the experiment is to reveal potential seismic activity related to either the water flow inside the soil sample, together with small cracks or seismic signals associated with grain rearrangements, mass movements, or failures. Seismic data were acquired using 5 vertical geophones of 4.5 Hz nominal frequency. The spacing between the geophones was 30 cm with the third geophone placed above the seepage zone (Figure 2). Data were acquired continuously during the experiment with a sampling frequency of 500 Hz. Since seismic velocities in concrete are elevated (P-wave velocity above 2000 m/s), information obtained by the 5 geophones showed to be redundant and only the results from the geophone placed above the soil zone will be further presented. A passive monitoring of the experiment was conducted by recording waves propagating inside the

experiment and detecting small seismic events. The acoustic emission introduced by Koerner et al. (1981) on dams consists on counting seismic events with amplitudes larger than a certain threshold. This has been used to monitor earth dams and to detect changes occurring inside the structure (Rittgers et al., 2015). In the present work, seismic signals were filtered in different frequency ranges and normalized to the maximum amplitude of a 5 min-long time window of the signal during the water flow in the soil sample. Following the normalization, different thresholds were set and the peaks exceeding the thresholds were cumulated and normalized by their maximum. These time-series were then compared to events detected in the video monitoring in order to identify the different stages of internal erosion.

Ambient seismic noise monitoring is a technique that consists of correlating seismograms of different geophones in order to identify relative changes in velocity (*dV/V*) and/or in the correlation coefficient (*cc*) of the waves. Ambient noise mainly consists of surface waves propagating in the presence of a free boundary, and the velocity of which depends on the frequency (Foti et al., 2018). The velocity of surface waves depends on the elastic property of the sub-surface, among which the shear-wave velocity is the main controlling property. Changes in velocity are related to changes in stiffness while changes in *cc* are related to geometrical or structural changes (Larose et al., 2015). However, considering the high velocity in the concrete with respect to the dimension of the experimental setup and to the sampling frequency, cross-correlation between couples of geophones eventually resembles auto-correlation. It was then chosen to auto-correlate signals recorded on the geophone located above the soil sample. Seismic signals were first cut in 2 s-long windows. They were then standardized (subtraction of the mean and normalization by the standard deviation of the 2 s-long samples) and further auto-correlated. Classical ambient seismic noise studies imply a spectral whitening of the seismic recordings to avoid the correlation to be dominated by a particular source. The cross correlation of successive time windows gives insight into the evolution of the Green's functions and of the changes in the medium. Contrarily to these studies (e.g. Planès et al., 2016), an active and repetitive source was introduced, under the form of a controlled leak located upstream. That source was energetic enough to be recorded by the geophones and, hence, to monitor the evolution of the experiment.

4.3 Results

A chronological framework of the geophysical measurements and of the visual observations is presented in figure 3. The time reference t = 0 coincides with the start of the seismic monitoring and will be the same throughout the following. The experiment started with ERT measurement ep01 at time t -3.5 min. Seismic monitoring started around 1 min before the end of ep01. At the end of ep01, the valve was opened and water started to flow into the soil sample. ep02 started at the same time (t = 1 min) and lasted around 4.5 min. Finally, ep03 lasted around 4.25 min and was acquired during the occurrence of collapses and/or slides (which will be further referred to as mass movements, MM) and, eventually, the complete failure. ep03 ended at time t = 9.75 min, which is around 1.25 min after the complete failure of the soil sample.

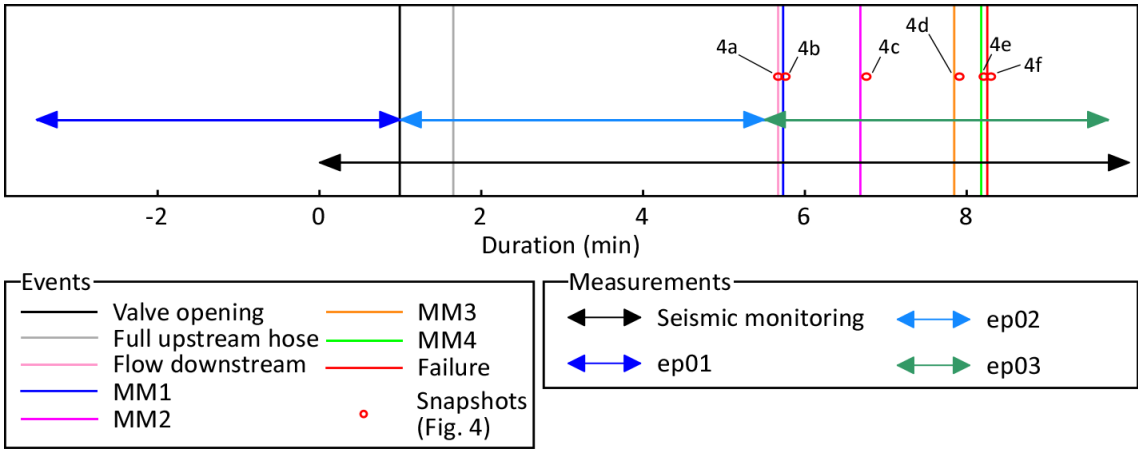

Figure 4-3: Chronological framework of the geophysical measurements along with the observed events. MM: mass movement.

4.3.1 Video monitoring

Figure 4 shows 6 different frames extracted from the video recorded downstream, taken at specific times. Snapshot a (Figure 4a) was taken at 5.67 min, when the first drop of water appeared downstream. At this time, the water pipe was established, although there was no measurable water flow. Snapshot b (Figure 4b) was taken at 5.76 min, just after the first mass movement (MM1) event that occurred from 5.7 min to 5.76 min and which is evidenced in the snapshot. There was no noticeable change in the water flow following this MM. Snapshot c (Figure 4c) was taken at 6.76 min, just after the second mass movement (MM2) event that

occurred from 6.61 min to 6.76 min and which is also visible in the snapshot. Once again, there was no noticeable change in the water flow following MM2. However, it showed a significant amount of mud, suggesting that the amount of water in the soil sample had increased with respect to the conditions at the time of MM1. Snapshot d (Figure 4d) was taken at time 7.91 min, just after MM3 that occurred from 7.78 min to 7.91 min (i.e. roughly 8 s of slow mass movement) and which is evidenced in the snapshot. Although a small quantity of water is visible in the image, again there was no noticeable change in the water flow following this mass movement. Snapshot in figure 4e was taken at time 8.21 min, just after MM4 that occurred from 8.15 min to 8.21 min (i.e. roughly 8 s of slow mass movement, with a progradation of the soil visible in the snapshot. At this time, an increase in the water flow was observed following this mass movement. Finally, snapshot f (Figure 4f) was taken at time 8.3 min, when the complete failure of the soil sample was reached, together with a free water flow. The 5.4 s duration between snapshots e and f suggests an acceleration of the erosion process towards the failure of the soil sample.

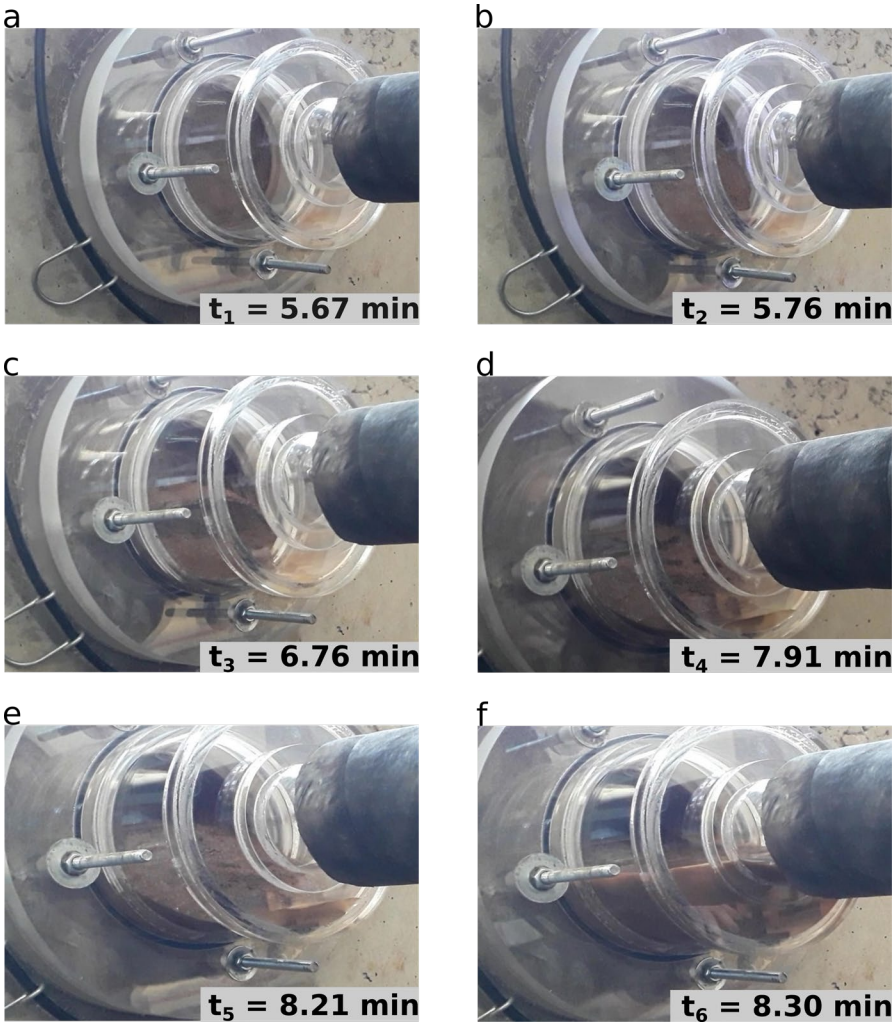

Figure 4-4: Captions taken from the video of the camera mounted downstream during the seepage of water in the soil sample. a) The water reaches the downstream. b), c), d) and e) Mass movements MM1 to MM4, respectively. f) Failure of the soil sample allowing water to flow freely. See Figure 3 for the location of the events on the timeframe.

4.3.2 Electrical resistivity imaging and monitoring

Figure 4-6a shows the mesh adopted for the inversion of synthetic and experimental measurements along with the location of the seepage zone and of the electrodes, and statistical results are detailed in **Table 4-1**. Figure 4-6b shows the resistivity distribution of the synthetic measurements with the complete sequence (74 measurements, above) and the optimized sequence (37 measurements, below). The image is a 2D slice extracted from the

3D volume and passing through the vertical plane defined by the location of the electrodes ("slice" in Figure 4-6a). Statistical results show that inversion converged toward satisfactory results after 4 iterations ($\chi^2 \approx$ 1-1.5 and RRMSE < 5 %). The examination of the figure shows that, considering the particular geometry of the experiment and of the 2D acquisition setup, the complete sequence provides a fair image of the studied structure along with, however, average resistivity (420 and 110 Ω.m in the concrete and in the soil, respectively; TableTable 4-2) different from the model (500 and 300 Ω.m in the concrete and in the soil, respectively). Furthermore, the limit between concrete and soil is not clearly located. Stronger decoupling between the two zones was tested. On one hand, it allowed to better distinguish these two zones. On the other hand, it led to unsatisfactory statistical results along with resistivity values far away from the model. It was then chosen to keep a decoupling of 50 % to get more realistic resistivity values. Compared to the complete sequence (real duration of around 8.5 min), the optimized sequence (real duration of around 4 min) provides a degraded image of the structure in terms of location of the soil zone. Furthermore, average resistivity values (230 and 160 Ω.m in the concrete and in the soil, respectively; Table Table 4-2) are also not in agreement with the model.

Figure 4-6c presents the coverage analysis. Coverage images of the complete and the optimized sequences appear fairly similar with the log scale. However, the relative difference between the optimized and complete sequences (bottom part of Figure 4-6c) reveals a global decrease, down to -50 % in the vicinity of the first electrodes along the profile. In the soil sample zone, this decrease is of around -15 % in the bottom part and decreases down to around -40 % in the upper part. This global decrease is not surprising considering the decrease of the number of experimental measurements by a factor of two. It suggests that other optimizing techniques could have been tested, such as the Compare R method, which aims at optimizing the resolution matrix (Wilkinson et al. 2006). It also suggests that, for such short-duration measurement sequences, multi-channel resistivity meters would prevent such strong decreases of sensitivity or resolution.

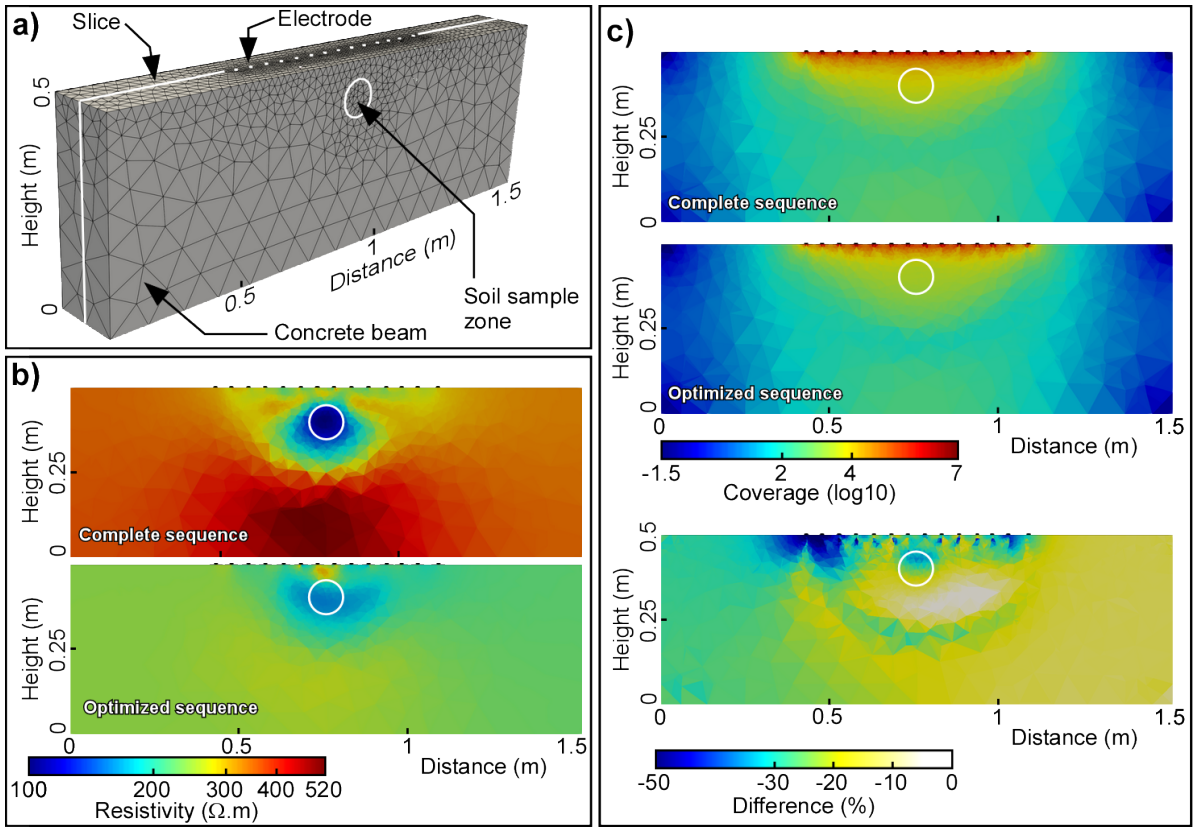

Figure 4-5: Synthetic results with the complete (74 measurements) and the optimized (37 measurements) sequences. a) The mesh used for inversion along with the location of the slice shown in Figs. 8b and 8c. b) Resistivity slices from the 3D models. c) Coverage slices from the 3D models along with the difference, expressed in percent, between the complete and optimized sequences. All slices pass through the vertical plane defined by the line of electrodes.

Table 4-1: Statistical results of synthetic and experimental inversions of electrical resistivity data. RRMSE: relative root mean square error.

Dataset	Iterations (#)	χ^2	RRMSE (%)
Synthetic computations			
74 measurements	4	1.5	3.7
37 measurements	4	1.2	3.4
Inversion of experimental data			
ep01	2	0.9	9.3
ep02	3	3.4	5
ep03	3	5	6

Table 4-2: Inversion results of the synthetic dataset. Resistivity of the concrete and of the soil sample in the numerical model were initially set to 500 and 300 Ω.m, respectively.

Synthetic dataset	Resistivity of the concrete (Ω.m)			Resistivity of the soil (Ω.m)		
	Min.	Max.	Average ± 1σ (volume and coverage-weighted)	Min.	Max.	Average ± 1σ (volume and coverage-weighted)
74 measurements	130	530	420 ± 25	100	120	110 ± 5
37 measurements	160	310	270 ± 60	150	190	160 ± 5

The results of the inversion of experimental resistivity are shown in Table 4-2 and Figure 4-7. Average contact resistances were of around 7200-7500 Ω (ep01 and ep02) and 9400 Ω (ep03). The first set of data representing the baseline before the opening of the valve is shown in Figure 4-7a. In agreement with synthetic results, the soil sample zone is very poorly detected with the optimized

sequence. The soil sample zone was further divided in two sub-zones, namely the upper and lower sub-zones (Figure 4-7a). Figure 4-7b presents the relative resistivity differences (expressed in percent) between, on the one hand, ep02 and ep01 and, on the other hand, ep03 and ep01. Profile ep02 was acquired when the valve was opened up until 4.5 min. This time corresponds to the water seepage in the soil sample and precedes time 5.67 min when the water reached the downstream, meaning that the sequence encompasses the major part of the saturation of the soil sample. The relative difference in figure 4-7b shows a global increase of resistivity in the beam in the low sensitivity zone. Then, strong decrease (down to -75%) and increase (up to 75%) of resistivity are observed between the electrodes. These are visible in Figure 4-7a for ep02 and ep03. These strong variations could originate from contact resistances, where the salt water injected before starting the experiment flowed in the concrete and did not allow to keep low contact resistance. Finally, figure 4-7b shows a decrease in electrical resistivity in the soil sample zone. It highlights the increase in water content of the sample and the partial saturation during the data acquisition time. The third data set ep03 is from 4.5 min until the failure of the soil sample. As shown in Figures 4-4 and 4-5, this duration corresponds to the time when the water reached the downstream and was followed by a series of mass movements leading to the failure. Figure 4-7c shows the evolution of the average resistivity of the 2 sub-zones. For both sub-zones, it decreases between ep02 and ep01 (-7%). This could correspond to the higher water content in the soil sample accompanying its saturation. Between ep03 and ep02, resistivity increases by ~3.5% and 15% for the lower and upper sub-zones, respectively. This increase could be linked to the collapse of the soil identified in the video snapshots (Figs. 4-5b to 4-5f) that induced the replacement of soil particles by air. However, and even if these results fit the observations, large error bars suggest that these variations are poorly significant from a statistical point of view. The discrimination between lower and upper zones also appears poorly significant from the same statistical point of view.

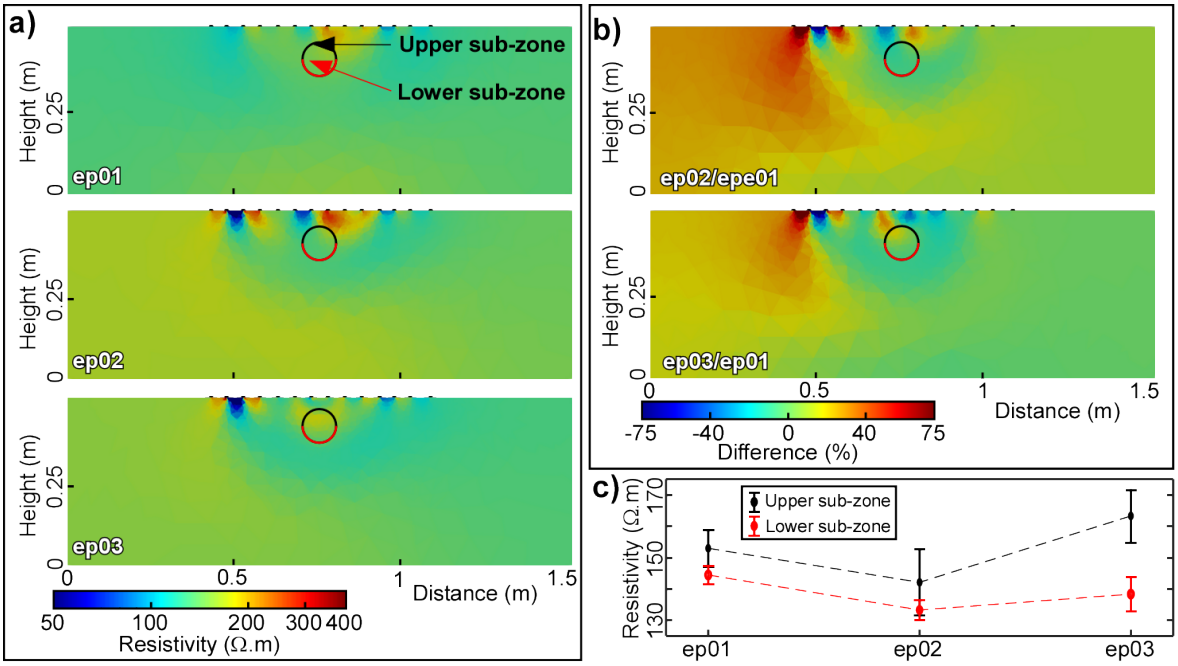

Figure 4-6: Experimental electrical resistivity tomography results. a) Tomographic images for measurements ep01 to ep03 from top to bottom, respectively. b) Resistivity difference of tomograms ep02 and ep03 with respect to ep01. c) Evolution of the average resistivity of the upper (in black) and lower (in red) sub-zone. Error bars correspond to the standard deviation. These sub-zones are indicated in Figure 6a.

4.3.3 Seismic monitoring

Figure 4-8 presents the passive seismic recording of geophone 3 located above the soil sample zone. Figures 4-8a and 4-8b present the unfiltered seismogram and the corresponding time-frequency representation, respectively. The latter shows successive sequences representing the main events happening during the experiment. The time period before the opening of the valve gives an insight of the background seismic noise. High amplitude signals are then observed from around 1 to 1.5 min and correspond to the slow and progressive opening of the valve. Starting from 1.5 min and up to 7.78 min, the seismogram is formed by seismic waves very similar to the background noise. The first visible mass movement (MM1) captured by the video occurred at a time of 5.76 min. It is not associated to a clear seismic event. On the contrary, MM2 is associated to a small amplitude seismic event, that would have gone unnoticed without the associated video recording. Finally, three other high-amplitude events are observed, namely two mass movements (MM3 and MM4) and the eventual failure, with amplitudes clearly above the background level. Several seismic events were also observed, which are associated with stronger amplitudes but not with observed events. The strong similarity of these events with what is measured before the beginning of the experiment makes it difficult to associate the seismic events with the water flow

or with any rupture occurring inside the soil sample. A possible way to discriminate what is related to the environment of the experiment from what is truly related to the physics of the experiment is to decompose the seismic signal in its different components. Figure 4-8b presents the spectrogram of the seismogram up to 250 Hz (the Nyquist frequency). In this time versus frequency representation of the seismic signal, it is easier to identify the prominent features of the experiment. At the first glance, the most energetic and dominant feature of the spectrogram is the valve opening phase, that radiates mostly in the lower frequency range (0-50 Hz) and includes impulsive events that radiate up to the Nyquist frequency. The continuous energy in the 25, 50, 75, 100 Hz and so on are related to the electrical power supply. The rupture and slow mass movements identified with the video recording have a seismic signature that is sometimes hardly visible in Figure 4-8b. MM1 is not recorded, possibly because of a very slow motion that does not radiate seismic energy. On the contrary, event MM2 is marked by a large seismic energy release visible at all frequencies. MM3 is associated to a small amplitude and long duration of the seismic signal, recorded mostly in the low frequency range. Interestingly, the seismic signal started significantly before the video recording of the mass movement. A similar seismic signature is observed for MM4, a few seconds before the final failure that radiates throughout the entire frequency range.

At frequencies from 80 to 120 Hz, the spectrogram is dominated by repetitive high energy events observed during the water seepage stage starting at around 1.5 min until the collapse of the soil sample. These events that do not appear in the baseline data are related to the water leakage at the upstream hose. Each droplet of water triggers a seismic wavefield that was recorded by all the geophones (see below for details). These external and repetitive seismic events were used as an active seismic source to investigate the soil sample and its evolution (see below). Finally, the spectrogram shows seismic events in the 150-250 Hz band that seem to be more numerous as the soil sample reaches the time of failure, suggesting that some of the events have to be related to the physics of the experiment.

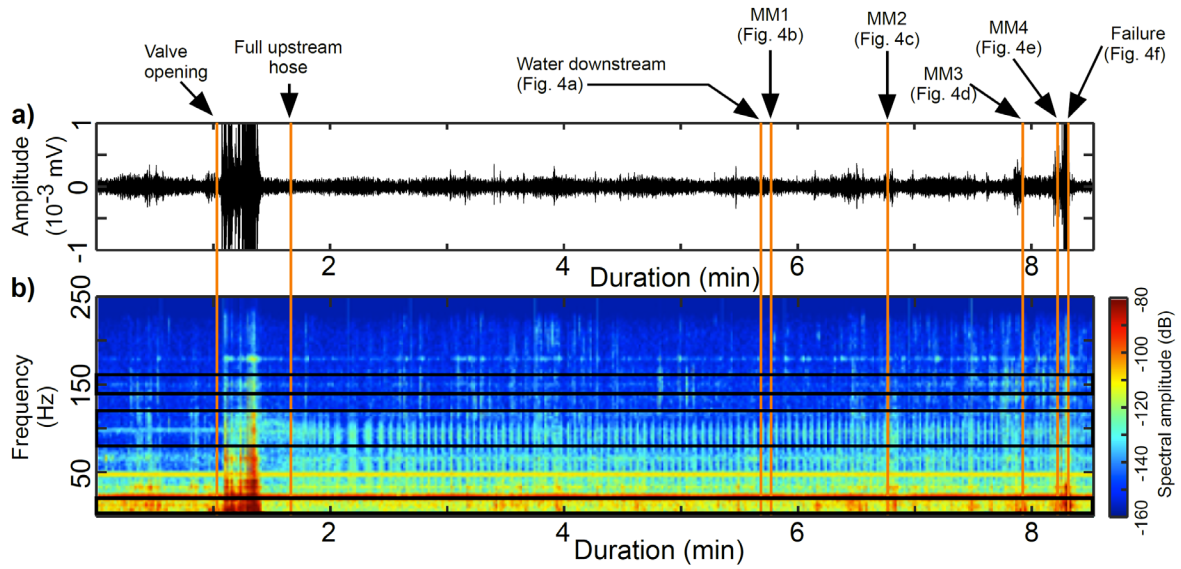

Figure 4-7: Seismic recordings of geophone 3 located above the soil sample zone. a) Time series showing the main seismic events. Arrows and orange lines delimit the different phases of the experiment (valve opening, full upstream hose, water downstream, mass movements MM1 to MM4 and failure with references to the video snapshots of Figure 4. b) Time versus frequency analysis of the seismic recordings presented in Fig 7a. The black rectangles show the three frequency ranges that are further analysed: 140 – 160 Hz, 80 – 120 Hz and 5 – 20 Hz

In order to confirm this apparent acceleration of the number of seismic events as the experiment approaches the failure, it was decided to monitor their dynamics by counting them. Figure 4-9 presents the band-passed filtered seismic data in the three frequency bands of interest defined previously from the analysis of the spectrogram: 140-160 Hz (Figure 4-9a), 80-120 Hz (Figure 4-9c), and 5-20 Hz (Figure 4-9e). The associated right panels (Figs. 4-9b, 4-9d and 4-9f, respectively) show the normalized cumulative number of seismic events detected in the seismic time-series and classified by classes of amplitude. In each frequency band, the amplitude of an event was defined with respect to the strongest event of the frequency band. This normalization reveals that the strongest event of each frequency band is associated to the final failure occurring at the end of the experiment. Then, in each class of amplitude, the cumulative number of events was normalized to the total number of events of the class. This two steps normalization allows to compare the dynamics of the experiment in the different frequency bands. Four amplitude classes were established in order to differentiate the dynamics of the experiment: 1) small events between 0.1 and 0.4 represented by the grey curve, 2) events between 0.4 and 0.6 represented by the blue curve, 3) events between 0.6 and 0.8 represented by the green curve and, finally, 4) events larger than 0.8 represented by the red curve.

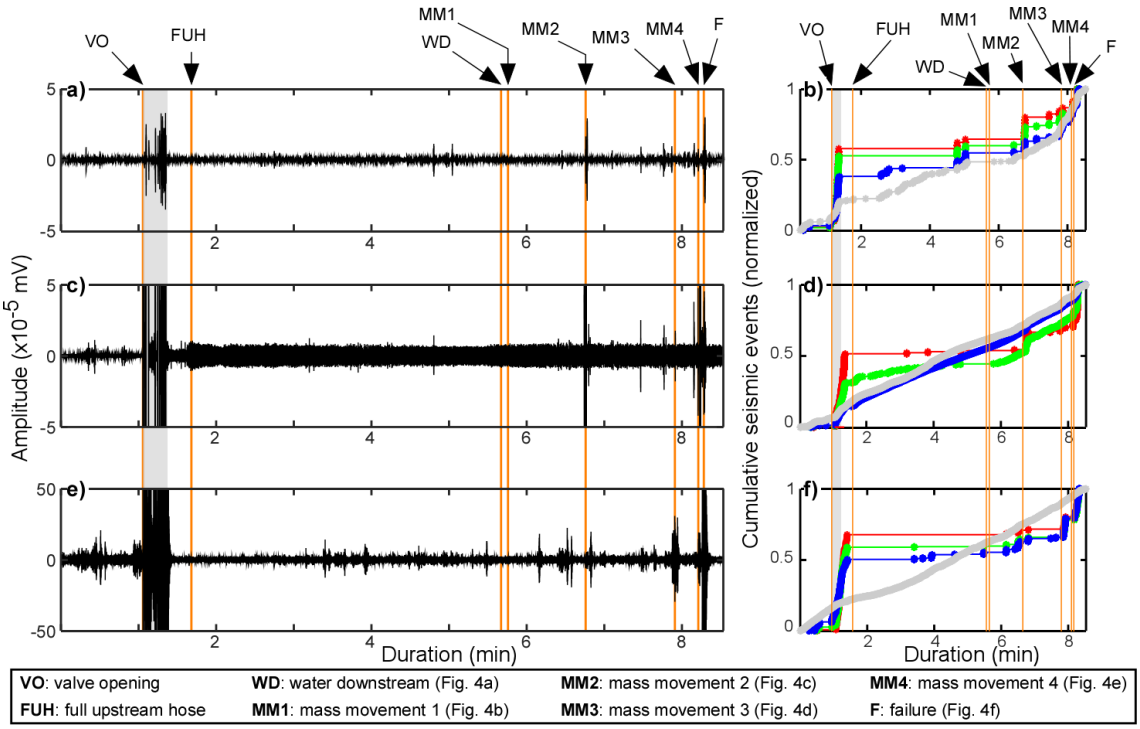

Figure 4-8: a), c) and e) seismic record of geophone 3 filtered in the 140-160, 80-120 and 5-20 Hz frequency range, respectively. Vertical orange lines indicate the different phases of the experiment (details at the bottom of the figure). The grey stripe corresponds to water movements in the tank following valve opening. b), d) and f) Cumulative number of events per class of amplitude normalized to the strongest event. Grey: normalized amplitudes between 0.1 and 0.4; blue: normalized amplitudes between 0.4 and 0.6; green: normalized amplitudes between 0.6 and 0.8; red: normalized amplitudes between 0.8 and 1.

Figures 4-9a and 4-9b present the seismograms and the cumulative number of seismic events, respectively, in the frequency range 140-160 Hz. Figure 4-9a shows that besides the period of valve opening, most of the seismic events (with large amplitude) occur at the time of MM2 and after. Small amplitude seismic events are visible from 2 to 4 min. One stronger series of events is recorded around time 5 min. Some of these events could be related to environmental noise and, if so, their occurrence should follow a random pattern. Figure 4-9b shows that for all classes of seismic detections the pattern is not random at all. Not considering the period of valve opening, the first three minutes reveal events with small amplitudes: the grey curve increases continuously and rather slowly. Slightly before 3 min, blue class seismic events are detected and the rate of grey class events suddenly increases. A similar sequence occurs at 5 min, with detections in all the classes. It suggests that a large event occurred within the soil sample which was not captured by video recording. Then, the system remains extremely quiet with no detection in this band until time 6.5 min, despite the occurrence of MM1 within that period. With the water appearing downstream starts a new sequence of small grey class events at first, rapidly followed by blue and green seismic detection and a major cluster of strong events corresponding to MM2. Contrarily to the first sequence, the rate of small grey class events is sustained and even increases slightly before

MM3 (7.78 to 7.91 min). Similarly the rate of blue, green and red classes increase until the final failure of the soil sample. The changes of rate detection observed for the different classes of events strongly suggests that most of the detections of seismic events in the 140-160 Hz frequency band are related to the physics of the soil sample evolution rather than to environmental noise. These detections suggest that the evolution of the soil sample is complex with at least one unrecorded seismic sequence at time slightly before 5 min. This is followed by events MM1 to MM4 and, eventually, the complete failure, all time-stamped using video recording. These events show both an increase in the rate of detection and an increase in the amplitude of the events.

Figure 4-9c presents the seismogram in the 80-120 Hz frequency band. It is dominated by a small amplitude but sustained seismic activity throughout the duration of the experiment. Some stronger seismic events are visible that correspond to the unrecorded seismic sequence occurring before 5 min (see above), event MM2 and a short period preceding the failure. The small amplitude and sustained activity that dominates the record is formed by repetitions of very short duration events that will be discussed further. Figure 4-9d presents the cumulative number of detections per class of amplitude. The grey and blue curves are particularly linear, despite some deviations at the valve opening and during some mass movements. This linear behaviour suggests, first, a nearly constant detection rate and, second, that the seismic events correspond to a background noise added to the signals. These classes of detections are much less sensitive to the soil sample evolution. Nonetheless, they will be further used to perform an independent monitoring of the evolution of the soil sample. On the contrary, green and red classes (intermediate and strong events, respectively) obey a different evolution. Shortly after the end of the valve opening phase, the number of detections in the red class is zero before increasing very weakly until event MM2. The rate of detection in the green class is slowly decreasing until the moment where water is observed downstream (5.67 min) along with event MM1 (between 5.7 and 5.76 min), where the rate increased suddenly. The occurrence of the second event MM2 (from 6.61 to 6.76 min) generated a bunch of strong and intermediate seismic events that are also recorded in the 140-160 Hz frequency band. Interestingly the green class shows a sustained rate that accelerates with the occurrence of the last sequences of events MM3 (7.78 to 7.91 min) and MM4 (8.15 to 8.21 min) before the failure (8.3 min).

Figure 4-9e presents the record of the seismic activity filtered in the 5-20 Hz frequency range. The background seismic noise is important because it captures the steps of the experimentalists before valve opening. Shortly after, the seismic signal is of low amplitude, with barely no strong events. The situation changes at 3 min, with the first stronger events occurring. Some of them are apparently not related to the macroscopic events recorded by the video or detected in the 140-160 Hz band. Figure 4-9f presents the cumulative number of detections per class of amplitude. The grey curve shows a nearly linear behaviour, suggesting again that these small amplitude events are

related to the seismic background noise. On the contrary, the blue green and red curves show behaviours that are strongly non-linear. The blue curve shows the first detection shortly after 3 min, rapidly followed by the green curve. Only very few events occur in these classes, and none in the red class. Changes are observed between 6 and 7 min (i.e. between MM1 and MM2), with an increase in detection rate in blue, green and red classes. Interestingly the detections precede event MM1, and stop at the time of event MM2. Then, the curves increase again shortly before events MM3, MM3 and, eventually, the final failure.

The repetitive, short-duration events shown in figure 4-9c (grey and blue curves) are illustrated in figure 4-10. The seismogram shows impulsive events (duration of around 0.1 s) occurring at intervals Dt of around 0.5 s at this moment of the experiment. These are the records of a leakage that appeared at the upstream side of the experiment and which regularly generated water drops each 0.5 s. This *a priori* superimposed noise was used as an active seismic source. It will be further used to illustrate the changes in time required for a wavefront to scan the experimental setup (i.e. the beam and the soil sample).

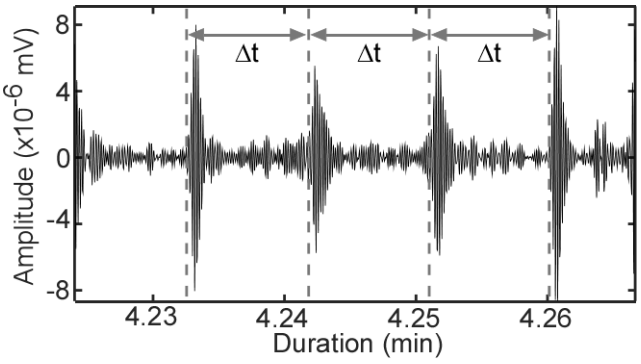

Figure 4-9: Impulsive, short-duration (around 0.1 s) seismic events generated each ~0.5 s (Dt) by a water leakage at the upstream part of the experiment and which was used as a seismic source to investigate the soil sample. The total duration shown in the figure is around 2.56 s.

The wave created by this source passes through the concrete beam and the soil sample. Any change in the medium (i.e. in the soil sample, since no change occur in the concrete) should lead to a change in the arrival time of the seismic wave. Therefore, a correlogram was computed from the autocorrelation of successive 2 s-long seismograms of geophone 3 placed on top of the seepage zone and filtered in the frequency range 80-120 Hz. Results are presented in figure 4-11a under the form of the evolution of time lags as a function of the duration of the experiment and with correlation coefficients *cc* represented by a colour scale. For the sake of visibility, this colour scale was intentionally limited to values ranging between -0.2 and 0.2. Before the valve opening (and the occurrence of water drop), no clear event is visible. After the valve opening, 4 main events are detected. The first one consists of the autocorrelation with its highest correlation coefficient at zero

lag. Three further events are observed at average lags of around 0.5, 1 and 1.5 s with, however, time lags that tend to increase non-linearly as a function of the duration of the experiment. These three further events were extracted from figure 4-11a and are presented in figure 4-11b. The 3 curves show the same trends during the experiment. First, from 1.65 min to around 3 min, there is an increase in the arrival times (and, hence, a decrease of the apparent velocity). This is interpreted as originating from the progressive infill of water into the soil specimen, leading to a change in its structure and the subsequent rearrangement of soil particles. It is noticeable that the slopes of the 3 curves are not identical (this is more visible in Figure 4-11b). This is caused by the autocorrelation process itself, where the correlation of increasing arrival times (caused by the multiple probing of the medium by the same wave) leads to progressively increasing time lags. This also explains the decrease of the correlation coefficient with the increase of the lag time as illustrated in figure 4-11b (with genuine *cc* values): for later arrivals, the wavefront scanned the medium several times and its similarity with the first one is degraded.Second, there is a slow increase of arrival times during the water seepage stage up to the moment when water appears at the downstream. Third, as water appears downstream at 5.67 min, followed by mass movement MM1 at 5.76 min, there is a small increase of the time lag starting from 6 min. Fourth and finally, further increases of the time lag took place which are related to the different mass movement events and the final failure. Interestingly, the increase in the time lag appears to be controlled by the different stages of this experiment that are detected in the video monitoring. This simple measure of autocorrelation reflects the changes of water content of the soil sample and the structural changes induced by the mass movements. The only varying portion of the experiment is the soil sample. It is then considered here that the concrete beam is poorly altered and interacts very little with the water.

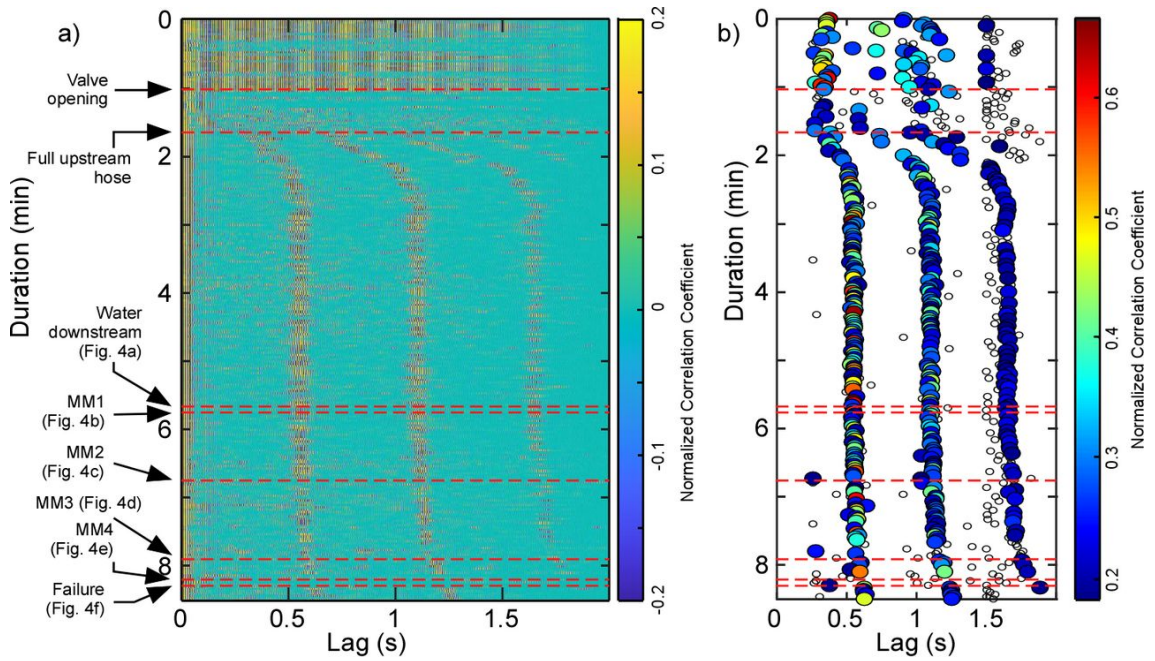

Figure 4-10: Autocorrelation of seismic time-series recorded by geophone 3 located immediately above the soil sample zone and filtered between 80 and 120 Hz. a) Causal part of the autocorrelation (the acausal part is symmetric). b) Maximum *cc* values of each autocorrelation. *cc* values below 0.18 were discarded and are represented by small white-filled circles. Monitored and observed events are indicated by red dashed lines.

4.4 Interpretation and discussion

Using the snapshots from the video, four stages can be identified and related to internal erosion. First, the initiation phase could be represented by the initial movement of the soil particles as shown in figure 4-5b with the first mass movement MM1 occurring at 5.76 min, immediately after a water flow was observed downstream (Figure 4-5a). This time could indicate the end of the initiation phase. Second, the continuation stage starts immediately after, with additional mass movements MM2 (Figure 4-5c) and MM3 (Figure 4-5d) until 8.21 min. Third, starting from this time, an increased flow of water was observed along with mass movement MM4 (Figure 4-5e), suggesting the beginning of the progression phase where the pipe was fully developed. Fourth, failure was observed at the end of the experiment (Figure 4-5f).

The electrical resistivity tomography time-series (Figure 4-7c) show a decrease in resistivity between ep02 and ep01. This can originate from the increase in water content of the soil sample following the opening of the valve. Then ep03 shows a global increase in resistivity compared to

ep01 and ep02. This can be related to the occurrence of the different mass movements MM1 to MM4 and of the final failure, leading to the replacement of soil particles by air in the sample zone. The global evolution of resistivity then appears to be in agreement with the observed events and suggests that electrical resistivity could be suitable to monitor internal erosion experiments in the laboratory. However, the measures conducted in this work show several and strong limitations. First, and due to the short time of the experiment, the single-channel resistivity meter used here is not adapted, even if it was attempted to optimize the measuring sequence using numerical modelling (Figure 4-6). In other words, several physical changes occurred during one measurement sequence. Consequently, a single ERT image encompasses several events that occurred in the soil sample zone and the device used here is not able to capture the rapid evolution of the experiment. This effect, called temporal smear has been investigated both numerically and experimentally by Rucker (2014). Second, and even if resistivity variations appear in agreement with the physical evolution observed along the experiment, the error bars associated to the data suggest that it is difficult to state whether resistivity variations are statistically significant. Several solutions can help to overcome these issues. Modern commercial resistivity meters allow multi-channel measurements (e.g. 10 to 12 channels for the most common recent devices). This could have allowed to use more electrodes in order to obtain a better reconstruction of the resistivity distribution, along with faster measurement sequences. Another solution would be the use of flexible, low-cost devices, especially dedicated to laboratory experiments such as the OhmPi resistivimeter (Clément et al., 2020). Finally, other optimization methods (e.g. optimizing the resolution matrix; Wilkinson et al. 2006) could be tested and compared to the results originating from the optimization of the sensitivity matrix. As a conclusion for resistivity in this experiment, the method could not indicate any additional information to what was already known from visual observation concerning the internal erosion in the soil sample.

On the contrary, the continuous monitoring using passive seismic recordings permits to interpret the evolution of the soil structure during the different stages of internal erosion, where no visual evidence was granted. The main events that were observed during the video monitoring were detected in the seismic signals in addition to multiple events preceding and following each snapshot. These events represent changes inside the structure of the soil sample such as the rearrangement of soil particles, the transport of soil particles and small mass movements that were not identified in the video. The curve of the cumulative seismic events in figure 4-9d (frequency range 80-120 Hz and thresholds between 0.6 and 0.8 represented by the green curve) was selected to illustrate that changes in the slope of the curve (detailed description in section 4.3.3) highlight the changes corresponding to the different phases of internal erosion: 1) at 5.76 min where the initiation phase ends and the continuation phase starts; 2) at 6.76 min where high amplitude events highlighted by a jump take place indicating the end of the continuation and the start of the progression phase; 3) at 8.21 min, another jump takes place suggesting the end of the progression phase and the start of the breach which is represented by high amplitude events denoting the failure

of the sample. The autocorrelogram shown in figure 4-11 also shows the changes in slopes that highlight as well the 4 stages of internal erosion: 1) a change in slope is observed at 5.76 min indicating the end of the initiation phase and the start of the continuation phase as indicated in the snapshots taken in figure 4-5b; 2) at around 7.5 min, highlighting the end of the continuation phase and the start of the progression phase; 3) at 8.30 min, the end of the progression phase and the start of the breach.

Figure 4-12 summarizes the seismic activity in the soil sample and its relation to the different stages of internal erosion (i.e. initiation, continuation, progression and failure). The cumulative seismic events (black curve) corresponds to the curve described above (frequency range 80-120 Hz and amplitude between 0.6 and 0.8 in Figure 4-9d) where the part before 2 min was removed. The autocorrelation curve (red curve) corresponds to the time lag greater than 1.5 s in figure 4-11b. It was chosen because it shows more pronounced slope changes. Also, the time lag, proportional to the apparent seismic velocity (the greater the lag, the lower the velocity and vice-versa) was expressed in terms of slowness (the inverse of the velocity) to present a trend similar to the cumulative number of seismic events. Once again, observations before 2 min were removed to highlight phenomenon corresponding to the evolution of soil sample during erosion only. The two super-imposed curves reveal globally similar trends with slope breaks corresponding to the identified stages of internal erosion. Changes in slope for both curves were analysed to better delineate transition zones and it must be stressed out that slope breaks are less pronounced on the slowness curve than on the seismic events curve, notably at time t = 6 min. This can originate from high velocity in the concrete, which tends to smooth velocity changes evaluated from the auto-correlation. Experiments on more realistic structures made of soil only, and using both auto- and cross-correlation, might provide sharper changes as a function of the development of internal erosion. This also suggests that the evolution from one stage to the other has to be considered as a progressive transition rather than an abrupt change. The change from continuation to progression shows, however, a slight discrepancy between the two geophysical parameters. Nevertheless, the two parameters are in good agreement and suggest they are both suitable to detect changes in soil samples subject to internal erosion in a laboratory experiment. Moreover, it appears that in this experiment seismic monitoring allows the detection of early stages of internal erosion, namely initiation and continuation.

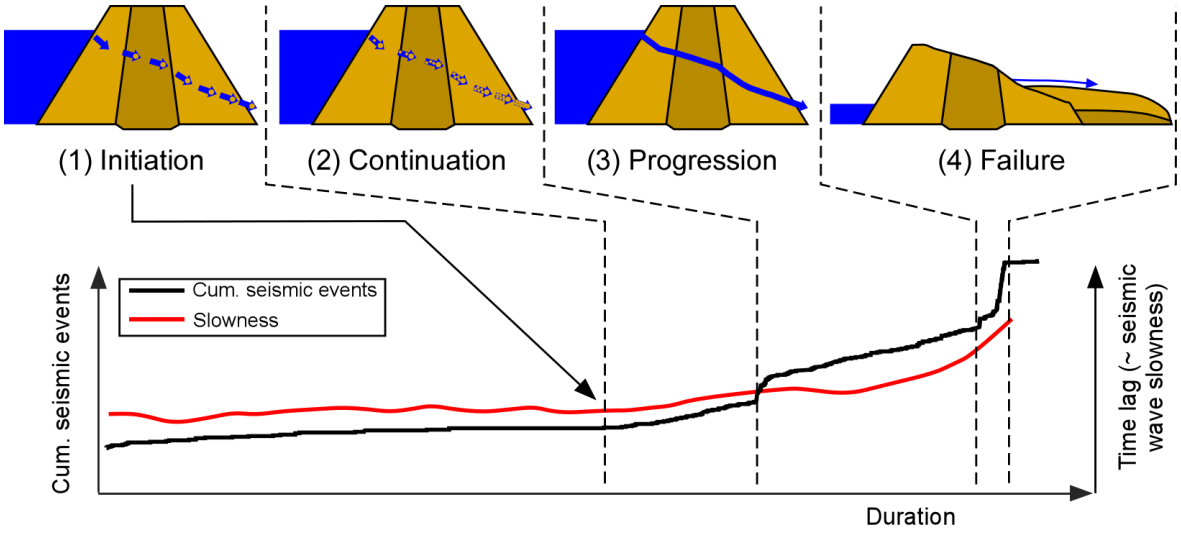

Figure 4-11: The different stages of internal erosion interpreted from seismic monitoring. The time lag (proportional to the apparent velocity) computed from autocorrelation is represented as a slowness (the inverse of velocity) to present a trend similar to the cumulative number of seismic events.

The present results are difficult to compare to previous research since very few passive seismic monitoring of earth dams has been reported so far. On the IJkdijk experiment in Netherlands, Rittgers et al. (2015) successfully located acoustic emissions at depth that were associated to the development of sand/water boils. Similarly, Bièvre et al. (2017) were able to locate seepage a few metres below the crest of a real earth dam. In this work, it was not possible because of a too high seismic velocity in the concrete, preventing variable travel times to be retrieved from the cross-correlation of the 5 geophones initially set up. Planès et al. (2016) used passive seismic interferometry but started the experiment at the progression stage by artificially creating a pipe. Results from the present work show a decrease of the apparent seismic velocity (estimated from auto-correlation) as internal erosion develops. This is in agreement with their findings, which showed a decrease of seismic velocity (from cross-correlation) as internal erosion develops. Moreover, the results of this study suggest that seismic monitoring, using either Acoustic Emission or interferometry, is suitable do detect early stages of internal erosion.

These encouraging results have, however, to be confirmed, notably by conducting experiments at larger scale, using analogous models more representative of earth dams. Also, the methodology has to be extended to real sites where piping occurs at depth, typically several metres, to evaluate its ability to detect early stages of internal erosion. Notably, such sites are likely to exhibit much higher background noise than in the laboratory. Consequently, early stages of internal erosion will most probably exhibit amplitudes of the same order of magnitude than background noise. Extracting relevant information will then be challenging. It could be achieved using machine learning/artificial intelligence tools (e.g. Fisher et al., 2017) which are increasingly used to extract and cluster observations from various time-series.

4.5 Conclusions

A controlled laboratory experiment consisting of a pipe embedded into an inert concrete beam was designed to monitor early stages of internal erosion. The temporal evolution of the soil sample submitted to a constant hydraulic head was monitored with cameras to time-stamp the evolution of the seepage from saturation up to failure. Electrical resistivity was monitored with a single-channel device. Results did not bring any additional information about the internal erosion process due to the quickness of the experiment. Consequently, not enough observation was provided to monitor the changes in the soil structure. The ability of electrical parameters to capture such rapid changes in a laboratory experiment could be increased by testing other approaches. First, increasing the number of channels would allow increasing the number of measurements, and, consequently, the resolution, while keeping relatively short durations of acquisitions. Second, other sensitive electrical parameters could be tested, such as Induced Polarization and Spontaneous Potentials.

On the contrary, the seismic monitoring provided satisfactory results. The cumulative counts of seismic events along with the variations of apparent seismic velocity approximated from autocorrelation were calibrated with video monitoring. The spectral analysis showed that distinct events occurred for specific frequency ranges, such as water flow (5-20 Hz) and mass movements (80-120 Hz), allowing to monitor the full evolution of the experiment. The seismic time-series allowed to differentiate different stages: baseline, valve opening, water seepage, mass movements and failure. They reveal that the evolution of the soil sample with time is complex, nonlinear and can be subdivided into distinct episodes. Both visual observations and seismic interpretations of the data allowed the identification of the 4 different stages of internal erosion (i.e. initiation, continuation, progression and failure). The seismic data show high amplitude events preceding the progression phase identified in the snapshots. Hence this experiment suggests that seismic techniques are suitable to detect changes inside the structure of the soil which may lead to failure. These preliminary and encouraging results pave the way for more realistic experiments at larger scale.

CHAPTER 5
CONCLUSIONS AND PERSPECTIVES

Earth dams are structures that are built using soils of very low permeability to limit the seepage of water. However, water tends to create a path inside the soil matrix that would generate a seepage without the detachment of particles that would initiate internal erosion mechanisms. Nevertheless, the presence of favorable soil and hydraulic properties in the body of the earth dam might mitigate the evolution of the flow rate. Consequently, water seepage might evolve and trigger the start of the internal erosion process. Up until today, with the availability of multiple techniques to monitor earth structures (invasive and non-invasive), failure is still taking place, leading to fatalities and huge losses in infrastructure systems and water. The variability and the complexity of the soil structure behavior and its changes due to water seepage makes it difficult to detect the start of internal erosion and identify its evolution. Hence, by the time signs of internal erosion show, it is too late to prevent it. Accordingly, the study and delineation of the different stages of internal erosion is very critical to prevent the failure of the earth dam.

Internal erosion is a very complex phenomenon that is dependent on various factors in order to take place. The monitoring of earth dams using classical methods such as pore water pressure, deformations among others stated in Chapter 1 have proved not to be enough to prevent failures. Studies done previously have introduced the use of geophysical techniques but to our knowledge, none have studied the entire process of seepage, initiation, continuation, progression and failure.

The objectives in this study were to develop the use of geophysical techniques, mainly electrical resistivity and ambient seismics monitoring, to detect and monitor the flow of water in a porous medium, identify the changes of flow rates, the start of internal erosion and its evolution (differentiating the different stages). For this purpose, three experiments were conducted in the

laboratory under controlled parameters and limited ambient seismic activity as well as in the field at a larger scale for feasibility purposes.

Detection of water seepage solely in porous media was studied under both conditions: laboratory with a controlled setup and in the field where it was subjected to multiple sources of activity surrounding the experiment. Continuous monitoring using electrical resistivity and seismic techniques were implemented throughout both of the experiments. Internal erosion experiment was conducted uniquely in the laboratory using the setup of the water seepage test.

The laboratory experiment of water seepage showed that the seismic source originating from the seepage of water produced a distinctive signature consisting of a series of events taking place in the 160 – 190 Hz frequency band. These events were related to the seepage of water and seemed to increase in amplitude and in occurrence with the increase in the head of water. Furthermore, the changes occurring in the soil sample were reflected in the seismic energy. The increase beyond the critical head for initiation of internal erosion triggers higher amplitude events and faster occurrences.

Moreover, the evolution of the system was not linear. It is subjected to different stages of activation of seismic energy due to the evolution of the sample and stages of stability with very low seismic energy. These stages were observed following every increase in the upstream head leading to increases in the flow rates. On the other hand, the electrical resistivity technique showed variations in resistivity data between the upper and lower part of the seepage zone. However, the equipment used was not suitable due to the long time required to acquire the data. Also, the data acquired made it hard to identify any stages of increases in heads.

The setup in the experimental field was identical to the laboratory. It focused on the detection and monitoring of water seepage in a porous medium with the use of electrical resistivity and seismic techniques. Higher seismic energies were detected in the frequency ranges of 160 – 190 Hz and 180 – 220 Hz following the water seepage in the channel and the increase in the head applied in the reservoir (the head is not the direct cause, it is the water flow). Seismic energy was detected when no water was perceived at the downstream side. However, the distinctive events detected in the laboratory were not distinguished in the field experiment. Why?

Interestingly, the frequency bands of interest are similar in both experiments even though the dimensions of the entire setup are different. Nevertheless, the dimensions of the seepage zones are the same. These results are in accordance with previously published studies that detected energy in the same frequency bands following water seepage.

These two experiments focused on the use of seismic and electrical resistivity techniques for the detection of water seepage and quantifying it. It was concluded that the seismic energy increases when seepage of water exists. However, sufficient velocity must be present to initiate the detection of the seismic energy that could originate from the friction between the water and the soil particles, air bubbles movement, rearrangement of the soil particles or even cracks that might take place

within the soil matrix. There exists a threshold head of water (flow/velocity) that would trigger the system in both experiments creating enough seismic energy to be recorded by the geophones located on top.

The stages that were identified in the seismic analysis represent the stages that would take place during the filling of the reservoir that is represented by the increase changes in head. The experiments were conducted for increasing water heads and not the opposite to represent the fill/empty cycle of a dam. The fatigue, cracking and aging phenomena were not taken into consideration in this study in order to show whether (1) the threshold would be affected or (2) if the relaxation stage would be delayed (the seismic energy originating from the seepage of water might not be embedded in the seismic energy originating from the surrounding activity). These two factors could be significant in the early detection of internal erosion (the moment internal erosion is initiated).

Following the detection of the water flow and the better understanding of the seismic response to the behavior of the soil sample when subjected to different flow rates, a laboratory experiment was conducted to study the evolution of the seepage and the beginning of the internal erosion mechanism and its progress. The same laboratory setup for the monitoring of seepage was used but with a stable head and different soil characteristics to produce internal erosion phenomenon. In addition to geophysical techniques (electrical resistivity and seismic), video monitoring was introduced for better classification of the stages of the experiment. The electrical resistivity results do not bring any additional information to the ones observed in the video monitoring due to the fast progress of the experiment. However, the seismic results are more promising. The presence of the leakage of water at the upstream was used as an active source for autocorrelation and the event counts detected in the frequency range 80 – 120 Hz allowed the differentiation between seepage and internal erosion. Once internal erosion was initiated, seismic analyses were used to delineate its evolution through the cumulative seismic event counts. The variations observed in the count of seismic events as a function of time was further interpreted as related to the four different stages of internal erosion, namely initiation, continuation, progression and failure. The autocorrelation of the seismic data through the use of the water leakage upstream as an active source permitted the determination of the change in velocity of the propagation of the wave generated by the drop of water. The analysis showed changes related to the evolution of the soil medium throughout the internal erosion mechanism. The seismic interpretation revealed the nonlinear and complex progress of internal erosion as well as the coupling between water flow and changes in the soil matrix (deformations, cracks, ruptures, mass movements among others).

The results obtained in this study show promising outcome for the monitoring of earth dam using seismic techniques. The analyses performed on the laboratory experiments and the experimental dam pave the way to conduct tests on real scale earth dams in order to detect water seepage and monitor the evolution of the medium and the trigger point that would lead to internal erosion.

Finally, seepage of water could last for a very long time before internal erosion is initiated if it would ever seize to exist. It is challenging to predict, detect and quantify the seepage which is crucial to avoid internal erosion initiation that could progress undetected in the body of the earth dam. The soil/water interaction presents a very complex mechanism and lead to various mechanisms besides internal erosion such as liquefaction, flooding, erosion, contaminant transport and landslides. The behavior during water seepage in a porous medium shows a nonlinear behavior characterized by phases of high energy explained by the evolution of the system; it is then followed by steady state phases that are re-activated following changes in the soil matrix. This dynamism could be identified in cases such as landslides where a mass movement takes place succeeded by an equilibrium state that is re-initiated.

The following study showed the use of multi-physics techniques on multiscale experimental setups in the objective of detecting and monitoring seepage and internal erosion in porous media. The use of seismic techniques was successful in detecting impulsive events creating high energy in small scale experiments. Tests should be further conducted on larger scales to validate the results obtained in this study. The use of other analytical techniques (such as machine learning) could be incorporated to classify the impulsive events detected in the laboratory and compare them to the ones obtained in the field. The understanding of their origin could narrow down what to look for while monitoring earth dams. This advancement in continuous data acquisition could pave the way to creating alarm systems through the use of Artificial Intelligence (AI) that would prevent internal erosion to progress and lead to failure.

REFERENCES

Abdulsamad, F., Revil, A., Soueid Ahmed, A., Coperey, A., Karaoulis, M., Nicaise, S., and Peyras, L. (2019). Induced polarization tomography applied to the detection and the monitoring of leaks in embankments. *Engineering Geology*, *254*, 89–101. https://doi.org/10.1016/j.enggeo.2019.04.001

Adamo, N., Al-Ansari, N., Sissakian, V., Laue, J., and Knutsson, S. (2020a). Dam Safety: Technical Problems of Aging Embankment Dams. *Journal of Earth Sciences and Geotechnical Engineering*, *10*(6), 281–322.

Adamo, N., Al-Ansari, N., Sissakian, V., Laue, J., and Knutsson, S. (2020b). Geophysical Methods and their Applications in Dam Safety Monitoring. *Journal of Earth Sciences and Geotechnical Engineering*, *11*(1), 291–345. https://doi.org/10.47260/jesge/1118

Artières, O., Bonelli, S., Fabre, J. P., Guidoux, C., Radzicki, K., Royet, P., and Vedrenne, C. (2007). Active and Passive Defences against Internal Erosion. In *Assessment of the risk of internal erosion of water retaining structures: dams, dikes and levees* (Issue 114, pp. 235–244). Deutsches Talsperren Komitee.

ASDSO (Association of State Dam Safety Officials). (2021). Retrieved July 13, 2021 from: https://damfailures.org/

ASTM D6913 / D6913M-17, Standard Test Methods for Particle-Size Distribution (Gradation) of Soils Using Sieve Analysis, ASTM International, West Conshohocken, PA, 2017, www.astm.org. DOI: 10.1520/D6913_D6913M-17

ASTM D854-14, Standard Test Methods for Specific Gravity of Soil Solids by Water Pycnometer, ASTM International, West Conshohocken, PA, 2014, www.astm.org. DOI: 10.1520/D0854-14

Barnes, M. (1992). Famous Failures: Revisiting Major Dam Catastrophes. *ASDSO Annual Conference*, 363–368.

Beck, Y., Khan, A., Cunat, P., Guidoux, C., Artières, O., Mars, J., and Fry, J. (2010). Thermal monitoring of embankment dams by fiber optics. *Proc. 8th ICOLD European Club Symposium on Dam Safety*, 444–448.

Bellanova, J., Calamita, G., Giocoli, A., Luongo, R., Macchiato, M., Perrone, A., Uhlemann, S., and Piscitelli, S. (2018). Electrical resistivity imaging for the characterization of the Montaguto landslide (southern Italy). *Engineering Geology*, *243*, 272–281. https://doi.org/10.1016/j.enggeo.2018.07.014

Bièvre, G., Franz, M., Larose, E., Carrière, S., Jongmans, D., and Jaboyedoff, M. (2018). Influence of environmental parameters on the seismic velocity changes in a clayey mudflow (Pont-

Bourquin Landslide, Switzerland). *Engineering Geology*, *245*, 248–257. https://doi.org/10.1016/j.enggeo.2018.08.013

Bièvre, G., Jongmans, D., Lebourg, T., and Carrière, S. (2021). Electrical resistivity monitoring of an earthslide with electrodes located outside the unstable zone (Pont-Bourquin landslide, Swiss Alps). *Near Surface Geophysics*, *19*(2), 225–239. https://doi.org/10.1002/NSG.12145

Bièvre, G., Lacroix, P., Oxarango, L., Goutaland, D., Monnot, G., and Fargier, Y. (2017). Integration of geotechnical and geophysical techniques for the characterization of a small earth-filled canal dyke and the localization of water leakage. *Journal of Applied Geophysics*, *139*, 1–15. https://doi.org/10.1016/j.jappgeo.2017.02.002

Bligh, W. G. (1910). Dams, barrages and weirs on porous foundations. *Engineering News*, *64*(26), 708–710.

Boleve, A., Janod, F., Revil, A., Lafon, A., and Fry, J.-J. (2011). Localization and quantification of leakages in dams using time-lapse self-potential measurements associated with salt tracer injection. *Journal of Hydrology*, *403*(3–4), 242–252. https://doi.org/10.1016/j.jhydrol.2011.04.008

Bonelli, S. (2013). *Erosion in geomechanics applied to dams and levees* (S. Bonelli and F. Nicot (Eds.)). John Wiley and Sons. https://doi.org/10.1002/9781118577165

Busato, L., Boaga, J., Peruzzo, L., Himi, M., Cola, S., Bersan, S., and Cassiani, G. (2016). Combined geophysical surveys for the characterization of a reconstructed river embankment. *Engineering Geology*, *211*, 74–84. https://doi.org/10.1016/j.enggeo.2016.06.023

Butler, D. K., Llopis, J. L., and Deaver, C. M. (1989). Comprehensive geophysical investigation of an existing dam foundation, Part 1. *Leading Edge*, *8*(8), 10–18. https://doi.org/10.1190/1.1439645

Calamak, M., and Yilmaz, M. (2018). A Review of the Anita Dam Incident: Internal Erosion Caused by a Buried Conduit and Lessons Learned. *5th International Symposium on Dam Safety*. https://www.researchgate.net/publication/328748365

Camarero, P. L., Moreira, C. A., and Pereira, H. G. (2019). Analysis of the Physical Integrity of Earth Dams from Electrical Resistivity Tomography (ERT) in Brazil. *Pure and Applied Geophysics*, *176*(12), 5363–5375. https://doi.org/10.1007/s00024-019-02271-8

Cardarelli, E., Cercato, M., and De Donno, G. (2014). Characterization of an earth-filled dam through the combined use of electrical resistivity tomography, P- and SH-wave seismic tomography and surface wave data. *Journal of Applied Geophysics*, *106*, 87–95. https://doi.org/10.1016/j.jappgeo.2014.04.007

Chambers, J. E., Gunn, D. A., Wilkinson, P. B., Meldrum, P. I., Haslam, E., Holyoake, S., Kirkham, M., Kuras, O., Merritt, A., and Wragg, J. (2014). 4D electrical resistivity

tomography monitoring of soil moisture dynamics in an operational railway embankment. *Near Surface Geophysics*, *12*(1), 61–72. https://doi.org/10.3997/1873-0604.2013002

Chlaib, H. K., Mahdi, H., Al-Shukri, H., Su, M. M., Catakli, A., and Abd, N. (2014). Using ground penetrating radar in levee assessment to detect small scale animal burrows. *Journal of Applied Geophysics*, *103*, 121–131. https://doi.org/10.1016/j.jappgeo.2014.01.011

Clément, R., Fargier, Y., Dubois, V., Gance, J., Gros, E., and Forquet, N. (2020) OhmPi: An open source data logger for dedicated applications of electrical resistivity imaging at the small and laboratory scale. HardwareX, , e00122. doi:10.1016/j.ohx.2020.e00122

Clement, R., and Moreau, S. (2016). How should an electrical resistivity tomography laboratory test cell be designed? Numerical investigation of error on electrical resistivity measurement. *Journal of Applied Geophysics*, *127*, 45–55. https://doi.org/10.1016/J.JAPPGEO.2016.02.008

Clements, T., and Denolle, M. A. (2018). Tracking Groundwater Levels Using the Ambient Seismic Field. *Geophysical Research Letters*, *45*(13), 6459–6465. https://doi.org/10.1029/2018GL077706

CFBR (Comité Français des Barrages et Réservoirs). (2012). Retrieved July 13, 2021 from: https://www.barrages-cfbr.eu/

Crawford, M. M., and Bryson, L. S. (2018). Assessment of active landslides using field electrical measurements. *Engineering Geology*, *233*, 146–159. https://doi.org/10.1016/j.enggeo.2017.11.012

de Wit, T., and Olivier, G. (2018). Imaging and monitoring tailings dam walls with ambient seismic noise. *Proceedings of the 21st International Seminar on Paste and Thickened Tailings*, 455–464. https://doi.org/10.36487/acg_rep/1805_37_de_wit

Deangeli, C., Giani, G. P., Chiaia, B., and Fantilli, A. P. (2009). Dam failures. *WIT Transactions on State-of-the-Art in Science and Engineering*, *36*. https://doi.org/10.2495/978-1-84564-142-9/01

Di Prinzio, M., Bittelli, M., Castellarin, A., and Pisa, P. R. (2010). Application of GPR to the monitoring of river embankments. *Journal of Applied Geophysics*, *71*(2–3), 53–61. https://doi.org/10.1016/j.jappgeo.2010.04.002

Engemoen, W. (2014). *Design Standards No.13: Embankment Dams. United States Bureau of Reclamation (USBR)*.

Evers, M., Kyriou, A., Thiele, A., Hammer, H., Schulz, K., and Nikolakopoulos, K. G. (2020). How to set up a dam monitoring system with PSInSAR and GPS. In K. Schulz, K. G. Nikolakopoulos, and U. Michel (Eds.), *Earth Resources and Environmental Remote Sensing/GIS Applications XI* (Vol. 11534, p. 18). SPIE. https://doi.org/10.1117/12.2573880

Federal Emergency Management Agency (FEMA). (2011). *Technical Manual: Filters for Embankment Dams Best Practices for Design and Construction*.

Federal Emergency Management Agency (FEMA). (2005). *Technical Manual: Conduits through Embankment Dams. Best Practices for Design, Construction, Problem Identification and Evaluation, Inspection, Maintenance, Renovation, and Repair*.

Federal Emergency Management Agency (FEMA). (2015). *Technical Manual: Evaluation and Monitoring of Seepage and Internal Erosion Interagency Committee on Dam Safety (ICODS)*.

Fell, R., Foster, M., Cyganiewicz, J., Sills, G., Vroman, N., and Davidson, R. (2008). Risk Analysis for Dam Safety: A Unified Method for Estimating Probabilities of Failure of Embankment Dams by Internal Erosion and Piping. UNICIV Report R466. In *the University of South Wales, Sydney, Australia*.

Fell, R., and Fry, J. J. (2007). The state of the art of assessing the likelihood of internal erosion of embankment dams, water retaining structures and their foundations. In *Internal Erosion of Dams and Their Foundations* (pp. 9–32). CRC Press. https://doi.org/10.1201/9781482266146-6

Fell, R., MacGregor, P., Stapledon, D., Bell, G., and Foster, F. (2015). *Geotechnical Engineering of Dams* (2nd editio). CRC Press.

Fell, R., Wan, C. F., Cyganiewicz, J., and Foster, M. (2003). Time for Development of Internal Erosion and Piping in Embankment Dams. *Journal of Geotechnical and Geoenvironmental Engineering*, *129*(4), 307–314. https://doi.org/10.1061/(ASCE)1090-0241(2003)129:4(307)

Fisher, W., Camp, T., and Krzhizhanovskaya, V. (2016). Crack detection in earth dam and levee passive seismic data using support vector machines. *Procedia Computer Science*, *80*, 577–586. https://doi.org/10.1016/j.procs.2016.05.339

Fisher, W., Jaclson, B.Camp, T., and Krzhizhanovskaya, V. (2017). Anomaly detection in earth dam and levee passive seismic data using multivariate Gaussian. *Proceedings - 16th IEEE International Conference on Machine Learning and Applications, ICMLA 2017*, *2017-Decem*, 685–690. https://doi.org/10.1109/ICMLA.2017.00-81

Foley, N., Tulaczyk, S. M., Grombacher, D., Doran, P. T., Mikucki, J., Myers, K. F., Foged, N., Dugan, H., Auken, E., and Virginia, R. (2019). Evidence for pathways of concentrated submarine groundwater discharge in east Antarctica from helicopter-borne electrical resistivity measurements. *Hydrology*, *6*(2), 54. https://doi.org/10.3390/hydrology6020054

Foster, M., and Fell, R. (1999). *A framework for estimating the probability of failure of embankment dams by internal erosion and piping using event tree methods. UNICIV Report No. R-377. The University of New South Wales, Australia*.

Foster, M., Fell, R., and Spannagle, M. (2000a). A method for assessing the relative likelihood of failure of embankment dams by piping. *Canadian Geotechnical Journal*, *37*(5), 1025–1061. https://doi.org/10.1139/cgj-37-5-1025

Foster, M., Fell, R., and Spannagle, M. (2000b). The statistics of embankment dam failures and accidents. *Canadian Geotechnical Journal*, *37*(5), 1000–1024. https://doi.org/10.1139/cgj-37-5-1000

Foster, M.A., Fell, R., and Spannagle, M. (1998) Analysis of embankment dam incidents. UNICIV Rep. No. R-374, University of New South Wales, Sydney, Australia.

France, J. W., Alvi, I. A., Dickson, P. A., Falvey, H. T., Rigbey, S. J., and Trojanowski, J. (2018). Independent Forensic Team Report: Oroville Dam Spillway Incident.

Gance, J., Malet, J. P., Supper, R., Sailhac, P., Ottowitz, D., and Jochum, B. (2016). Permanent electrical resistivity measurements for monitoring water circulation in clayey landslides. *Journal of Applied Geophysics*, *126*, 98–115. https://doi.org/10.1016/j.jappgeo.2016.01.011

Garambois, S., Voisin, C., Romero Guzman, M.A., Brito, D., Guillier, B., and Réfloch, A. (2019) Analysis of ballistic waves in seismic noise monitoring of water table variations in a water field site: added value from numerical modelling to data understanding. *Geophysical Journal International*, 219, 1636-1647. doi:10.1093/gji/ggz391

Garg, S. K. (2002). *Irrigation Engineering and Hydraulic Structures* (16th ed., Vol. 1). Khanna Publishers.

Gevaert, J. H. N. (2019). *Monitoring Backward Erosion Piping with Self-Potential Geophysics. Master Thesis*. Delft University of Technology.

Gökalp, E., and Taşçi, L. (2009). Deformation monitoring by gps at embankment dams and deformation analysis. *Survey Review*, *41*(311), 86–102. https://doi.org/10.1179/003962608X390021

González, J. A. M., Comte, J.-C., Legchenko, A., Ofterdinger, U., and Healy, D. (2021). Quantification of groundwater storage heterogeneity in weathered/fractured basement rock aquifers using electrical resistivity tomography: Sensitivity and uncertainty associated with petrophysical modelling. *Journal of Hydrology*, *593*, 125637. https://doi.org/10.1016/j.jhydrol.2020.125637

Graham, W.J. (1999) A procedure for estimating loss of life caused by dam failures. Tech Report No DSO-99-06, *Unite States Bureau of Reclamation*, Washington DC, USA.

Graham, W. (2008). The teton dam failure-an effective warning and evacuation. *Association of State Dam Safety Officials 25th Anniversary Conference*.

Guireli, L., Malagutti Filho, W., and Gandolfo, O. (2020). Detection of seepage paths in small earth dams using the self-potential method (SP). *REM-International Engineering Journal*, *73*(3), 303–310. https://doi.org/10.1590/0370-44672018730168

Gunn, D.A., Chambers, J.E., Dashwood, B.E., Lacinska, A., Dijkstra, T., Uhlemann, S., Swift, R., Kirkham, M., Milodowski, A., Wragg, J., and Donohue, S. (2018) Deterioration model and condition monitoring of aged railway embankment using non-invasive geophysics. *Construction and Building Materials*, 170, 668-678. doi:10.1016/j.conbuildmat.2018.03.066

Günther, T., Rücker, C., and Spitzer, K. (2006) Three-dimensional modelling and inversion of DC resistivity data incorporating topography - II. Inversion. *Geophysical Journal International*, 166, 506-517. doi:10.1111/j.1365-246X.2006.03011.x

Hayley, K., Bentley, L. R., Gharibi, M., and Nightingale, M. (2007). Low temperature dependence of electrical resistivity: Implications for near surface geophysical monitoring. *Geophysical Research Letters*, *34*(18), L18402. https://doi.org/10.1029/2007GL031124

Hayley, K., Bentley, L. R., and Pidlisecky, A. (2010). Compensating for temperature variations in time-lapse electrical resistivity difference imaging. *Geophysics*, *75*(4), 1JA-Z98. https://doi.org/https://doi.org/10.1190/1.3478208

Heinze, T., Limbrock, J. K., Pudasaini, S. P., and Kemna, A. (2019). Relating mass movement with electrical self-potential signals. *Geophysical Journal International*, *216*(1), 55–60. https://doi.org/10.1093/gji/ggy418

Hermans, T., and Paepen, M. (2020). Combined Inversion of Land and Marine Electrical Resistivity Tomography for Submarine Groundwater Discharge and Saltwater Intrusion Characterization. *Geophysical Research Letters*, *47*(3). https://doi.org/10.1029/2019GL085877

Hickey, C. J., Ekimov, A., Hanson, G. J., and Sabatier, J. M. (2009). Time-lapse seismic measurements on a small earthen embankment during an internal erosion experiment. *22nd EEGS Symposium on the Application of Geophysics to Engineering and Environmental Problems*, 144–156. https://doi.org/10.4133/1.3176689

Himi, M., Casado, I., Sendros, A., Lovera, R., Casas, A., and Rivero, L. (2016). Using the resistivity method for leakage detection at Sant Llorenç de Montgai Embankment (Lleida, NE Spain). *Near Surface Geoscience 2016-22nd European Meeting of Environmental and Engineering Geophysics*, *2016*(1), cp--495. https://doi.org/10.3997/2214-4609.201601925

Hirose, T., Nakahara, H., and Nishimura, T. (2017) Combined use of repeated active shots and ambient noise to detect temporal changes in seismic velocity: application to Sakurajima volcano, Japan. *Earth, Planets and Space*, 69, 42. doi:10.1186/s40623-017-0613-7

Hung, M.-H., Lauchle, G. C., and Wang, M. C. (2009). Seepage-Induced Acoustic Emission in Granular Soils. *Journal of Geotechnical and Geoenvironmental Engineering*, *135*(4), 566–572. https://doi.org/10.1061/(ASCE)1090-0241(2009)135:4(566)

ICOLD (International Commission on Large Dams). (2020). Retrieved July 13, 2021 from: https://www.icold-cigb.org/

ICOLD. (2017). Bulletin 164: Internal Erosion of Existing Dams, Levees and Dikes, and their Foundations. In *ICOLD Bulletin* (Vol. 1, Issue B164).

ICOLD (2001) *Tailings dams risk of dangerous occurences. Lessons learnt from practical experiences*. *ICOLD Bulletin*, 121, International Commission on Large Dams, ICOLD, Paris, France.

Ikard, S. J., Revil, A., Jardani, A., Woodruff, W. F., Parekh, M., and Mooney, M. (2012). Saline pulse test monitoring with the self-potential method to nonintrusively determine the velocity of the pore water in leaking areas of earth dams and embankments. *Water Resources Research*, *48*(4), 752–752. https://doi.org/10.1029/2010wr010247

Ikard, S. J., Rittgers, J., Revil, A., and Mooney, M. A. (2015). Geophysical investigation of seepage beneath an earthen dam. *Groundwater*, *53*(2), 238–250. https://doi.org/10.1111/gwat.12185

Johansson, S., Beaupretre, S., and Boue, A. (2021). *Distributed Acoustic Sensing for Detection of Defects in the Test Dam at Älvkarleby. [Technical Report].* www.energiforsk.se

Johansson, S., and Sjödahl, P. (2004). Downstream seepage detection using temperature measurements and visual inspection – monitoring experiences from røsvatn field test dam and large embankment dams in sweden. *Stability and Breaching of Embankment Dams*, 20.

Karl, L., Fechner, T., Schevenels, M., and Degrande, G. (2011). Geotechnical characterization of a river dyke by surface waves. *Near Surface Geophysics*, *9*(6), 515–527. https://doi.org/10.3997/1873-0604.2011030

Khan, A. A., Vrabie, V., Beck, Y. L., Mars, J. I., and D'Urso, G. (2014). Monitoring and early detection of internal erosion: Distributed sensing and processing. *Structural Health Monitoring*, *13*(5), 1–15. https://doi.org/10.1177/1475921714532994

Koerner, R.M., McCabe, W.M., and Baldivieso, L.F. (1981) Acoustic emission monitoring of seepage. *Journal of the Geotechnical Engineering Division*, 107, 521-526. doi:10.1061/ajgeb6.0001414

Larose, E., Carrière, S., Voisin, C., Bottelin, P., Baillet, L., Guéguen, P., Walter, F., Jongmans, D., Guillier, B., Garambois, S., Gimbert, F., and Massey, C. (2015). Environmental seismology: What can we learn on earth surface processes with ambient noise? *Journal of Applied Geophysics*, *116*, 62–74. https://doi.org/10.1016/j.jappgeo.2015.02.001

Lecocq, T., Longuevergne, L., Pedersen, H. A., Brenguier, F., and Stammler, K. (2017). Monitoring ground water storage at mesoscale using seismic noise: 30 years of continuous observation and thermo-elastic and hydrological modeling. *Scientific Reports*, *7*(1), 1–16. https://doi.org/10.1038/s41598-017-14468-9

Lin, W., Liu, A., Mao, W., and Koseki, J. (2020). Acoustic emission behavior of granular soils with various ground conditions in drained triaxial compression tests. *Soils and Foundations*, *60*(4), 929–943. https://doi.org/10.1016/J.SANDF.2020.06.002

Lu, Z., and Wilson, G. V. (2012). Acoustic Measurements of Soil Pipeflow and Internal Erosion. *Soil Science Society of America Journal*, *76*(3), 853–866. https://doi.org/10.2136/SSSAJ2011.0308

Lumbroso, D., Davison, M., Body, R., and Petkovšek, G. (2021). Modelling the Brumadinho tailings dam failure, the subsequent loss of life and how it could have been reduced. *Natural Hazards and Earth System Sciences*, *21*(1), 21–37. https://doi.org/10.5194/nhess-21-21-2021

Mallet, T., Fry, J. J., and Tourment, R. (2019). Accidentology of the levees of the Rhône delta from 1840 to the present day. *Digues Maritimes et Fluviales de Protection Contre Les Inondations*. https://doi.org/10.5281/zenodo.2530102

Martínez-Moreno, F. J., Delgado-Ramos, F., Galindo-Zaldívar, J., Martín-Rosales, W., López-Chicano, M., and González-Castillo, L. (2018). Identification of leakage and potential areas for internal erosion combining ERT and IP techniques at the Negratín Dam left abutment (Granada, southern Spain). *Engineering Geology*, *240*, 74–80. https://doi.org/10.1016/j.enggeo.2018.04.012

Mc Dowell, P., Barker, R., Butcher, A., Culshaw, M., Jackson, P., McCann, D., Skipp, B., Matthews, S., and Arthur, J. (2002). *Geophysics in engineering investigations* (Vol. 19). Geological Society of London. https://doi.org/doi.org/10.1144/GSL.ENG.2002.019

Moore, J. R., Boleve, A., Sanders, J. W., and Glaser, S. D. (2011). Self-potential investigation of moraine dam seepage. *Journal of Applied Geophysics*, *74*(4), 277–286. https://doi.org/10.1016/j.jappgeo.2011.06.014

Morales-Nápoles, O., Delgado-Hernández, D.J., De-León-Escobedo, D., and Arteaga-Arcos, J.C. (2014) A continuous Bayesian network for earth dams' risk assessment: methodology and quantification. *Structure and Infrastructure Engineering*, 10, 589-603. doi:10.1080/15732479.2012.757789

Mordret, A., Courbis, R., Brenguier, F., Chmiel, M., Garambois, S., Mao, S., Boué, P., Campman, X., Lecocq, T., der Veen, W., and others. (2020). Noise-based ballistic wave passive seismic monitoring--Part 2: surface waves. *Geophysical Journal International*, *221*(1), 692–705.

Mydlikowski, R., Beziuk, G., and Szynkiewicz, A. (2007). Detection of inhomogeneities in structure of flood embankments by means of D.C. resistivity, GPR and frequency

electromagnetic method measurements – Short note. *Acta Geodynamica et Geomaterialia*, *4*(4), 83–88.

Nayebzadeh, R., and Mohammadi, M. (2011). The Effect of Impervious Clay Core Shape on the Stability of Embankment Dams. *Geotechnical and Geological Engineering*, *29*, 627–635. https://doi.org/10.1007/s10706-011-9395-z

Pagano, L., Fontanella, E., Sica, S., and Desideri, A. (2010). Pore water pressure measurements in the interpretation of the hydraulic behaviour of two earth dams. *Soils and Foundations*, *50*(2), 295–307. https://doi.org/10.3208/sandf.50.295

Parekh, M. L. (2016). *Advancing Internal Erosion Monitoring Using Seismic Methods in Field and Laboratory Studies. Thesis*. Colorado School of Mines.

Park. (2017). Technical report: Geophysical methods for reservoir safety investigations. In *Environment Agency and British Dam Society*.

Park, Yi, M. J., Kim, J. H., and Shin, S. W. (2016). Electrical resistivity imaging (ERI) monitoring for groundwater contamination in an uncontrolled landfill, South Korea. *Journal of Applied Geophysics*, *135*, 1–7. https://doi.org/10.1016/j.jappgeo.2016.07.004

Planès, T., Mooney, M. A., Rittgers, J. B. R., Parekh, M. L., Behm, M., and Snieder, R. (2016). Time-lapse monitoring of internal erosion in earthen dams and levees using ambient seismic noise. *Geotechnique*, *66*(4), 301–312. https://doi.org/10.1680/jgeot.14.P.268

Revil, A., Karaoulis, M., Johnson, T., and Kemna, A. (2012). Review: Some low-frequency electrical methods for subsurface characterization and monitoring in hydrogeology. *Hydrogeology Journal*, *20*(4), 617–658. https://doi.org/10.1007/s10040-011-0819-x

Rice, J., and Swainston-Fleshman, M. (2013). Laboratory Modeling of Critical Hydraulic Conditions for the Initiation of Piping. *Geo-Congress 2013: Stability and Performance of Slopes and Embankments III*, 1044–1055. https://doi.org/10.1061/9780784412787.106

Rinehart, R. V, Parekh, M. L., Rittgers, J. B., Mooney, M. a, and Revil, A. (2012). Preliminary Implementation of Geophysical Techniques to Monitor Embankment Dam Filter Cracking at the Laboratory Scale. *6th International Conference on Scour and Erosion (ICSE-6)*, 1401–1408.

Rittgers, J. B. B., Revil, A., Planes, T., Mooney, M. A. A., and Koelewijn, A. R. R. (2015). 4-D Imaging of Seepage in Earthen Embankments with Time-Lapse Inversion of Self-Potential Data Constrained by Acoustic Emissions Localization. *Geophysical Journal International*, *200*(2), 756–770. https://doi.org/10.1093/gji/ggu432

Robbins, B. A., and Griffiths, D. V. (2018). Internal erosion of embankments: A review and appraisal. In ASCE (Ed.), *Rocky Mountain Geo-Conference 2018* (pp. 61–75). ASCE. https://doi.org/10.1061/9780784481936.005

Rücker, C., Günther, T., and Spitzer, K. (2006). Three-dimensional modelling and inversion of dc resistivity data incorporating topography — I. Modelling. *Geophysical Journal International*, *166*(2), 495–505. https://doi.org/10.1111/J.1365-246X.2006.03010.X

Scaioni, M., Marsella, M., Crosetto, M., Tornatore, V., and Wang, J. (2018). Geodetic and remote-sensing sensors for dam deformation monitoring. *Sensors (Switzerland)*, *18*(11), 3682. https://doi.org/10.3390/s18113682

Sellmeijer, H., de la Cruz, J. L., van Beek, V. M., and Knoeff, H. (2011). Fine-tuning of the backward erosion piping model through small-scale, medium-scale and ijkdijk experiments. *European Journal of Environmental and Civil Engineering*, *15*(8), 1139–1154. https://doi.org/10.1080/19648189.2011.9714845

Sens-Schönfelder, C., and Wegler, U. (2006). Passive image interferometry and seasonal variations of seismic velocities at Merapi Volcano, Indonesia. *Geophysical Research Letters*, *33*(21). https://doi.org/10.1029/2006GL027797

Sentenac, P., Benes, V., and Keenan, H. (2018). Reservoir assessment using non-invasive geophysical techniques. *Environmental Earth Sciences*, *77*(293). https://doi.org/10.1007/s12665-018-7463-x

Sharma, R. P., and Kumar, A. (2013). Case Histories of Earthen Dam Failures. *Seventh International Conference on Case Histories in Geotechnical Engineering*, *May*, 0–7.

Shin, S., Park, S., and Kim, J. H. (2019). Time-lapse electrical resistivity tomography characterization for piping detection in earthen dam model of a sandbox. *Journal of Applied Geophysics*, *170*. https://doi.org/10.1016/j.jappgeo.2019.103834

Silva Rotta, L. H., Alcântara, E., Park, E., Negri, R. G., Lin, Y. N., Bernardo, N., Mendes, T. S. G., and Souza Filho, C. R. (2020). The 2019 Brumadinho tailings dam collapse: Possible cause and impacts of the worst human and environmental disaster in Brazil. *International Journal of Applied Earth Observation and Geoinformation*, *90*, 102119. https://doi.org/10.1016/j.jag.2020.102119

Sjödahl, P. (2006). *Resistivity investigation and monitoring for detection of internal erosion and anomalous seepage in dams. [Thesis]*. Lund University.

Sjödahl, P., Dahlin, T., and Johansson, S. (2010). Using the resistivity method for leakage detection in a blind test at the Røssvatn embankment dam test facility in Norway. *Bulletin of Engineering Geology and the Environment*, *69*(4), 643–658. https://doi.org/10.1007/s10064-010-0314-y

Sjödahl, P., Dahlin, T., Johansson, S., and Loke, M. H. (2008). Resistivity monitoring for leakage and internal erosion detection at Hällby embankment dam. *Journal of Applied Geophysics*, *65*(3–4), 155–164. https://doi.org/10.1016/j.jappgeo.2008.07.003

Sjödahl, P., Dahlin, T., and Johansson, S. (2009) Embankment dam seepage evaluation from resistivity monitoring data. *Near Surface Geophysics*, 7, 463-474. doi:10.3997/1873-0604.2009023

Smith, A., and Dixon, N. (2019). Acoustic emission behaviour of dense sands. *Geotechnique*, *69*(12), 1107–1122. https://doi.org/10.1680/JGEOT.18.P.209

Snieder, R., Grêt, A., Douma, H., and Scales, J. (2002). Coda wave interferometry for estimating nonlinear behavior in seismic velocity. *Science*, *295*(5563), 2253–2255. https://doi.org/10.1126/science.1070015

Soueid Ahmed, A., Revil, A., Bolève, A., Steck, B., Vergniault, C., Courivaud, J. R., Jougnot, D., and Abbas, M. (2020). Determination of the permeability of seepage flow paths in dams from self-potential measurements. *Engineering Geology*, *268*(105514). https://doi.org/10.1016/j.enggeo.2020.105514

Stephens, T. (2010). *Manual on small earth dams A guide to siting, design and construction* (FAO). Food and Agriculture Organization of the United Nations.

Taşçi, L. (2008). Dam deformation measurements with GPS. *Geodesy and Cartography*, *34*(4), 116–121. https://doi.org/10.3846/1392-1541.2008.34.116-121

Terzaghi, K., and Peck, R. (1948). *Soil Mechanics in Engineering Practices*. John Wiley and Sons, Inc.

Terzaghi, K., Peck, R., and Gholamreza, M. (1996). *Soil Mechanics in Engineering Practice* (3rd ed.). John Wiley and Sons.

The Daily Star - Lebanon. (2015). Retrieved July 13, 2021 from: https://m.dailystar.com.lb/News/Lebanon-News/2015/May-20/298642-mount-lebanon-reservoirs-burst-causing-massive-flooding.ashx

Tourment, R., Beullac, B., Peeters, P., Pohl, R., Bottema, M., Van, M., and Rushworth, A. (2018). *European and US Levees and Flood Defences Characteristics, Risks and Governance*. [Research Report] irstea. pp.173. ⟨hal-02609228⟩

Tucker-Kulesza, S., Rutherford, C., and Bernhardt-Barry, M. (2019). Electrical Resistivity at Internal Erosion Locations in Levees. *ISSMGE International Journal of Geoengineering Case Histories*, *5*(2), 55–69. https://doi.org/10.4417/IJGCH-05-02-01

United Nations. (2019). The sustainable development goals report 2019. *United Nations Publication Issued by the Department of Economic and Social Affairs*, 64. https://undocs.org/E/2019/68

USACE. (2004). *Engineering and Design: General Design and Construction Considerations for Earth and Rock-Fill Dams*. CreateSpace Independent Publishing Platform.

Van Beek, V. M., Van Essen, H. M., Vandenboer, K., and Bezuijen, A. (2015). Developments in modelling of backward erosion piping. *Geotechnique*, *65*(9), 740–754. https://doi.org/10.1680/geot.14.P.119

Van Beek, V.M., Bezuijen, A., and Sellmeijer, H. (2013). *3*. In: Bonelli, S., and Nicot, F. (Ed.), *Backward erosion piping*, John Wiley and Sons, Ltd.

Voisin, C., Garambois, S., Massey, C., and Brossier, R. (2016). Seismic noise monitoring of the water table in a deep-seated, slow-moving landslide. *Interpretation*, *4*(3), SJ67–SJ76. https://doi.org/10.1190/INT-2016-0010.1

Wahl, T., Regazzoni, P.-L., and Erdogan, Z. (2008) Determining erosion indices of cohesive soils with the Hole Erosion Test and Jet Erosion Test. *United States Bureau of Reclamation, Denver, USA*.

Wan, C. F., and Fell, R. (2004). Investigation of Rate of Erosion of Soils in Embankment Dams. *Journal of Geotechnical and Geoenvironmental Engineering*, *130*(4), 373–380. https://doi.org/10.1061/(ASCE)1090-0241(2004)130:4(373)

Weller, A., Lewis, R., Canh, T., Möller, M., and Scholz, B. (2014) Geotechnical and Geophysical Long-term Monitoring at a Levee of Red River in Vietnam. *Journal of Environmental and Engineering Geophysics*, 19, 183-192. doi:10.2113/JEEG19.3.183

Wiltshire, R. L. (2002). 100 Years of embankment dam design and construction in the US Bureau of Reclamation. Technical Report. In *Bureau of Reclamation History Symposium*.

Yavaşoğlu, H. H., Kalkan, Y., Tiryakioğlu, Yigit, C. O., Özbey, V., Alkan, M. N., Bilgi, S., and Alkan, R. M. (2018). Monitoring the deformation and strain analysis on the Ataturk Dam, Turkey. *Geomatics, Natural Hazards and Risk*, *9*(1), 94–107. https://doi.org/10.1080/19475705.2017.1411400

Yuwono, B. D., and Prasetyo, Y. (2019). Analysis Deformation Monitoring Techniques Using GNSS Survey and Terrestrial Survey (Case Study: Diponegoro University Dam,Semarang, Indonesia). *IOP Conference Series: Earth and Environmental Science*, *313*(1), 12045. https://doi.org/10.1088/1755-1315/313/1/012045

Zimmerman, L. J., and Chen, S. T. (1992). Geophysical Methods for Reservoir Characterization. *Permian Basin Oil and Gas Recovery Conference*, SPE-23953-MS. https://doi.org/10.2118/23953-ms

APPENDIX

Appendix A

Table A-1 Rate of development and detectability of internal erosion through the embankment (Fell et al., 2015)

Phase of Development	*Mechanism*	*Usual Rate of Development*	*Ease of Detection*	*Method of Detection*
Initiation	Global backward erosion in the core	Medium to slow, potentially rapid to very rapid at the end	Difficult (unless observed at downstream face)	Pore pressure, seepage, thermal, geophysical Visual if emerges on the downstream face
	Concentrated leak in a crack or in a hydraulic fracture	Rapid or very rapid, medium if soil very resistant to erosion	Difficult	Seepage, visual if the crack emerges on the downstream face
	Concentrated leak in cracks or hydraulic fracture, associated with conduits or walls	Rapid or very rapid	Difficult	Seepage, visual.
	Suffusion/internal instability	Rapid for internally unstable soils. Medium to slow if soils graded so internal instability is marginal	Moderate to difficult	Pore pressure, seepage, thermal, geophysical, visual if emerges on the downstream face
Continuation	Filters satisfying no-erosion criteria	Erosion will cease		
	Filters satisfying excessive erosion criteria	Rapid to very rapid	Moderate to difficult	Seepage, pore pressure
	Filters not satisfying continuing erosion criteria, or no filters	Rapid to very rapid	Moderate to difficult	Seepage, pore pressure
Progression to form a pipe, and a breach	Gross enlargement; and slope instability linked to development of a pipe.	Very rapid or rapid	Moderate to readily	Seepage, visual
Assess time using method in Section 8.9.2	Crest settlement or/and sinkhole in embankment	Usually slow to medium.	Readily	Visual, survey, seepage
	Slope instability, unravelling or sloughing	Usually slow to medium unless linked to rapid development of pipe.	Readily to Moderate	Visual, survey, seepage

Table A-2 Rate of development and detectability of internal erosion through the foundation, and from the embankment to the foundation (Fell et al., 2015)

Phase of development	*Mechanism*	*Usual Rate of Development*	*Ease of Detection*	*Method of Detection*
Initiation – Foundation	Backward erosion piping with eroding soil strata exposed downstream	Rapid if critical gradient is reached	Readily if at surface. Difficult if eroding into ditch or channel	Visual, seepage, pore pressure, thermal, geophysical
	Backward erosion following "blow-out" of overlying soil strata	Rapid to very rapid	Readily to difficult	Visual, seepage, pore pressure, thermal, geophysical
	Concentrated leak erosion	Rapid or very rapid	Moderate to difficult	Visual, seepage
	Suffusion/internal instability	Slow	Moderate to difficult	Visual, seepage, pore pressure, thermal, geophysical
Initiation – embankment to foundation	Backward erosion (not applicable to plastic soils)	Slow, potentially rapid to very rapid at the end	Difficult	Pore pressure, seepage
Initiation – embankment to foundation	Contact erosion	Medium to rapid depending on soil erosion properties	Difficult	Pore pressure, seepage, survey, thermal, geophysical
Continuation	Filters satisfying no erosion criteria	Erosion will cease rapidly if all seepage is intercepted		
	Filtered exit, satisfying some or excessive erosion, or incomplete seepage interception	Filtering should become effective rapidly to medium Rapid to very rapid	Moderate to difficult	Seepage, pore pressure
	Filtered exit, not satisfying continuing erosion criteria, or unfiltered exit	Erosion will continue rapid to very rapid	Moderate to difficult	Seepage, pore pressure
Progression to form a pipe, and a breach Assess time using method in Section 8.9.2.	Gross enlargement in the foundation or in the embankment; and slope instability linked to development of a pipe.	Very rapid or rapid	Moderate to readily	Seepage, visual
	Crest settlement or/and sinkhole in embankment	Medium or slow Usually slow to medium.	Readily	Visual, survey, seepage
	Slope instability, (and unravelling or Sloughing for internal erosion embankment to foundation	Usually slow to medium unless linked to rapid development of pipe.	Readily Moderate to readily	Visual, survey, seepage Visual, survey, seepage

Notes:
(A) Filters are those controlling internal erosion around the conduit, or adjacent walls.
(B) Often the crack and seepage is visible on inspection, but erosion may be intermittent, or only when conduit is flowing with water, so not readily observed.
(C) The evidence seems to be that even for conduits surrounded by erodible soils, e.g. fine sand, the rate of erosion into the conduit is slow.

Table A-3 Rate of development and detectability of internal erosion into and along conduits or adjacent walls (Fell et al., 2015)

Phase of Development	*Mechanism*	*Usual Rate of Development*	*Ease of Detection*	*Method of Detection*
Initiation	Concentrated leak in crack or hydraulic fracture	Rapid or very rapid	Difficult	Visual, seepage
	Erosion into open crack or joint in the conduit or wall	Slow	Moderate	Visual, seepage
Continuation Concentrated leak in crack or hydraulic fracture	Filters (A) satisfying no erosion criteria	Erosion will cease rapidly		
	Filtered exit, satisfying excessive erosion	Filtering should become effective rapidly to medium	Moderate to difficult	Seepage, pore pressure
	Filtered exit, not satisfying continuing erosion criteria, or unfiltered exit	Erosion will continue rapid to very rapid	Moderate to difficult	Seepage, pore pressure
Continuation Erosion into open crack or joint in the conduit or wall	Crack or joint width satisfies excessive erosion criteria.	Slow (C)	Moderate to difficult (B)	Seepage, pore pressure
	Crack or joint width does not satisfy continuing erosion criteria	Slow to medium (C)	Moderate to difficult (B)	Seepage, pore pressure
Progression to form a pipe and a breach	Gross enlargement; and slope instability linked to development of a pipe	Very rapid or rapid	Moderate to readily	Seepage, visual
Assess time using method in Section 8.9.2.	Crest settlement or/and sinkhole in the embankment	Usually slow to medium.	Readily	Visual, survey, seepage
	Slope instability, unravelling or sloughing	Usually slow to medium unless linked to rapid development of pipe.	Moderate to readily	Visual, survey, seepage
	Erosion into a conduit or crack in a wall, usually only progresses towards breach by initiation of erosion along the conduit or wall, in which case factors are as for gross enlargement and instability. For cases which continue towards development of a sinkhole in a crest mode of breach, ability to hold a roof/or sinkhole is critical and the rate of development is usually slow, readily detectable by visual, survey or seepage.			

Notes:
(D) Filters are those controlling internal erosion around the conduit, or adjacent walls.
(E) Often the crack and seepage is visible on inspection, but erosion may be intermittent, or only when conduit is flowing with water, so not readily observed.
(F) The evidence seems to be that even for conduits surrounded by erodible soils, e.g. fine sand, the rate of erosion into the conduit is slow.

Appendix B

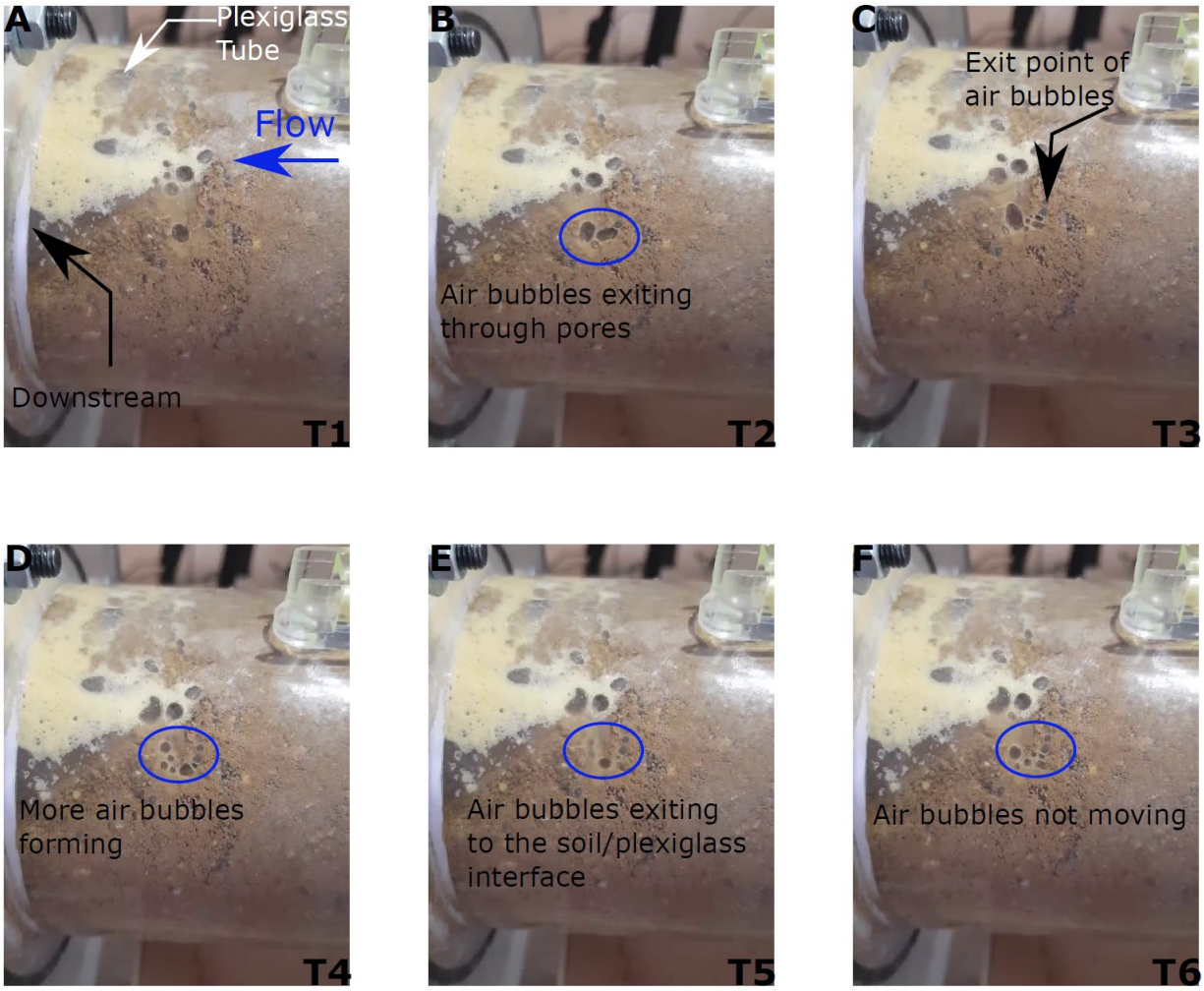

Figure B-1 A to F: Visualization of the seepage of water in the soil medium showing the air bubbles exiting the soil through pores

Appendix C

The seismogram was filtered at a frequency band of 90-120 Hz (Figure 3-12B) to identify the changes observed in the spectrogram (C). It can be noticed that the amplitudes of the events are affected by the day/night cycle where they decrease at night to increase again during the day. Moreover, the amplitudes of the events caused by the double tipping bucket (22 h to 28 h) are much larger than the ones observed in the previous frequency bands (Figure 3-10B and Figure 3-11B).

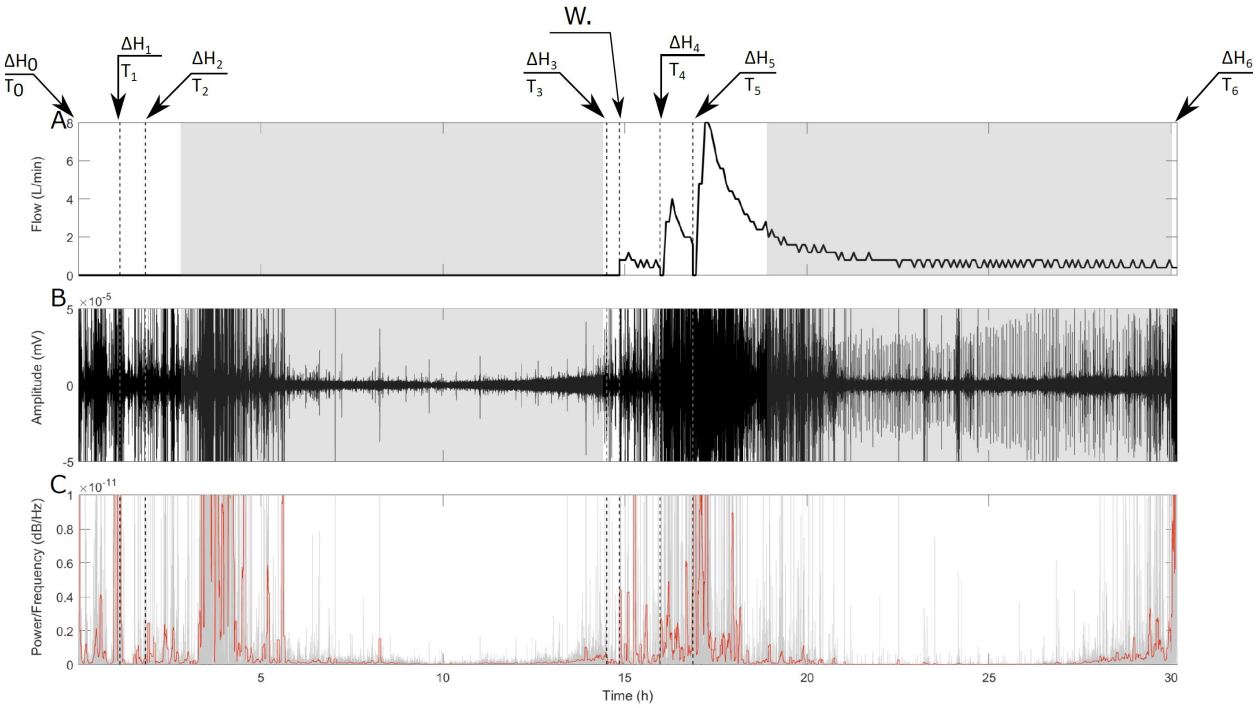

Figure C-1 Analysis of the horizontal geophone (geophone 19); A- Flowmeter measurements with time, B- Filtered seismogram in the 90 - 120 Hz band frequency and C- the PSD of geophone 19 at 100 Hz; the grey data represent the unsmoothed PSD whereas the red data represent the smoothened data

Appendix D

The seismograms corresponding to the horizontal geophones located at and around the channel of seepage. The amplitudes in surrounding geophones in Figure D-1 A, B, D and E are lower than the amplitudes recorded at the geophone on top of the channel (Figure D-1A).

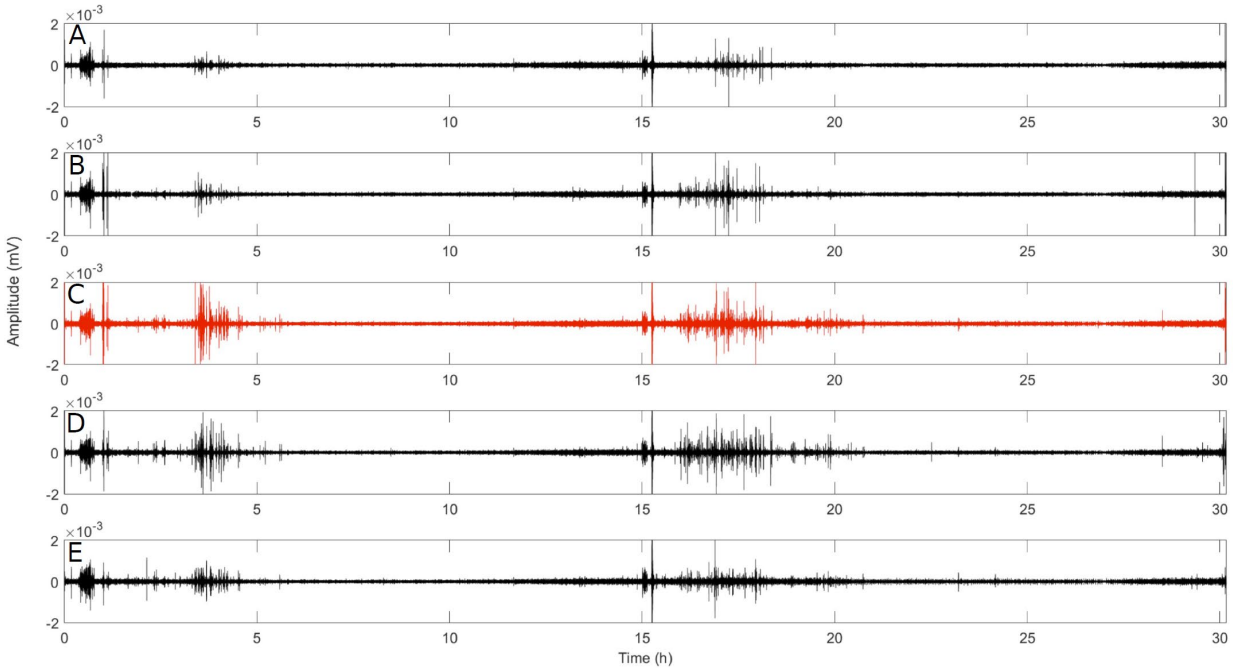

Figure D-1 Seismograms of the horizontal geophones located next to the channel at on top of the channel. A corresponds to geophone 17, B geophone 18, C in red is the geophone located on top of the seepage channel- geophone 19, D geophone 20 and E geophone 21.

Appendix E

The seismograms corresponding to the geophones located on top of the beam are presented in Figure E-1. All the seismograms represent the same response when water was flowing in the soil sample.

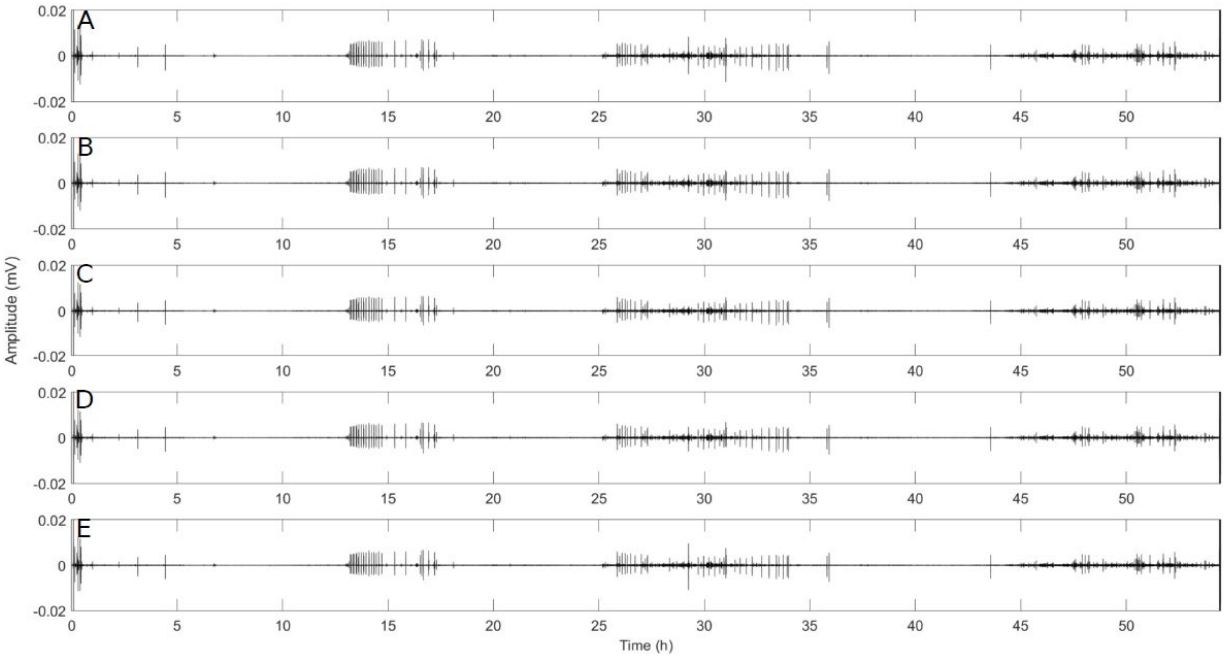

Figure E-1 Seismograms of the geophones located on top of the concrete beam. A corresponds to geophone 1, B geophone 2, C geophone 3 – data of this geophone were used in the study, D geophone 4 and E geophone 5.

Appendix F

The seismograms corresponding to the geophones located on top of the beam are presented in Figure F-1. The seismogram in red corresponding to the geophone located on top of the seepage channel and that was used in this study shows a higher amplitude than the rest of the geophones that were located next to the seepage zone.

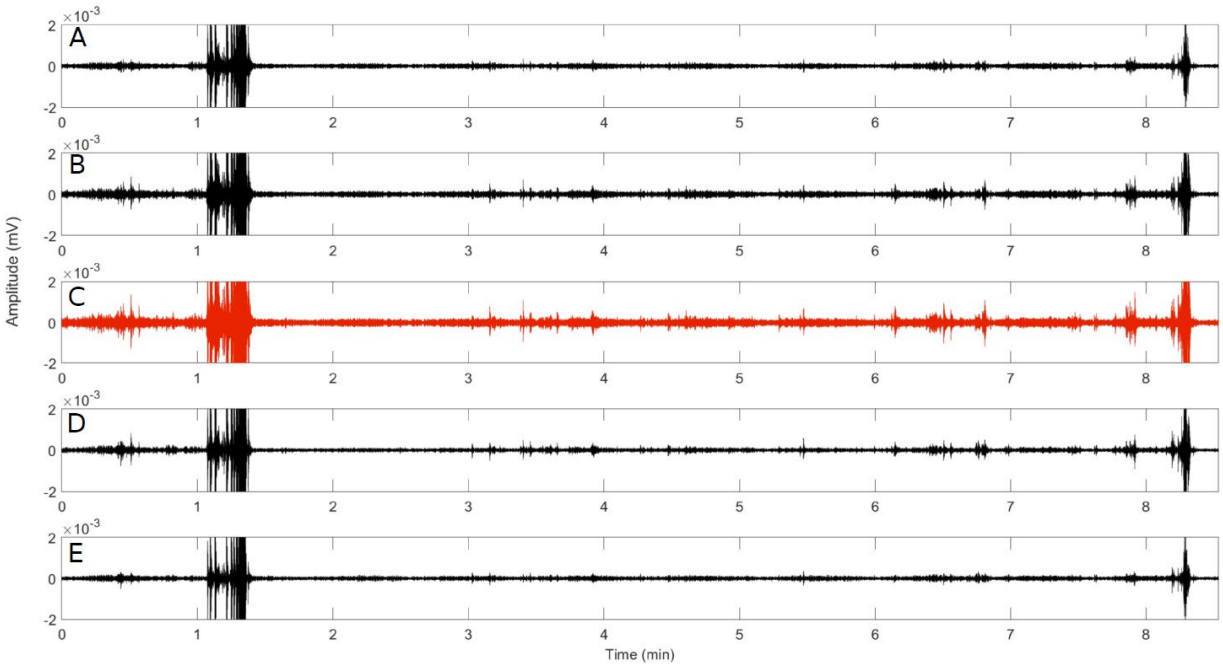

Figure F-1 Seismograms of the geophones located on top of the concrete beam. A corresponds to geophone 1, B geophone 2, C geophone 3 – data of this geophone were used in the study, D geophone 4 and E geophone 5.